Atomic force microscopy studies of DNA origami nanostructures: from structural stability to molecular patterning

Dissertation

zur Erlangung des Grades

„Doktor rerum naturalium"

an der Universität Paderborn

Fakultät für Naturwissenschaften

Department Chemie

von

Saminathan Ramakrishnan

Geb. 22.04.1989 in Aranthangi, India

Gutachter: PD Dr. Adrian Keller

Adjunct Professor, PhD Veikko Linko

Eingereicht am:

Tag der Verteidigung:

Contents

Abstract

After their introduction in 2006 by Rothemund, DNA origami nanostructures have emerged as an important molecular tool for various applications in biophysics, medicine, and engineering. The efficient addressability and simple synthesis protocol for a variety of two- and three-dimensional DNA origami structures allow the single-molecule investigation of various biochemical and biophysical processes. However, under a variety of experimental conditions, the question on the structural stability of DNA origami nanostructures is of importance and pose significant limitations regarding their applicability, for instance in protein folding studies that require strongly denaturing conditions. In the first half of this thesis, the structural stability of DNA origami triangles under chaotropic agents induced denaturing conditions is studied. Chaotropic agents such as urea and guanidinium chloride have been used to induce the denaturation of biomolecules. To this end, the effect of denaturing agents on the structural organization of DNA origami triangles is studied with dependent on the temperature and cation concentration. At a 6M concentration of urea and guanidinium chloride, DNA origami structures are found to be stable at 23°C but completely denatured at 42°C. The structural damage of DNA origami triangles varies with a chaotropic agent. Importantly the DNA origami were found to be stable overnight under 6M urea and guanidium chloride at room temperature. Since the stability of DNA in solution partially depends on the concentration of cations, the role of cations in the stabilization and destabilization of DNA origami triangles in the presence of chaotropic agents is also characterized. Increased cation concentration in solution stabilize the DNA origami triangles in urea but destabilize in guanidinium chloride, due to the possible salting out of Gdm^+. In the second half of the thesis, the ability of DNA origami triangles to self-assemble into a tightly packed monolayer on mica in the presence of Na^+ is used to pattern variety of proteins. The role of cation concentration and protein concentration in the

1

preparation of a well-ordered protein pattern are discussed. Desorption of DNA origami monolayer after directed protein adsorption to create heirachical assembly of proteins is discussed. Additionally DNA origami adsorption in nanoholes arrays, fabricated in gold films on silicon wafers by nanosphere lithography with a well-defined diameter is investigated. The role of ionic strength, incubation time, Mg^{2+} concentration, DNA origami concentration on the adsorption specifictiy is studied. The buffer strength has a surprisingly strong effect on DNA origami adsorption in the nanoholes and multiple DNA origami triangles with 120 nm edge length can adsorb in nanoholes as small as 120 nm in diameter. This is due to the low lateral mobility of once adsorbed DNA origami on the SiO_2 surface which prevents them from maximizing their contact area with the oxide surface and thus results in only partial DNA origami localization inside the nanoholes.

1. Introduction

1.1 Genetic material

The storage, replication, and heredity of distinctive features from parent to offspring had been a question for several centuries. A long history of the search for an important answer came to an end through a simple speculative demonstration using pea plants and a well-studied theory by Gregor Mendel in 1866 called 'Mendelian inheritance'[1]. Decades later, scientists integrated their provisional findings with Mendel's hypothesis on chromosomes and inheritance, that there is an innate material in chromosomes called 'gene'[2] which is the ultimate storage pack of a complete set of information, required in the synthesis, development of unique phenotypes in an organism, that is transformed via reproductive cells[3]. For millions of years, addition, deletion, substitution, and other modifications in gene sequences due to the biological, environmental, physicochemical factors, played a significant role in the evolutionary development path of the organisms[4]. Genes are a specific code of nucleobases that defines phenotype, located on chromosomes[5].

1.2 DNA as a genetic material

Before the invention of the crystal structure of DNA, three basic findings by bacteriologists which cemented the role of genetic material in the transformation of information. The fast replicating nature of experimental organisms, gave an advantage to bacteriologists than others to provide many impressive experimental results to prove the role of genetic material such as Griffith's experiment[6] on pneumococcus pneumonia. When a mixture of heat-killed virulent strains and nonvirulent strains of bacteria were administered in host mice, the heat killed virulent strain of bacteria, transferred its DNA to nonvirulent stain and eventually killed the host. Further important inventions include the first proof for DNA as a genetic material by Avery–MacLeod–McCarty experiment[7] in 1944 who isolated and studied the chemical nature of DNA along with the role of proteins and

3

other substances. The transformation of nonvirulent strain to a virulent strain was studied using pro-knockout experiments where a DNA digesting enzyme deoxyribonucleodepolymerase could inhibit the virulence proving that DNA alone is responsible for the virulence. A year before the publication of crystal structure of DNA, equally critical experimental results from Hershey and Chase published in 1952[8] showed that T4 bacteriophages exhibit the role solely based on the DNA transformation, not by accompanying proteins, even though proteins are partially infused inside the host cells.

1.3 Molecular structure of nucleic acids

On April 25, 1953, three different manuscripts were published in the journal Nature which studied the same question of the structure of DNA. Molecular structure of deoxypentose nucleic acid by Wilkins et al.,[9] molecular configuration in sodium thymonucleate by Franklin et al.,[10] were published based on X-ray crystallographic images of DNA fibers whereas molecular structure of nucleic acids by Watson and Crick[11] was a theoretical approach.

While Wilkins et al., primarily discussed the repeating helical units in the nucleotide, Rosalind Franklin's article focused on the crystal structure of dehydrated A form of DNA and hydrated biological form of B DNA, notably phosphates lie outside the structure of helix, not in the center of the helix.

With acceptable explanation on the refusal of Linus Pauling and Robert Corey's proposal[12] that there are three polynucleotide chains in one DNA molecule, with phosphates inside the axis and bases outside, James Watson and Francis Crick suggested the structure of DNA as follows; DNA is a right-handed, antiparallel double helix chain. Monomer unit of DNA called nucleotide consists of a phosphate, a ribose sugar, and nucleobase. Ribose sugar and bases are to the central axis of the double helix whereas the phosphates are placed outside the helical axis. Each nucleotide is

4

connected with adjacent nucleotide via phosphodiester bond between ribose sugar and phosphate called sugar-phosphate backbone. Major components of DNA double helix are two different nitrogenous nucleobases such as purines (Adenine - A, Guanine - G) and pyrimidines (Thymine - T, Cytosine - C). Bases in one strand are connected to the respective complementary bases in the opposite strand via hydrogen bonds. Adenine and Thymine are paired by two hydrogen bonds (A=T) whereas Guanine and Cytosine are paired by three hydrogen bonds (G ≡ C). The distance between two base pairs in a helix is 3.4 Å. The double helical unit repeats after every ten base pairs in 34 Å length interval. Phosphates are 10.5 Å in the distance from the center of double helix axis.

Despite the same theme and experimental results, few crucial findings of Watson and Crick historically differed their invention from others as follows:

- The need for the presence of peculiar deoxyribose sugar that the additional oxygen atom in ribose sugar would create too close Van der Waals interaction

- Identification of antiparallel double helix

- Reasoning for uninterrupted helical turns with exact width and number of turns

- Chargaff's rule: Apart from identifying physical dimensions of DNA using the Xray diffraction images, Watson Crick base pairing was supported by the critical set of rules published by Erwin Chargaff and colleagues in 1952 that the base composition of DNA molecules includes the equal molar concentration of purines and pyrimidines in one chain. [13,14].

In other words, if the base composition is known for one chain, then the base composition of another chain can be automatically generated. At the end of the article, Watson and Crick mentioned that this specific base pairing suggests a possible mechanism of genetic material copying or DNA replication. After the invention of B-DNA double helix structure and peculiar

Watson-Crick base pairing, Francis Crick once again stated an important combinatory molecular synthesis chain of biomolecules called central dogma of molecular biology[15]. Immediate inventions alongside the structure of DNA opened many options to manipulate the genetic material invitro for structural and functional analysis to provide a platform for understanding of DNA and protein biosynthesis mechanism. Techniques, for instance, the chemical synthesis of DNA bases helped to control the number of nucleotides, length, size, and copy numbers of a double helix, particularly a low-cost research theme when compared to other fields. Laboratory synthesis of dinucleotide by Alexander Todd et al.,[16], total synthesis of a gene by Hargobind Khurana et al.,[17,18], identification of first nucleic acid sequence composition by Robert Holley et al.,[19] led to rapid commercial synthesis and availability of nucleobases. Elucidation of the molecular mechanism of biomolecules such as DNA replication in mammalian chromosomes by Huberman and Riggs et al.,[20] , Arthur Kornberg's discovery of DNA polymerase 1[21], Lehman and Bessman's protocol on enzymatic synthesis of DNA[22,23] posed a significant number of application-specific inventions, for instance, the polymerase chain reaction(PCR) by Kary Mullis et al.,[24]. Along with this route, techniques involved in the isolation and purification of biomolecules using charge and molecular weight based separation, especially nucleic acid separation by electrophoresis[25] and protein purification by chromatography[26] helped in the immediate visualization of the final product which importantly reduced the experiment time.   One of such advancements in molecular biology is DNA nanotechnology which involves synthesis and manipulation of DNA nanostructures for wide range of applications in science and technology.

1.4 Nanotechnology and Atomic Force Microscopy (AFM)

The history of nanotechnology begins with physicist Richard Feynman's vision of a new approach to science in his famous talk at Caltech in 1958 'There is plenty of room at the bottom,'[27] that it is possible to manipulate individual atoms to create a miniature of an object. His talk includes the necessary to create a computer which fit on a bench, a microscope which is capable of graphing the biological events and tiny molecular machines that do the same process like in a biological system, etc.. However, Norio Taniguchi[28] coined the term nanotechnology in 1974. Nanotechnology is defined as the synthesis and manipulation of materials sized 0.2-100nm at atomic and molecular scale[29]. In nanotechnology, the synthesis is divided into two approaches[30].

(i)   In bottom-up synthesis, the building blocks such as molecules, nanoparticles or individual atoms are deposited one on one to create a nanostructure. For example, metal thin film deposition, synthesis of nanoparticles and nanorods.

(ii)   A top-down synthesis method can be described where a bulk structure is decreased in size by successive slicing of individual molecular layers by, for instance, milling, lithographic etching, focused ion beams etching.

The choice of technique decides few crucial factors such as the cost, the control on size and order, homogenous distribution of atoms and reduced number of defects. As an important technique for characterization of nanostructures, in 1982, Scanning Tunneling Microscope (STM) was invented by Gerd Binning and Heinrich Rohrer at IBM – Zurich, for which they were awarded the noble prize[31]. As a part of Scanning Probe Microscopes (SPM), In 1986, Binning, Quate, and Gerber from Stanford and IBM invented the atomic force microscope[32] which played a significant role in the drastic growth of nanotechnology for past 30 years in molecular biology, device physics, chemical synthesis, surface science, lithography, semiconductor devices manufacturing etc.

7

A modification of working mechanism from STM, AFM was invented in the process of imaging nonconductive surfaces using simple probe-sample interaction. AFM mainly employs laser deflection measurement method where a sharp probe is illuminated with a laser beam and scanned over the sample surface or close to the proximity of the surface to measure the deflection in laser beam due to the atomic forces between probe and sample, such as Van der Waals and ionic forces. A scanner is equipped with a laser diode, a cantilever, a position sensitive photo sensor and a piezoelectric ceramic transducer or piezo actuator. A silicon-based cantilever with a sharp probe is mounted on a tip holder. During the measurement, typically an optical lever method is used that a laser beam is focused and reflected from the backside of a cantilever to a position sensitive quartered photodetector. This detector measures the deflection intensity which is directly proportional to the displacement of the cantilever and converts this signal into electrical signals. The movement of the scanner in X, Y, Z directions is achieved via a piezo actuator which responses to the change in geometry when the voltage applied. Different types of the piezoelectric sensors can be used to create well-defined motions from nanoscale to microscale per volt applied. When cantilever scans the surface of the sample, the force between tip and sample is measured by Hooke's law.

$$F = -kz$$

Where k is the stiffness of the cantilever and z is the distance cantilever bent due to the force.
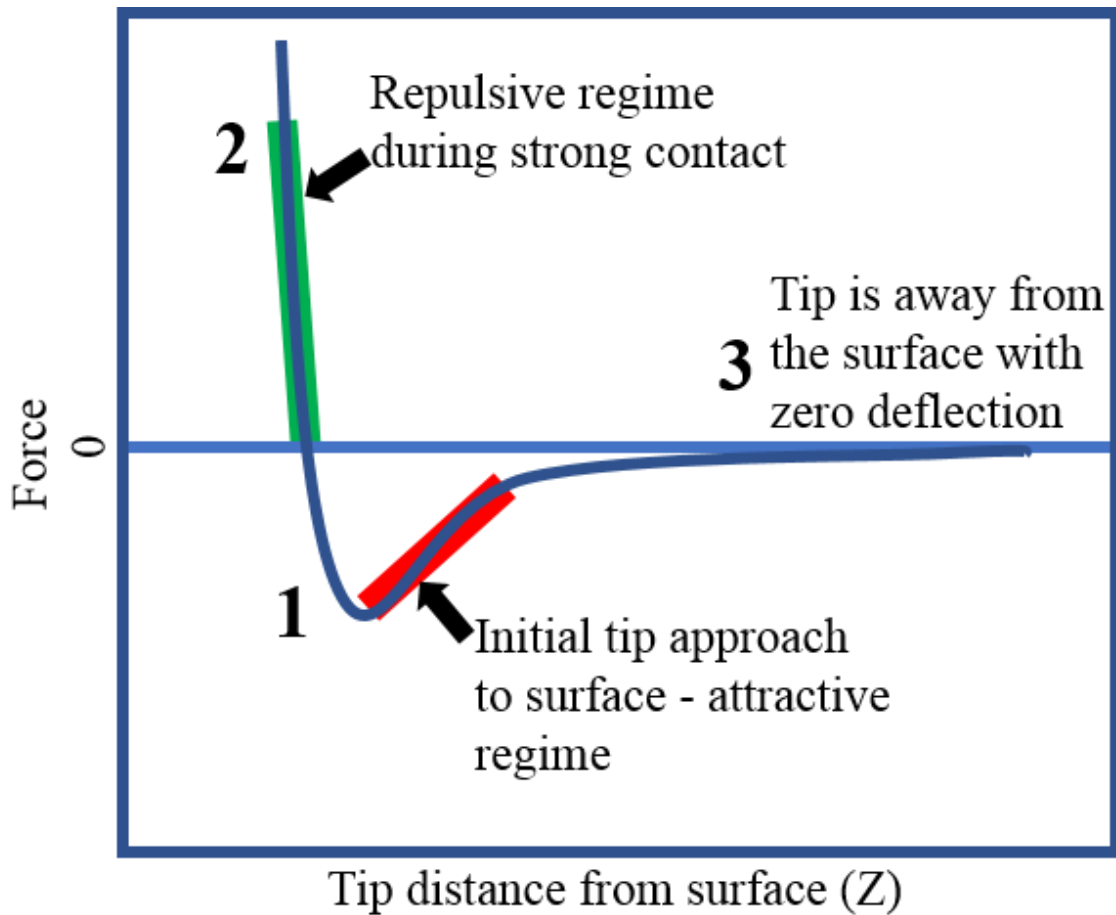
Figure 1. Force vs. distance curve

Force-distance curve [33] is generated using the cantilever deflection against the extension of the piezo scanner or probe distance from the sample. Figure 1 shows a three-regime force vs. distance curve. When tip approaches a sample surface, initially the atoms tend to weekly attract each other, and Van der Waals force falls into the attractive regime. However, in the repulsive regime, due to close contact, the electron clouds in both atoms strongly repels and reduces the attraction. Any force close to this will end up in the repulsive regime and additional force to push the cantilever more than the repulsive regime will eventually damage the surface or cantilever. On the third regime, the force becomes zero when z distance reaches several nanometers.

Based on force-distance curve, the operational modes of AFM can be divided into three:

9

1. **Contact mode in the repulsive regime:** In contact mode, the piezo actuator operates in two ways to move the tip against the sample or sample against the tip depends upon the AFM and cantilever deflection is collected to generate force distance curve. During the measurement, a feedback loop operates to maintain the stable Z range movement of the probe. To maintain the value of deflection stable, a feedback loop senses the actual deflection during measurement and compares it with the desired value of deflection. If the measured deflection value differs with desired deflection value, then the feedback amplifier engages the piezo actuator to increase or decrease the position of the sample. However, a typical problem with contact mode is excessive tracking force applied by the probe which can be overcome by the noncontact mode of measurement where the probe is kept in the attractive regime and importantly few nanometers away from the sample.

2. **Non-contact mode in the attractive regime**: In non-contact mode or amplitude modulation mode, the cantilever is vibrated along the sample, and cantilever deflection using amplitude or resonance frequency is collected as a function of tip-sample distance. However, since the principle working mechanism is based on the Van der Waals force, in non-contact mode, the Van der Waals force becomes weak when the distance between the probe and sample increases, and ultimately gives a hard time to measure the high-resolution topography. Excessive tracking force in contact mode and reduced Van der Waals force in non-contact mode can be overcome by the important and widely used tapping mode or intermittent contact mode

3. **Tapping mode**: Tapping mode is an advancement in AFM measurements to overcome the problems from friction, electrostatic forces etc. In tapping mode, the cantilever is oscillated on the sample surface with large vibration amplitude and retraced continuously to avoid dragging on the surface. Continuous approach and lifting off with high amplitude provides

reduced oscillation due to the loss of energy by contacting surface. A feedback system maintains the stable oscillation amplitude. Depends upon the surface feature, the amplitude increases or decreases and the changes in oscillation amplitude is used to generate the image.

The role of AFM in the development of DNA nanotechnology has been enormous in the senses of cost effective technique, less time consuming and precision in providing topographic information.

1.5 DNA nanotechnology

DNA nanostructure is a self-assembled molecule synthesized by rationalized Watson-Crick base pairing which exhibits numerous possible ways to articulate the structure of DNA in 2D,3D and precisely design and define the choice of applications in physics, chemistry, biology, medicine and computational engineering. In this chapter, we discuss the short history of development path of DNA nanotechnology.

The primary role of DNA in all living things is to store, copy and transmit the genetic information employing a specific combination of DNA sequences that can be identified by enzymes, for instance in DNA recombination and replication machinery. The role of DNA is determined by the combination of inter and intramolecular recognition. Genetic engineering studies manipulate the intermolecular recognition, functions, and property of DNA, for example, an artificial plasmid DNA structure[34] in recombination technology. Later, the intermolecular recognition specificity between DNA and enzymes opened up research themes like the artificial synthesis of insulin[35].

However, the molecular recognition specificity inside the DNA double helix structure was first introduced and utilized by Nadrian Seeman[36], a protein crystallographer to address, assembling protein molecules in a self-assembled 3D network of DNA using Watson-crick base pairing and sticky end strategy. Three significant research inventions would have inspired Nadrian Seeman to

11

arrange DNA molecules into multiple molecular junctions through sticky end ligation method. Watson Crick base pairing, Holliday Junction, chemical synthesis of DNA bases.

As he mentioned in his article, the proposal of the existence of Holliday junction, a homologous recombination intermediate of DNA during meiotic cell division in fungi by Robin Holliday in 1964.[37] Research findings[38,39] followed had confirmed that the isolation and analysis of such junctions are not possible due to the formation of branch point migration and preferably a double helix followed by that. However, using peculiar Watson-Crick base pairing and complementarity, if the sequence symmetry is compromised and junctions are made immobile, then it is possible to create a branched, four-way junctions when few more rules are followed. Seeman created four basic rules and a FORTRAN program based on it to generate sequences accordingly. Figure.2 shows an immobile Holliday junction structure according to the four important rules of Seeman. In a four-way junction with multiple overlapping short sequences, every single overlapping sequence should be unique throughout the structure. Individual complimentary sequences of overlapping sequences, especially which are close to the junction, should not be present elsewhere in the structure. Self-complementary sequences should be avoided, and a maximum number of repetitive base pairs should be less than three and be present only in opposite junctions.
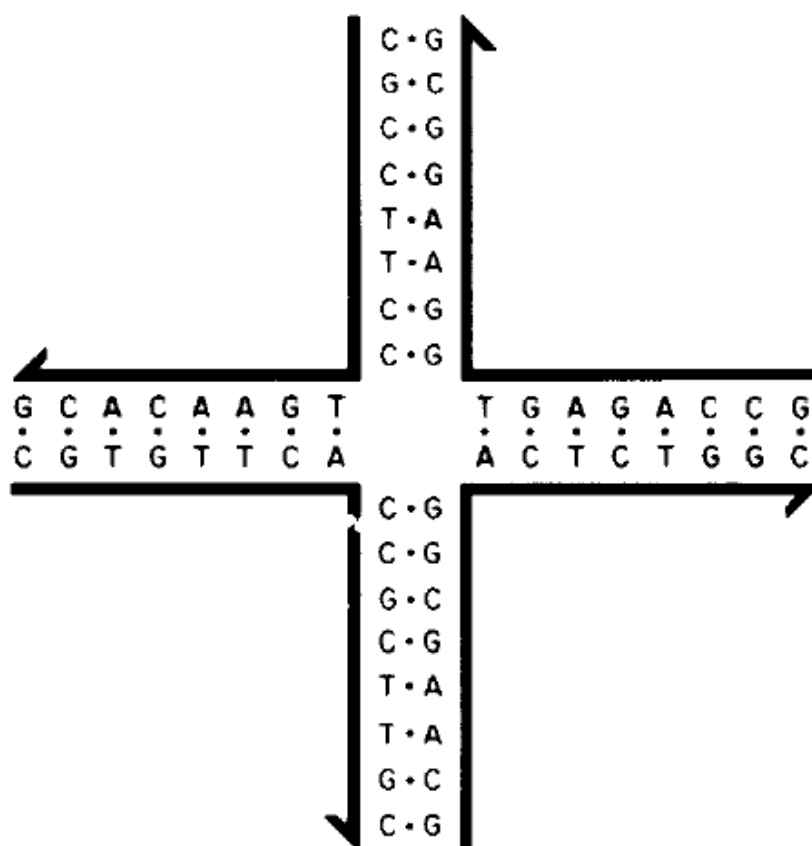
Figure 2. An immobile Holliday junction designed by Nadrian Seeman which follows the four basic rules of synthesis of DNA nanostructures[36].

Furthermore, Individual four-way junctions synthesized with flanking short sequences called 'sticky ends' could yield a DNA lattice for X-Ray diffraction studies. As a direct application of immobile Holliday junctions and their analogs, Seeman et al.,[40] demonstrated the role of two different resolvase enzymes which cleaves Holliday junctions depends upon the orientation using radiolabeled footprinting method.

In 1991 and 1993 two famous works of Seeman were published. First, construction of a 3D cage [41] using sticky end based DNA hybridization which led to the synthesis of compound DNA nanostructures with potential application in later years such as DNA tetrahedron[42], DNA truncated

13

octahedron[43]. Secondly, in 1993 Seeman et al.,[44] studied the possibilities of parallel and antiparallel double cross over constructs with odd and even fashion of hybridization which later laid the foundation for the 2D DNA crystal like lattices [45] and importantly DNA origami[46]. In the following decades, the synthesis of a variety of two- and three-dimensional DNA lattices based on different DNA tile motifs have been reported[45,47–50]. Excellent reviews are available elsewhere [51–55].

Apart from that, the sole purpose of DNA lattice is to address individual molecules by linkers, so that the arrangement of molecules will be periodical. However, yield from one pot synthesis, the floppy nature of DNA[56] and less rigidity when it grows into a crystal-like lattice were significant problems to be addressed. All these three problems mentioned were overcome by the famous Rothemund's DNA origami nanostructures.

1.6 DNA origami

DNA origami [46] or Rothemund's origami is a self-assembled DNA nanostructure using a bottom-up approach. For assembly, a long, single-stranded viral genome or 'scaffold' is folded into a desired arbitrary 2D or 3D nanoscale structure using base pair complementarity and segmental crossovers of a large number of short oligonucleotides, so-called staple strands. The sequence of the single-stranded scaffold is known, and respective complementary sequences are designed in such way that the size and shape of DNA origami structure are predefined. Specifying the folding path is the first experimental step in which the desired shape is conceived by filling the required number of evenly paired, parallel helical cuts. Count of turns per helical cut can be varied from 1.5 to 4.5 depends on the shape required. However, the clipping crossover by short staples occurs every 1.5 turns, and turn's length is distributed in whole numbers all over the structure for example 16 bases per 1.5 turn, unlike in the natural B DNA structure which is 10.5 bases per turn. In the next step, single-stranded helical cuts are hybridized with short staple strands by periodic crossovers.

The staples are partially complementary to adjacent helices and sometimes to three helices. The stacked arrangement of helical cuts creates junction points of scaffold called scaffold crossovers which meets in an odd number of half-turns when the alignment progress and even number of half-turns when reverse. After the antiparallel crossovers by staple sequences are designed for the compatible DNA structure, the sequences are generated using a computer program.
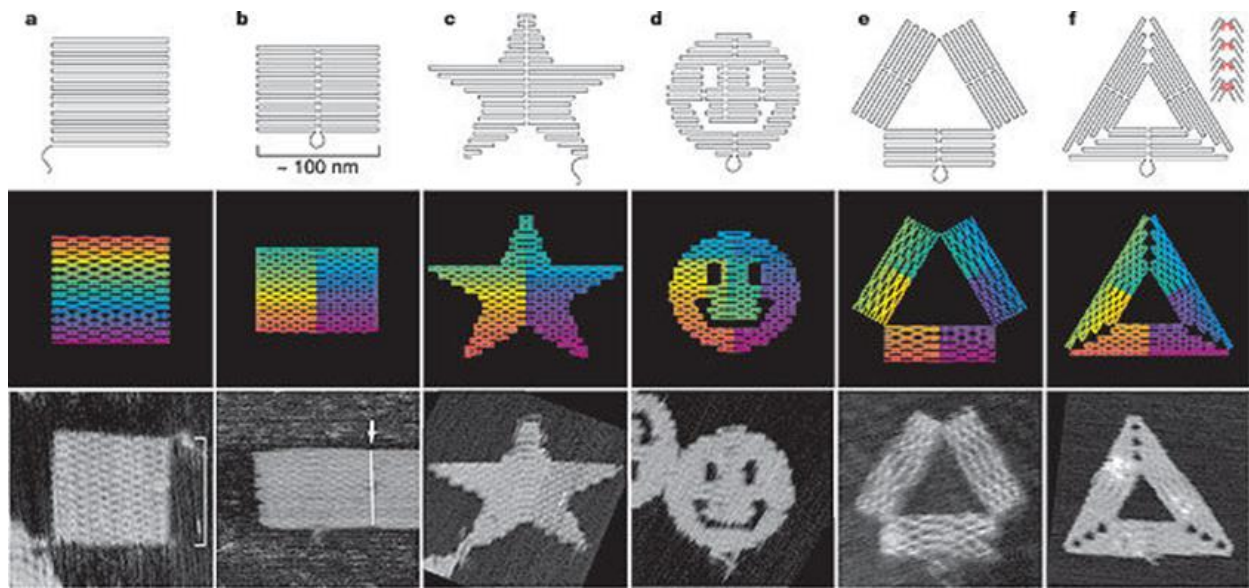
Figure 3. Folding path specified Rothemund's origami nanostructures synthesized using a long single-stranded viral genome. a) square b) rectangle c) star d) smiley e) triangle with rectangular domains f) triangle with trapezoidal domains. The AFM images of the third row have a size of 165nm*165nm.[46]

For example, in DNA origami triangle, in the final step, 207 short staple sequences are mixed with M13mp18 scaffold about 100-fold excess in the magnesium-containing buffer, preferably in 1X TAE buffer and synthesized by stepwise thermal annealing. The initial annealing temperature is set at the maximum melting temperature of a sequence in the reaction mixture and gradually cooled down to room temperature. Optimized sequences, minimized free energy and maximized Watson Crick base pairing along with the preferred antiparallel multiple crossovers, results in a perfect

15

assembly of DNA origami nanostructure. Figure.3 shows different Rothemund's DNA origami nanostructures of square, rectangle, star, smiley and triangles with rectangular and trapezoidal domains.

The resulting DNA origami nanostructures may serve as spatially addressable molecular breadboards that enable the controlled arrangement of functional entities with nanometer precision, which then would serve as a molecular platform to perform, for instance, molecular biological events such as protein-ligand interaction studies.

Inexpensive, robust synthesis protocol with precision and high yield provide three critical advantages over conventional DNA nanostructures or crystal-like lattices. The DNA origami nanostructures are relatively rigid due to the multiple crossovers inside the structure. Annealed short staple sequences can be extended from their original length to provide specific ligands to functionalize the surface with many different biomolecules, organic-inorganic nanomaterials. Yield is high with a reliable number of wholly synthesized structures without structural defects.

Just ten years after the introduction by Rothemund in 2006, DNA origami technique enabled the fabrication of larger DNA tiles with almost arbitrary shapes[46] that could be arranged into more complex lattices either by solution-based[46,57–62] or surface-assisted[63–67] hierarchical self-assembly and widely used in various fields of applied and fundamental research. In particular, the possibility to modify selected staple strands with metallic,[68] semiconducting,[69] and biological nanoparticles,[70] fluorophores,[71] proteins,[72] and DNA strands of desired sequence[73] and topology[74] renders DNA origami nanostructures powerful platforms for single-molecule studies.[75,76] DNA origami act as masks in molecular lithography,[77–79] templates for nanoelectronic[80–82] and plasmonic[83–85] device fabrication, as delivery vehicles in molecular medicine,[86–88] and substrates for biophysics, nanotechnology, sensing, and medicine.

16

Though the synthesis protocol is not complicated for many DNA origami nanostructures, in every application, the critical point to consider is the stability of DNA origami nanostructures under biological and nonbiological experimental conditions.

1.7 Structural stability of DNA origami

Denaturation of macromolecule[89] is defined as the total disruption of primary, secondary or tertiary native structure due to the biological, physical and chemical factors that break the stabilizing bonds. In DNA, Structural stability [90,91] is determined by the hydrogen bonds between nucleobases, base stacking between the aromatic rings. Many of the applications of DNA origami rely on an intact and well-defined shape as well as tailored mechanical properties of the DNA origami. Consequently, the stability and denaturation of DNA origami nanostructures under diverse application-relevant conditions has received growing interest from different research fields[92–99].

1.7.1 Biological factors

Among the three possible forms of DNA, hydrated B form is abundant in cells than dehydrated, compact A form and left-handed Z form. Synthesis, repair and degradation events corresponding to the DNA completely relies on the intermolecular recognition between enzymes and DNA. For example, in mutation, the DNA sequences are replaced with mismatching bases[100] during DNA replication which may leads to cancer or other diseases. However, cells are equipped with very sophisticated and efficient proofreading mechanism and DNA damage repair mechanism such as nucleotide excision repair to ensure the genetic stability. In biological condition, intermolecular recognition between DNA and enzymes is achieved via the chemical moieties in nucleobases, for instance by proofreading enzymes in DNA repair. This molecular recognition leads to controlled or programmed events such as scanning of nucleotide sequences by polymerases[101], unwinding of DNA duplex by helicases[102], removal of additional segments during repair by cytoplasmic

17

nucleases[103], or in bacteria, specific scission of nucleobases by DNA restriction enzymes[104]. One such event is digestion and degradation of nucleic acids by nucleases.

Genomic DNA is digested in nucleus, cytoplasm, and cytosol at various conditions. In the nucleus, programmed cell death or apoptosis involves a crucial stage of chromosomal DNA degradation by caspase-activated DNase or CAD to prevent cancer formation[105–107]. Once the cell is dead, lysosomes in phagocytes degrade the cellular materials including the DNA using lysosomal TREX 1 or DNase III and DNase II to reuse the basic building blocks later. Since the undigested nucleus material in the cytosol will induce autoinflammatory condition[106], lysosomes[108] that produce 60 different hydrolytic enzymes such as proteases, nucleases and lipases will efficiently identify macromolecules and organelles via the membrane spanned glycoproteins [109] during phagocytosis, as a part of defense mechanism [110,111]. In the cytoplasm of fiber cells of the optic lens, a specific DNA digestion enzyme is employed called DNase II-like acid DNase or DLAD to digest the nucleus material, so that the lens is transparent[106]. Apart from these, another essential waste management nuclease called DNase I[107,112] is abundantly available in kidney, liver, pancreas, alimentary tract and serum to clean up the DNA that arises from infection, apoptosis and accidentally dead cells, to prevent autoimmune diseases[113].

1.7.2 Stability of DNA origami in biological conditions

Nanotechnology-mediated drug delivery system[114] has been widely studied to overcome the difficulties in conventional therapeutics such as insolubility of drugs, specificity in targetting, multiple targetting, controlled release and extended availability of the drug, especially in cancer therapy. However, there are disadvantages[115] found along with the rapid development of several different nanoparticle-mediated approaches. In toxicological perspective[116–118], the nonbiological surface chemistry of a nanoparticle would create adverse immune effects on the body; nano-

physical dimensions may end with deposition in organs. For instance, carbon nanotubes induce inflammation[119], and other toxicities[120], fullerenes[121] as antimicrobial agents are ecotoxic[122], quantum dots are cytotoxic[123] and induce heavy metal poisoning[124]. Moreover, gold, silver metallic nanoparticles induce free radical assisted cell death in healthy cells[125], accumulates in the blood-brain barrier[126]. In the case of biocompatible liposomes mediated drug delivery, aggregation of particles, low stability in storage and encapsulation are common experimental problems[127]. Additionally, tuning the size of the particle and multiple functionalizations of the nanoparticle surface are comparatively tricky, time-consuming procedures than in DNA origami. In this part, we focus on the advances and structural stability of DNA origami in drug delivery and imaging based experimental approach.

Knowing the advantage that functionalization of DNA nanostructure surface is efficient, the idea of encapsulating a protein molecule inside a DNA cage is first demonstrated by Erben et al., [128] with cytochrome C protein. Along with that, functionalization of DNA origami surface with quantum dots[129] to track the molecule using fluorescent signals[69,130] paved a way to use DNA origami in medical biotechnology either in diagnostics or therapeutics or both[131]. When DNA origami is used in cellular environments, there are several factors that can affect the structural integrity, for instance, nucleases. As a direct demonstration in therapeutics and drug delivery using DNA origami, Zhao et al.,[86] reported the synthesis of twisted DNA origami tubes to encapsulate with doxorubicin that induces programmed cell death in breast cancer cell lines. The efficiency in cytotoxicity and drug releasing kinetics between free doxorubicin and cargo loaded doxorubicin was studied where the doxorubicin-loaded DNA cargo was more effective than control. The DNA origami cargo was found to be stable when treated with treated 10% fetal bovine serum at room temperature up to 48 hours in pH between 4 to 10.

19

To directly observe the structural stability of DNA origami when delivered in the cellular environment, Shen.et.al[99] modified the DNA origami tube's surface with fluorescein, cyanine dyes and incubated in breast cancer cell lines. Transformation of weak emission property of cyanin fluorophore to strong emission, when bound to DNA linker, was used in this experimental approach to analyze the intactness of DNA origami in the presence of DNase1. Additionally, the localization of DNA origami was found in lysosomes up to 12 hours, and complete denaturation was observed at 60 hours. Inside the cell, the DNA origami tubes were found to be stable in the folded state up to 24 hours. These critical results proved the inherent biocompatibility of DNA origami nanostructures in drug delivery applications.

Qiao Jiang et al., [132] investigated the efficient drug loading of DNA origami with doxorubicin. By comparing the toxicity of free doxorubicin, doxorubicin-loaded ds-DNA, and DNA origami triangle, the results show that DNA origami loaded doxorubicin are more efficient and importantly breaking the drug resistance of cancer cells. Lysosomal acidification[133] is an essential criterion in the degradation of macromolecules during the endocytic pathway where the surrounding of lysosome cell wall maintains high acidic pH. However, in drug-resistant cells, intake of drugs is suppressed by the acidic conditions of lysosomal lumina. DNA origami triangles loaded with doxorubicin changes this property of lysosomes by increasing the pH from the high acidic condition and improves the efficient intake of doxorubicin.

Hahn et al. studied the two crucial factors, low magnesium concentration and a nuclease that affect the stability of DNA origami in tissue culture environment[95]. Cationic strength is fundamental to protect the DNA structure from charge-screening mediated destabilization. Among octahedron, 6-Helix bundles, and 24-Helix rods tested in low magnesium buffer, 6-helix bundles were found to be stable. Even though the tissue culture media has relatively high concentration of sodium

monovalent cation than magnesium cation, octahedron and nanorods were entirely denatured at 24 hours time interval. However, no structure was stable in the presence of fetal bovine serum(FBS), supplemented with a nuclease. Apparently, heat inactivation of nuclease or nuclease inhibitors in FBS was found to reduce the rate of DNA origami nanostructure degradation.

DNA origami is also reported as a molecular chip to detect the single molecule events, for example, label-free RNA hybridization[134] and single nucleotide polymorphism[135] or DNA origami surface modified with specific surface antigens that can identify and bind to disease-related antibodies[136]. A malarial protein expression was observed on DNA origami rectangle, modified with specific antigen like DNA aptamers[136]. In such experiments, a cell lysate may be used for the hybridization or protein-ligand binding. Qian mei et al.[98] reported that DNA origami are stable in cell lysate and further recovery from gel and imaging is possible. The experiment was performed in normal and cancer cell lysate in which the DNA origami rectangle, triangle, and cuboid shapes were stable in all lysates and recovered, unlike the double-stranded DNA, because of the probable entangling with cellular proteins and enzymes.

Unlike in cell lysate, Jiang et al.[93] reported that 3D DNA origami nanostructures are extremely sensitive and exemplify almost instant degradation when exposed to 0.1 % serum. The height of DNA origami boxes collapsed up to 80% within the short span of time and further modification of surface may be required to improve the stability under serum conditions. Apparently, DNA cage end modification with single-stranded sequences resulted in improved stability in serum[137].

DNA Origami is widely considered for the targeted drug delivery[138] because of the possibilities to modify the surface chemistry with specific markers and efficient loading and releasing kinetics in liquid. The surface chemistry of the DNA origami plays a vital role in target recognition. Efficient interaction of DNA origami with cell surface was demonstrated by Douglas et al. , who synthesized

21

a DNA origami nanorobot - aptamer gated drug delivery vehicle which responses to aptamer antigen binding and induces cancer cell growth inhibition[139]. Additionally, Interaction and working dynamics of DNA origami with a cell can be tuned in different ways. For example, lid opening of a DNA origami box and release of the load can be controlled by external nucleic acid sequences or keys[140]., and motion of a DNA structure can be programmed[141], even the open/close gates to capture and release the molecules can be preplanned[142]. The interaction of DNA origami carrier with the cell surface can be improved by modifying with hydrophobic molecules like cholesterol moieties[143] or specific growth factors [144] and transferrin[145] to improve the cellular uptake. Recently, a programmed DNA origami robot[146,147] has been developed in the research group of Ido Bachelet, which can be stimulated and operated by electromagnetic waves to open or close the logic gates, using complementary DNA sequences, e.g., strand displacement reaction and aptamer binding to deliver the payload upon signal in DNA origami cargo. Since the stability of DNA origami in cancer cell lines has already been studied, all the modifications abovementioned would end up in improved recognition, internalization, and degradation of DNA origami by nucleases within a short span of time.

Apart from the stability of DNA origami nanostructures, DNA tetrahedron have also been studied under denaturing conditions. Walsh et al. utilized the stability of DNA tetrahedra., [148] as a cargo for drug delivery and in vivo imaging. DNA tetrahedra were monitored for structural integrity inside the live mammalian cell using FRET measurements. The structures were intact and stable up to 48 hours. Importantly the DNA tetrahedra do not require the transfecting agent to get inside the cell. The ability to transfect the fluorescent molecule loaded DNA cargo was demonstrated with high yield and persistence. Contrary to the protection of DNA origami or nanostructure surface with chemical moieties, a stable DNA tetrahedron in nuclease[149] was reported by Keum Et.al., in which the binding affinity of nonspecific nucleases was inhibited by rational designing of the

22

structure. Branched geometry or curvature in a DNA structure would inhibit the recognition of DNases and reduce the rate of digestion. This ability to withstand the enzymatic digestion can be a cumulative effect of several factors including DNA sequence, geometry, and size.

Some recent studies have attempted to increase the stability of DNA origami nanostructures using various coatings, including lipid bilayers[150], virus inspired encapsulation[150], various polymers,[151,152,152–154] and proteins.[155,156] Coating of the DNA origami nanostructures with these materials resulted in restricted accessibility of enclosed cargo,[151] as well as increased DNA origami resistance against DNase digestion,[150,152,153,155,156]. low-salt conditions,[153,156] and high electric field pulses.[154].

1.7.3 Physico-chemical factors

Thermal denaturation is a standard experimental procedure to calculate the melting temperature of a DNA sequence where hydrogen bonds between bases, hydrogen bonding between the phosphate-sugar backbone and surrounding water molecules, stacking interactions between aromatic rings are broken. Melting behavior of the duplex or unwinding is dependent to increment in temperature which differs with the composition of bases, for example, AT base pair has lower melting temperature than GC base pair[157]. In addition to it, the ionic strength of the buffer, length of the DNA duplex and G-C content determines the stability of the DNA duplex [158]. DNA origami has several segmental crossovers by staples and inhomogeneous composition of bases. Since the individual melting temperature of the staple sequences falls between 30°C to 90°C, it is not possible to generalize the melting behavior of the whole DNA origami structure. It differs between shapes.

Maintaining the structural integrity of the DNA origami may pose significant limitations regarding their applicability in biophysical and biochemical studies. Typically, DNA origami is assembled in TAE buffer supplemented with moderate concentrations of Mg^{2+} ions to screen the electrostatic

23

repulsion between neighboring double helices. Deviations from these buffering conditions can have devastating effects on the DNA origami, ranging from aggregation to shape distortions to total structural collapse[64,95,159]. Thus, a number of recent studies have investigated the stability of different DNA origami nanostructures under various application-relevant conditions.[92–95] Especially the article from Kim.et.al.,[92] showed surprising DNA origami stability under harsh conditions such as high temperatures and pH values, when DNA origami is heated in dry state, the decomposition begins only at 230°C , DNA origami triangles are stable in the presence of hexane, ethanol, and toluene organic solvents up to 24 hours. The deionized water damages the DNA origami because of the absence of cations in solution. Low pH denatures the DNA whereas the structural integrity can be maintained up to pH 11. Under highly oxidative conditions, the DNA origami structure maintained its integrity even at 15 minutes exposure time of UV/ozone [92].

Wang et al. studied the effect of parameters on DNA origami structure that involve in protein crystallization processes such as cationic strength, pH, protein precipitants, and type of the buffering agent. When the DNA origami was synthesized in four different protein crystallization buffers of lysozyme, thaumatin, human serum albumin, catalase, the DNA origami structures were stable only in catalase protein crystallization buffer. In Na^+ containing buffer, the synthesis of DNA origami was not affected, but in the case of Ca^{2+}, K^+, NH_4^+, DNA origami was not formed. Additionally, the synthesis was not affected by Tris, HEPES, PEPES, MES buffering agents and precipitating agents like alcohols and polymers. Except for the pH 4, the DNA origami synthesis was successful up to pH 10.

Isothermal folding is an advancement in temperature mediated folding of DNA origami nanostructures. Since it is necessary to do subsequent annealing to incorporate temperature sensitive functional moieties on DNA origami, an alternative was proposed by Jungmann et.al.,[160]

in 2008 and followed by Kopielski et al., [161] that formamide mediated one pot folding is possible. Serial dilution of the concentration of formamide-based folding buffer by dialysis efficiently annealed a stable DNA origami structure. Moreover, the same experimental procedure was further improved to fold at room temperature without dialysis[162].

1.7.4 Mechanical stability

DNA origami has been used in optical tweezers[163][164,165]. Since the arrangement of holiday junctions in DNA origami structure determines the stability of the internal cavities of DNA origami , the structure may break when the force applied from one or both the ends of a DNA origami. On the other hand, rational designing of DNA origami nanostructures may help to overcome the restrictions in force measurements of, for instance DNA-protein interaction. Nickels et.al.,[165] constructed a nanoscopic force clamp using DNA origami nanostructure to study the TATA binding protein induced bending in DNA which is relatively a difficult approach due to the long tethers in conventional spectroscopy measurements. The stiffness of a molecular linker is another critical problem that can be solved using a rigid rod-like DNA origami nanostructure in single molecule spectroscopic experiments, for example, in protein conformation dynamics studies. When sub-nanometer ranged changes in protein confirmation is being recorded, the signal to noise ratio at low force regions can be affected by floppy DNA linkers. Emanual et al.,[166] demonstrated the stiffness of DNA origami using six, eight, ten and twelve DNA origami bundles. The hopping signatures between the unfolding and refolding are discriminable in the presence of DNA origami linkers whereas in conventional ds DNA linker it is not due to the low force to noise ratio. The noise suppression can be greatly achieved with the helix bundles with several binding motifs to beads.

Shrestha et al., [167]. Demonstrated that DNA origami tubes are mechanically more stable than pyramids and tile structure. After the DNA origami nanostructures were tethered to polystyrene beads using optical trapping method, DNA origami were stretched longitudinally to observe the rupture transitions depends on force range. Lower force range provides reversible rupture transitions, and high force range gives irreversible rupture. Irreversible rupture at low force range is concluded to the stability of holiday junctions in the DNA origami. For example, Nano tiles behave like longitudinally stretched nanotube at high force range which eventually shows irreversible rupture. The most stable structures are 3D nanotubes with the property of distal Holliday junctions come closer and form the isomerization transition upon stress. Due to the open 2D structure, Nano tiles and Nanopyramids exhibit week stability when the force applied longitudinally. 2D structures do not comply with the movement of holiday junction and end up in breakage of immediate holiday junction close to the stress axis. Moreover, no mechanical transition or intermediates were observed for nano tiles and pyramids due to their planar and pyramidal symmetry or absence of circular geometry like tubes. Importantly, stretching axis did not change the property of Holliday junctions when the force applied. At high force transition, horizontal pulling shows higher stability than the longitudinal pulling. Because of the availability of layer by layer disassembly in longitudinal stretching and several intermediates were observed during the disassembly process, which shows the less stability when compared to horizontal stretching.

Anchoring a DNA origami tube on a substrate by a single link or multiple links may express high-level resistance to the stress in angular or torsional motion because of the available Holliday junctions in circular symmetry to resist the breakage. On the other hand, DNA origami has been considered as a right tool for the construction of nanorobots and rotors which demands bending and torsion. With DNA 6 helix and four-helix bundles, Ralf Seidel et al.,[168] demonstrated the torsional and bending rigidity by using optical tweezers. With better bending rigidity compared to

26

the double-stranded DNA, the torque rigidity is weak and very close to that of double-stranded DNA by buckling in the same fashion after specific torque is applied, maybe because of stacking interaction between bases. To overcome the torsional restrictions in the DNA origami nanostructure, Zhao et al.,[169] designed a DNA origami structure with tunable torsional angles by using a ssDNA sequences as a connector between two sides. Lesser the sequences length, higher the torsional angle with less stiffness, the torsional angle between the two parts could be adjusted to the length of DNA sequence.

1.8 DNA origami for molecular patterning

1.8.1 Surface-assisted hierarchical assembly

Initially, the purpose of the invention of DNA nanostructures was to create a periodic lattice for protein arrays using addressable spaces. Using sticky end ligation strategy, Liu et al.,[59] first demonstrated the assembly of 2D crystal-like lattice with seeman tiles where the basic tile structure was modified with multiple sticky ends in every side and thermally annealed over days to create a lattice. Even though this approach is not the best way to create a perfectly assembled lattice over a large area, maximum of the 10µm sized lattice was obtained. Importantly physical stress on DNA origami when it grows into the large lattice, limitation in periodicity and size, number of defects and complex protection strategies in solution based sticky end ligation, makes it hard to use in conventional molecular patterning approach.

Woo et al.,[64] presented an alternative approach to create a checkboard like DNA origami lattice with rectangular DNA origami structures using blunt-end stacking interaction on mica. This approach consists three steps,

1. The DNA origami were deposited on mica surface using 12mM Mg^{2+} containing 1X TAE buffer. After adsorption, the DNA origami are immobile on mica surface due to the strong binding of DNA origami to mica surface.

2. 700mM NaCl was added to the buffer, and the sample was incubated for 4 hours at 40 ℃. The monovalent cation was used to diffuse through the bridging layer between mica and DNA origami to weaken the binding so that the DNA origami become mobile on the surface. The mechanism of lattice formations was described in two steps such as immobilization of DNA origami on the surface by strong DNA to mica binding and diffusion of DNA origami by weak DNA to mica binding. This can be efficiently achieved by adjusting monovalent cation concentration to divalent cation concentration ratio in the reaction buffer.

3. After the lattice was formed, the diffusion of DNA origami was stopped by adding 1mM Ni^{2+} and gradually the NaCl concentration in the buffer was replaced by 12mM Mg^{2+}. Ni^{2+} was used to stop the mobility of DNA origami on mica surface since Ni^{2+} binds DNA to mica stronger than Mg^{2+}.

In surface assisted crystal like an assembly of DNA origami nanostructures, Rafat et al., [65] studied the effect of monovalent cations further in detail with regular noninteracting DNA origami triangle, rectangles and blunt end stacking cross tile structures. Noninteracting DNA origami triangle and rectangles organize into large-scale lattices in the presence of Na^+ cation. Depends upon the symmetry of shape in DNA origami, the quality of the lattice differs. For example, the number of point defects is very less in triangular DNA origami than in long rectangle and cross tiles. Twist corrected cross-shaped tiles also assemble into very large lattices by blunt end stacking. 200mM NaCl in 1X $TAE/MgCl_2$ buffer was used in this approach to induce the mobility of DNA origami on mica surface. Importantly, NaCl concentration more than 200mM resulted in the loosely packed

28

lattice and DNA origami desorption from the surface. In the case of twist corrected seeman tiles, after the DNA origami adsorption, the mica surface was incubated overnight with the solution of 1X TAE buffer/12.5 mM Mg^{2+} and 400 mM Na^+ to improve the crystal formation.

Another important strategy using lipid bilayer assisted micrometer-sized crystal like assembly of DNA origami structures was studied by Suzuki et al., [63]. A mica supported zwitter ionic lipid bilayer was used to create blunt end staking and close packing mediated self-assembly of DNA origami lattices. The interaction of DNA origami on lipid bilayer was found to be weaker than on mica surface which promotes the diffusion of DNA origami laterally in the presence of high Na^+ concentration. The authors highlighted the real-time observation of DNA origami adsorption, diffusion, defects filling and desorption of DN origami at high Na^+ concentration during the formation of the lattice. To improve the periodicity and reduce the stacking interaction, additional poly T sequences were introduced in the twist corrected cross tiles which ultimately reduced the number of defects in the lattice.

1.8.2 Directed adsorption of DNA origami on surfaces

Patterning of DNA molecules into microarrays has already been studied for the purpose of genome mapping and gene expression using fluorescent labeling techniques[170]. Precisely positioned whole gene sequences may have an advantage of simultaneous analysis of multiple gene targets. In that context, Gad et. al., demonstrated a conventional lithography approach to stretch a lambda DNA molecule on mica by molecular combing [171]. In the case of DNA origami, it is used as a mask or a substrate to create patterns. Gallego et.al, [172] reported that a DNA ink on gold substrates can be attached using a pattern on DNA origami with thiol sequences. When the DNA origami substrate that carries the ssDNA linkers or 'DNA ink' is denatured using NaOH, the available pattern on the gold surface can directly be further modified with gold nanoparticles.

29

A simple approach to create DNA origami patterns on a surface using thiolated DNA origami tubes was demonstrated by Ding et.al.,[173] The end-thiolated DNA six-helix bundles connect the gold islands prepared by e-beam lithography, after overnight incubation and create the pattern according to the position of gold islands. Gao et.al., [174] reported a protocol to create well-ordered DNA rafts on substrates. e-beam lithography assisted patterns on PMMA was first created and further functionalization of APTES anchor pads on patterns help in precise adsorption of DNA molecules on the patterns.

Gerdon et.al., [175] studied selectivity and control in DNA origami adsorption which is an important criterion in lithographic approach. DNA origami was adsorbed on carboxylic acid and hydroxyl group-terminated SAMs on gold surface patterns. The carboxylic acid-terminated surface results in better immobilization than the hydroxyl-terminated SAM. The DNA origami surface was further utilized to specifically deliver gold nanoparticles by hybridization. Kershner et.al,[176] reported a method to add more specificity in placement and orientation of DNA origami adsorption on surfaces. Using trimethyl silyl as a template layer, hydrophobic background and hydrophilic binding sites were created using oxygen plasma cleaning. The yield of single origami bound and oriented was 88%. Gopinath et.al.,[177] demonstrated a detailed study on the placement of DNA origami on SiO_2 substrates. typically, few crucial factors such as the influence of DNA origami concentration, $MgCl_2$ concentration, and pH in DNA origami orientation is reported. Importantly Gopinath et.al., [178] successfully used the precision in positioning DNA origami nanostructures in photonic crystal cavities to vary the emission intensities for the hybrid nanophotonic device manufacturing.

2. Structural stability of DNA origami nanostructures in the presence of chaotropic agents

2.1 Introduction

DNA origami represent powerful platforms for applications in nanotechnology, biophysics, and structural biology, single-molecule investigations of biomolecular processes. Among many potential applications of DNA origami as nanoscale platforms,[68–71,179,180] they are particularly attractive to monitor triggered conformational changes[181,182] in single biomolecules.[183–185] One very prominent example of such conformational changes are protein folding studies using single-molecule Förster Resonance Energy Transfer (smFRET).[182,186–188]. Protein immobilization on DNA origami would allow for the investigation of protein subpopulations and conformational dynamics of complex and heterogeneous protein folding scenarios such as folding networks as well as the study of distance-dependent protein-folding effects; folding scenarios that are otherwise extremely hard if not impossible to address.

A critical factor to consider when conducting protein conformation dynamics studies on DNA origami substrates is the exposure of the protein-decorated DNA origami to chaotropic denaturants. Biological macromolecules are structurally stabilized by the interface called hydration shell or solvation shell around them in water. Chaotropic agents disrupt this hydration shells by breaking hydrogen bonds, Van der Waals interactions and introduces the core structure to water molecules that weakens, destabilizes the hydrophobic effect [189,190] and promotes denaturation. However, urea and GdmCl may also interfere with DNA in a similar way as with proteins by disrupting native hydrogen bonding or hydration shells, of which both are crucial for double-stranded (ds) DNA formation.[191] Consequently, exposure of dsDNA to urea or GdmCl may induce denaturation of the

31

duplex. Indeed, it was shown that the melting temperature (T_m) of genomic dsDNA decreases linearly by 2.25°C per molar increasing urea concentration.[192] Nevertheless, the effect of urea and GdmCl on the stability of more complex DNA structures like DNA origami has to date not been investigated, and the question boils down to whether DNA origami maintain their structural integrity as molecular breadboards in the presence of high concentrations of chemical denaturants.

Therefore, we have exposed 2D DNA origami triangles as designed by Rothemund[46] to buffers containing different concentrations of urea or GdmCl and monitored their structural integrity in dependence of temperature. These triangular DNA origami are structurally more rigid than many other 2D DNA origami designs and feature only a few exposed base pairs which reduce their tendency to aggregate.[46] The DNA origami triangles thus represent well-suited platforms for single-molecule experiments.[73,84,193–197] Melting curves analysis by fluorimetry to report on global melting of DNA origami and atomic force microscopy (AFM) were employed to visualize nanoscale alterations in the DNA origami superstructure. We find that the DNA origami are stable at room temperature in both denaturants at concentrations as high as 6 M. At elevated temperatures, however, DNA origami degradation is observed with the bridging staples that connect the trapezoidal domains being most susceptible toward denaturant attack. Importantly, our results reveal that the structural integrity of DNA origami depends crucially on variations in melting temperature of the individual staple strands. Therefore, the global melting temperature of the DNA origami as measured by bulk fluorimetry does not represent an accurate measure of DNA origami stability. By rational design of the arrangement and lengths of the individual staple strands used for the folding of a particular shape, however, the structural stability of DNA origami may be tailored toward specific applications. Considering their stability at room temperature, the triangular DNA origami can be readily employed as platforms in the study of biomolecular processes that

rely on the presence of chaotropic denaturants, e.g., single-molecule protein folding studies using urea or GdmCl as denaturing agents.

2.2 Methods

DNA origami synthesis. The triangular DNA origami were synthesized as previously described.[194] Briefly, the 7249 bp long M13mp18 genome (Tilibit) was folded by thermal annealing into the triangular shape using 208 staple strands (Metabion and Biomers) with lengths ranging from 22 to 43 nt in 1xTAE buffer (Calbiochem) containing 10 mM $MgCl_2$ (Sigma-Aldrich). After assembly, origami were purified by centrifugal filtration (Amicon Ultra, 100K, Millipore) and washing with 1xTAE/Mg^{2+} to remove excess staple strands.

AFM imaging. Urea and GdmCl stock solutions with four different concentrations (1 M, 2 M, 4 M, and 6 M) were prepared in 1xTAE/Mg^{2+}. DNA origami triangles (5 nM) were incubated in these stock solutions for $1 - 24$ h at four different temperatures (23°C, 30°C, 37°C, 42°C) using a thermocycler Primus 25 advanced (PEQLAB). After incubation, 5 µL of DNA origami sample were mixed with 50 (1 M and 2 M denaturant concentration) or 100 µl (4 M and 6 M denaturant concentration) of 1xTAE/Mg^{2+} buffer and adsorbed on freshly cleaved mica for 15 minutes. Due to the viscosity of the denaturing agents at high concentration, the samples were diluted stronger for 4 M and 6 M concentrations and the adsorption time on mica was extended to 30 minutes. The immobilized DNA origami were washed carefully with plenty of ultrapure water and dried in a stream of ultrapure air for AFM imaging. The images were obtained in intermittent contact mode with an Agilent 5100 AFM and HQ: NSC18/Al BS cantilevers (MikroMasch). For the statistical analyses, up to 496 individual DNA origami have been evaluated for each experimental condition.

2.3 Results and Discussion

In the first set of experiments, the stability of DNA origami is probed in the presence of the chemical denaturants urea and GdmCl using thermal melting analysis. To this end, a real-time fluorimetric monitoring is set using SYBR green as a reporter dye whose fluorescence intensity is 1000-fold increased when bound to dsDNA [96]. This assay reports on dsDNA dissociation as a function of temperature and thus serves as a global probe of DNA origami duplex integrity. Melting profiles of DNA origami triangles in 1xTAE buffer supplemented with 10 mM $MgCl_2$ and varying concentrations of urea and GdmCl are obtained. An increasing denaturant concentration leads to a decrease in the global melting temperature (T_m). In particular, urea lowers T_m from 73°C at 0 M to 56°C at 6 M urea. For GdmCl, we observe an even stronger shift down to 37°C at 6 M GdmCl. Plots of melting temperatures as a function of denaturant concentration reveal a linear decrease in T_m with denaturant. Increasing concentrations of urea lower T_m by 2.76°C M^{-1}, in very good agreement with the reported value of 2.25°C M^{-1} observed for genomic dsDNA melting in the absence of Mg^{2+} ions. Interestingly, GdmCl impacts the global T_m by a decrease of 5.84°C M^{-1}. From protein unfolding studies, GdmCl is known to be approximately $2 - 3$ times more effective than urea in denaturing proteins depending on the polarity of buried polypeptide residues.[198] Such a relative effectiveness in global melting apparently also holds true for DNA origami melting by urea and GdmCl. More importantly, the results indicate that DNA origami when exposed to 6 M of either denaturant exhibit substantial stability at moderate temperatures (e.g., room temperature), suggesting that DNA origami maintain their integrity also in the presence of high denaturant concentration.

To investigate the effects of the denaturants on the structural integrity of the DNA origami at a single-molecule level, AFM has been employed. Figure 4 shows AFM images of the DNA origami triangles after 1 h incubation in solution at different concentrations of urea and at different

34

temperatures. At 23°C, structurally intact triangles are observed for all urea concentrations ranging from 1 M to 6 M. At 30°C incubation temperature, intact DNA origami triangles are observed up to a urea concentration of 4 M. For 6 M urea. However, some of the DNA origami are noticeably damaged. Although the original triangular shape can still be recognized, most of the triangles have been disrupted at the corners (see zoomed images in the right column). At 37°C and 6 M urea, the overall shape of the DNA origami is completely destroyed and has adopted a somewhat molten topology that in few cases still resembles a (strongly distorted) triangular shape. Increasing the incubation temperature to 42°C leads to further degradation of the DNA origami in 6 M urea. Under these conditions, the formerly triangular structures appear crumpled without any similarity to the original shape. Note that the observed structures are still composed of dsDNA since single strands cannot be resolved by AFM. At lower urea concentrations, however, the DNA origami are still intact at 42°C. In the case of GdmCl (Fig. 5), we observe similar trends as for urea, *i.e.*, the DNA origami are stable in 1 M and 2 M GdmCl up to at least 42°C. At 4 M GdmCl, the first partially degraded DNA origami are observed at 37°C. Although the damaged DNA origami still have their triangular shape after exposure to GdmCl, the connections between the three trapezoids that comprise the triangle are broken. At 42°C, some of the DNA origami cannot maintain their triangular shape and collapse.

Interestingly, most of the collapsed structures still consist of three intact trapezoids that are still connected to each other, similar to the type of damage observed in 6 M urea at 30°C. For a concentration of 6 M GdmCl, DNA origami degradation already starts at 30°C. However, DNA origami are still structurally intact at 23°C. At 37°C, all the triangles are completely disintegrated with the trapezoids having lost their structural integrity, and the DNA origami appear shredded. At 42°C, the DNA origami have shrunken into irregular structures and appear to have lost a significant amount of material.

The melting curve for 6 M urea yields a mean melting temperature of 56°C with the low-temperature slope extending down to about 45°C. Hence, one would not expect any pronounced effect on the DNA origami structure at incubation temperatures below 40°C.
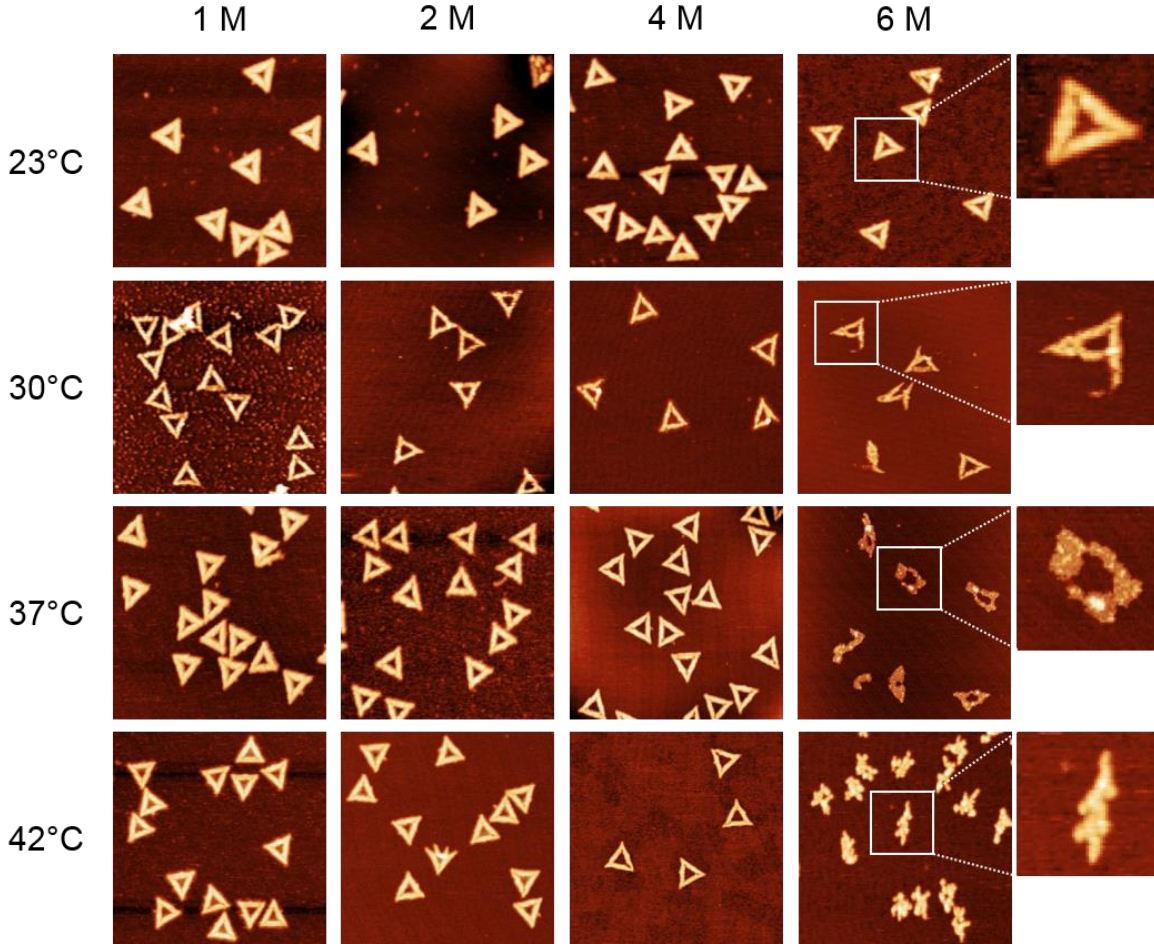
Figure 4. AFM images of DNA origami triangles after 1 h incubation in urea at different concentrations and temperatures. Overview images and zooms have a size of 1 x 1 and 0.2 x 0.2 µm², respectively. Height scales are 2.3 nm.[96]

In contrast, however, the AFM images reveal significant structural degradation already at 30°C, although the DNA origami tend to maintain their original shape (figure 4). Most likely, this discrepancy originates from local variations in the melting temperatures of the individual staple

strands in the DNA origami, which have been reported to exhibit a broad distribution of melting temperatures.[161,199] A significant fraction of the staple strands with the lowest melting temperatures will, therefore, dehybridize from the scaffold already well below the global melting temperature of the DNA origami (note the definition of the melting temperature as the temperature at which 50 % of the duplexes have dehybridized and exist as single strands). The other strands remain largely in place but are unable to preserve the overall shape of the DNA origami. With increasing temperature, more staple strands dehybridize from the scaffold until the entire structure collapses.

In this context, it is particularly interesting that both denaturants seem to preferentially attack the corners of the triangles and induce the breakage of the connections between the individual trapezoids (cf. figures. 4 and 5). From a structural point of view, these corners have some peculiar features[46] (see inset in figure. 6) that may be responsible for this effect. First, each trapezoid is composed of nine parallel double helices. Therefore, the corners of the triangle are the only sites that exhibit exposed base pairs. Second, each trapezoid is connected to the other two via one scaffold crossover and four bridging staple strands. Due to residual twist strain, each trapezoid will adopt a curved shape in solution, so that these bridges may experience significant mechanical stress. Third, in order to account for the different gaps between the helices of neighboring trapezoids, three of the bridging staples feature up to three unpaired thymines. Furthermore, a closer inspection of the bridging staples reveals that those are the shortest staples in the entire DNA origami triangle with a (hybridized) length of 22 nucleotides (nt). Thus, these staples can be expected to have rather low melting temperatures.

In order to further elucidate the role of the bridging staples, we have calculated the melting temperatures of all staple strands in the DNA origami triangle using the DINAMelt web server[200] in the absence of denaturants. For simplicity, each staple strand has been treated as a single

37

continuous hybridization domain in these calculations. In the assembled DNA origami, however, each staple strand consists of at least two independent segments that hybridize with spatially separated complementary sequences of the scaffold.
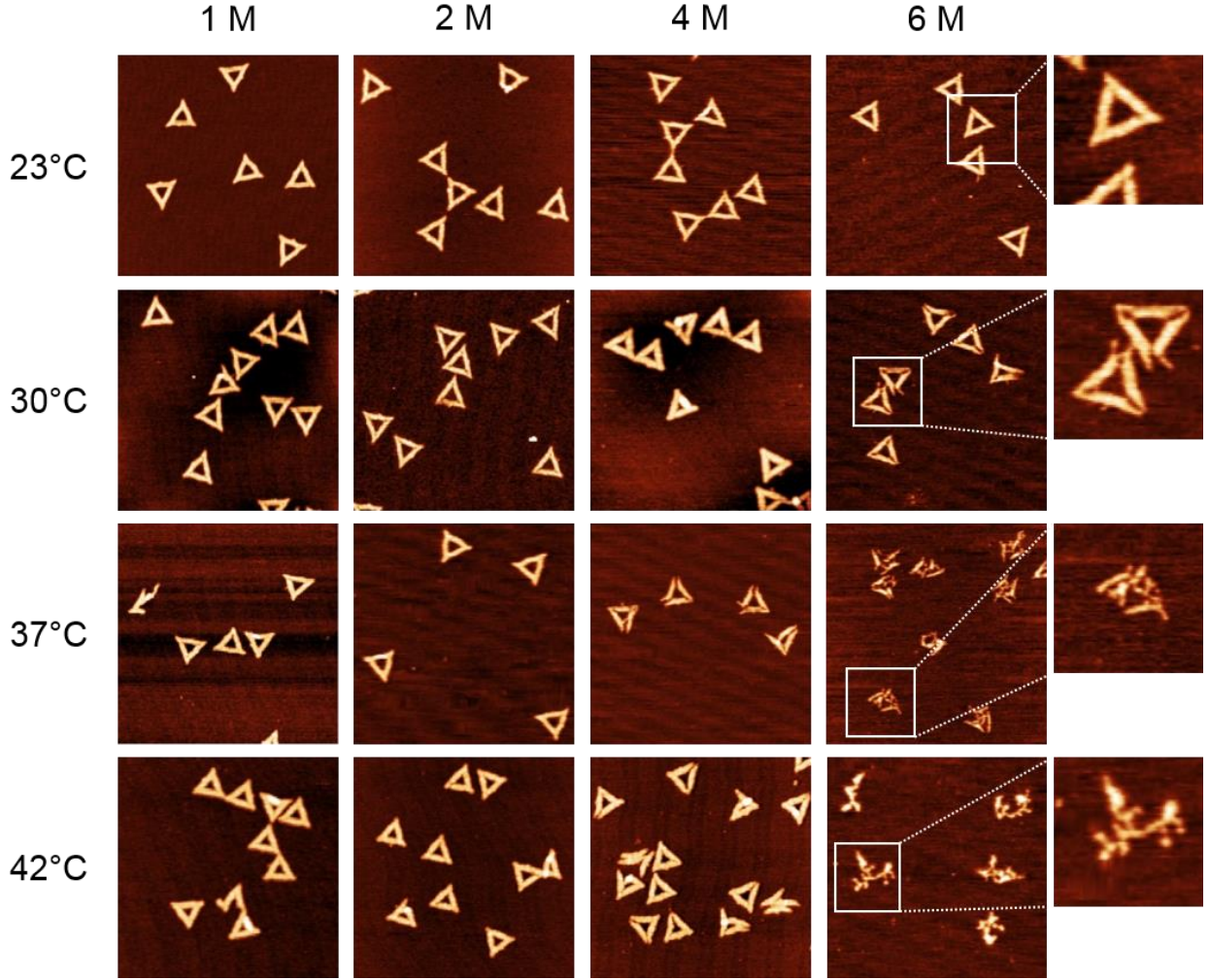

Figure 5. AFM images of DNA origami triangles after 1 h incubation in GdmCl at different concentrations and temperatures. Overview images and zooms have a size of 1 x 1 and 0.2 x 0.2 μm², respectively. Height scales are 2.3 nm.[96]

The resulting T_m distribution in figure. 6, therefore, represents only a coarse approximation which agrees surprisingly well with the fluorimetric melting curve[96]. Indeed, figure. 6 reveals that while virtually all trapezoid staples have calculated melting temperatures between 45°C and 85°C, four

38

of the twelve bridging staples have melting temperatures below 45°C with the lowest melting temperature being only 32.6°C. These calculations support our observation that the denaturants first compromise the stability of the corners of the triangles before degrading the trapezoids.
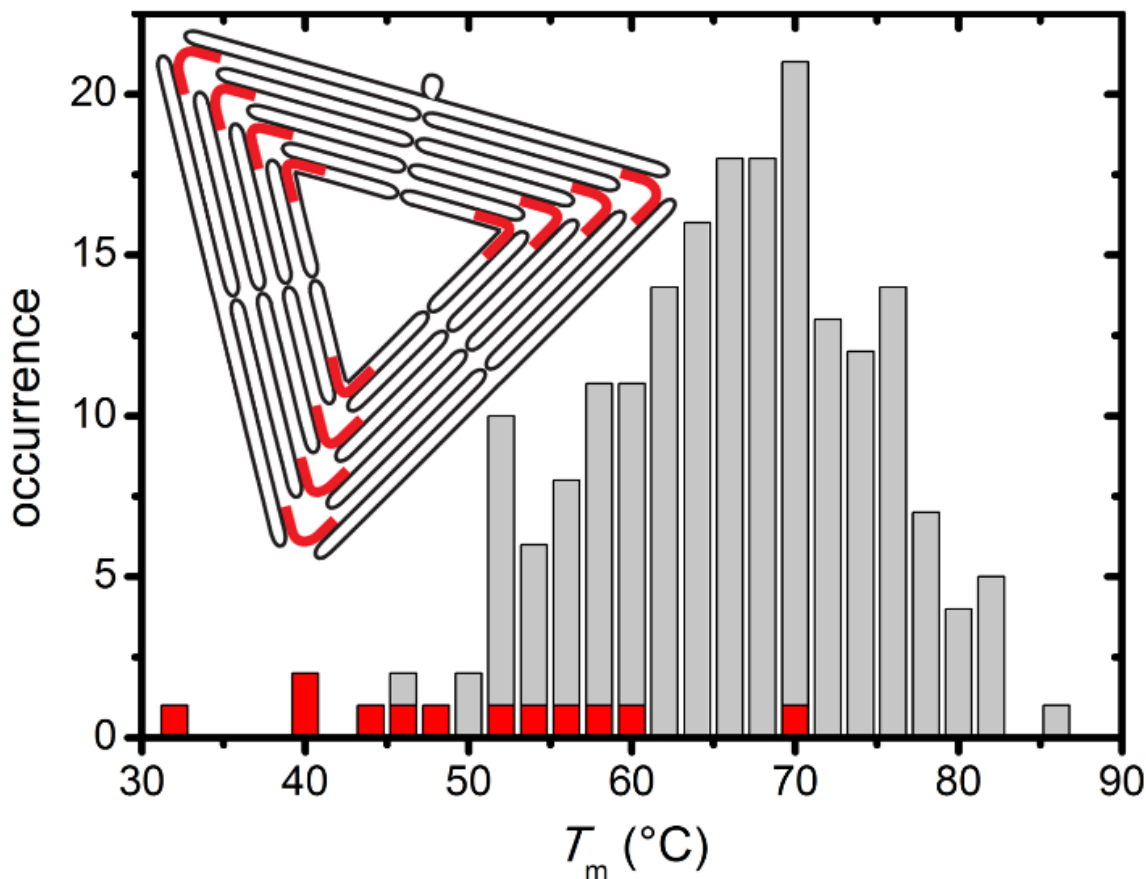
Figure 6. Melting temperature distributions of the trapezoid (grey) and bridging staples (red), respectively. The inset schematically shows the folded scaffold (black) in the triangular DNA origami and highlights the positions of the 12 bridging staples (red). [96]

In comparison to the distribution in figure. 6, narrower T_m distributions were previously reported for a rectangular DNA origami design.[161,199] In particular, no staple strands with melting temperatures below 50°C were identified in the rectangular DNA origami. Therefore, we speculate that these rectangular DNA origami exhibit a sharper denaturation transition at higher temperatures than the triangles. On the other hand, our results suggest that the stability of the DNA origami

triangles in the presence of urea and GdmCl can be further enhanced by the rational redesign of the bridging staples. Statistical analysis of the AFM images allows further quantification of the denaturant effects. Figures 7 and 8 show the relative occurrence of intact, structurally compromised, and heavily damaged DNA origami after incubation with urea and GdmCl, respectively. In this context, intact refers to DNA origami with an evidently uncompromised triangular shape. Structurally compromised refers to DNA origami nanostructures which still have a clear triangular shape that is, however, visibly compromised, e.g., in the form of partially disconnected trapezoids. Heavily damaged, on the other hand, refers to DNA origami that have lost their original triangular shape as observed for instance in figures. 4 and 5 at 6 M concentration and temperatures of 37°C and 42°C. This category also includes DNA origami fragments that are sometimes observed even in the absence of denaturing agents. Below 6 M urea, we observe that the vast majority, *i.e.*, $80 - 100\,\%$, of the DNA origami are intact, even at 42°C (figure. 4). At 6 M urea, DNA origami remain intact at 23°C while at higher temperatures, a significant fraction of structurally compromised and damaged DNA origami is found. At 30°C, the fractions of structurally compromised and heavily damaged DNA origami both increase to approximately 25 % each. At 37°C and 42°C, all DNA origami nanostructures are heavily damaged without any intact or even compromised structures present.

The statistical analysis in figure. 7 reveals that DNA origami remain stable at 23°C up to 6 M GdmCl. Nevertheless, at elevated temperatures, GdmCl damages the DNA origami at much lower concentrations than urea. Already at 1 M GdmCl and 42°C, about 25 % of the DNA origami are structurally compromised or heavily damaged. This tendency is further substantiated at 2 M GdmCl, and in the presence of 4 M GdmCl, almost 50 % of the DNA origami are structurally compromised at 37°C. At 42°C, we find almost equal fractions of intact, structurally compromised, and heavily damaged DNA origami. The harshest condition of 6 M GdmCl results in a fraction of

40

structurally compromised DNA origami peaking at 30°C, while at 37°C and 42°C, only heavily
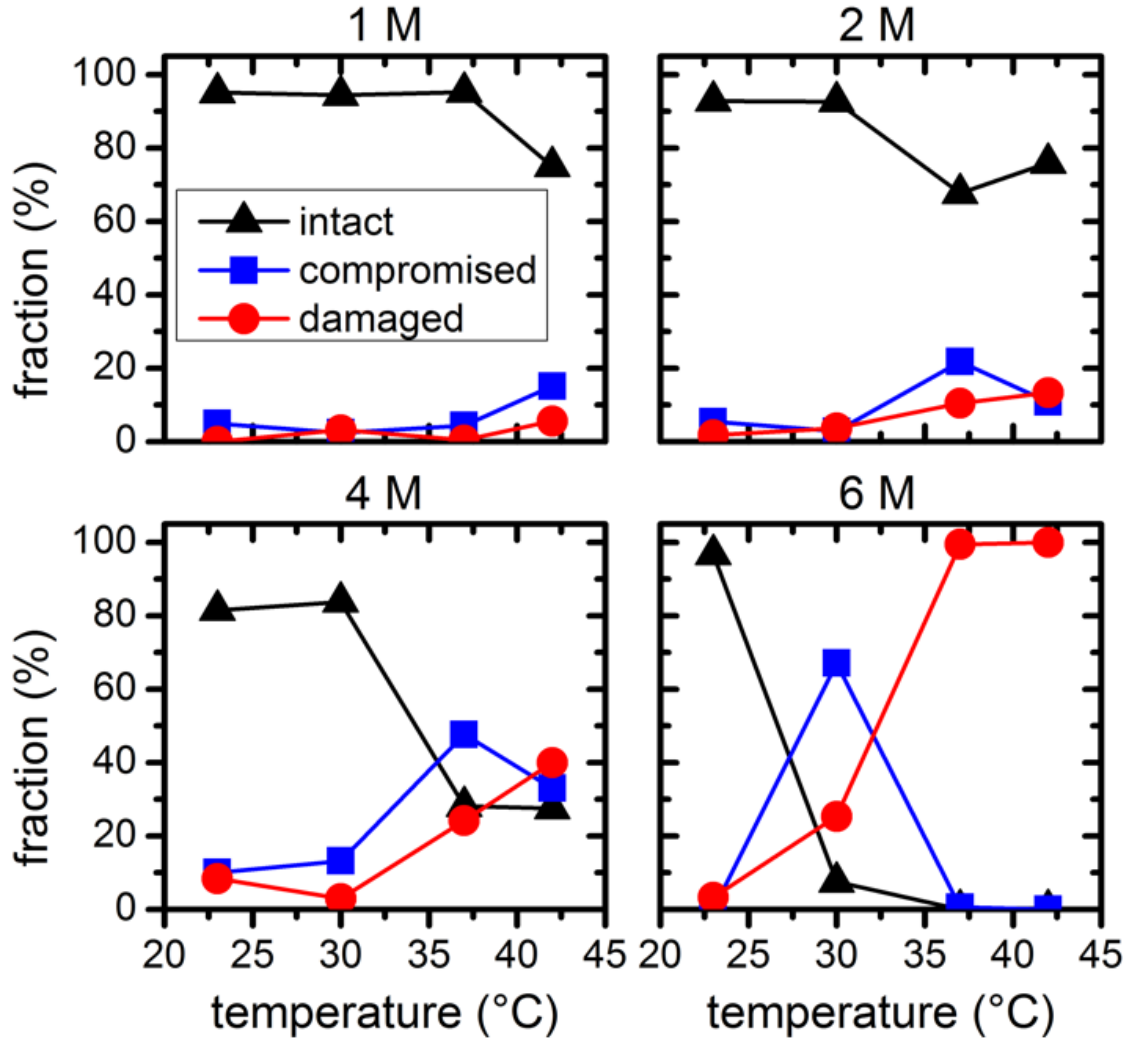
damaged DNA origami are observed.
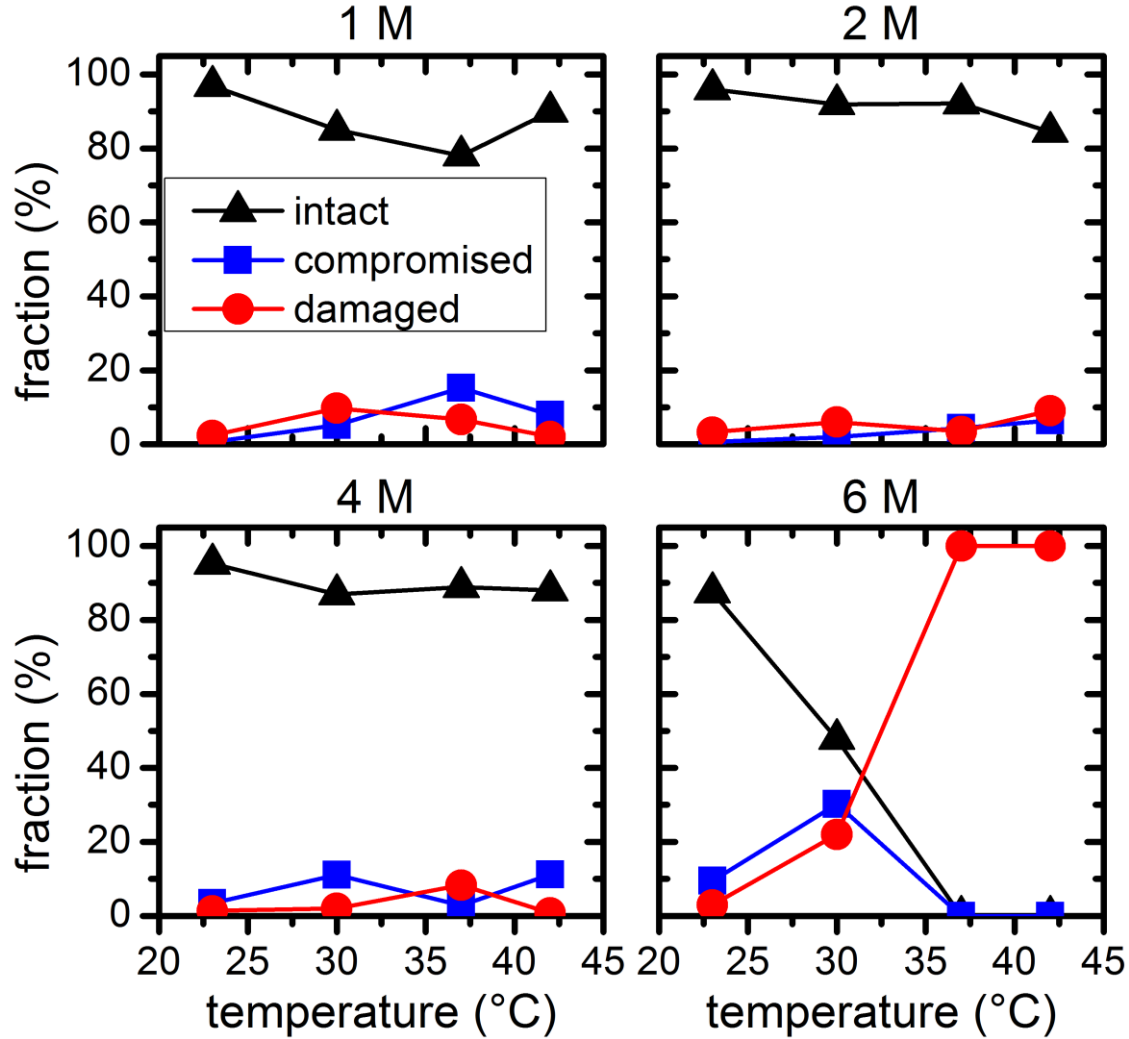
Figure 7. Relative fractions of intact, structurally compromised, and heavily damaged DNA

origami after 1 h incubation with urea at different concentrations and temperatures.[96]

The shift of visible DNA origami degradation to lower concentrations in comparison to urea

denaturation agrees qualitatively with the stronger decrease of the melting temperature per molar

GdmCl observed in melting curve analysis.

Comparing the ensemble melting curves for the two different denaturants in melting curve analysis[96], we can identify a similar melting temperature $T_m \approx 57°C$ for DNA origami in 6 M urea or 2 M GdmCl.

Figure 8. Relative fractions of intact, structurally compromised, and heavily damaged DNA origami after 1 h incubation with GdmCl at different concentrations and temperatures.[96]

Hence, one would expect that the DNA origami exhibit also a similar degree of structural degradation at these conditions. However, both, the corresponding AFM images in figures. 4 and 5 and the statistical action. In the case of 6 M urea, incubation at 37°C results in the complete

destruction of all DNA origami nanostructures in the sample (figure. 7). For 2 M GdmCl at the same temperature, however, more than 70 % of intact origami are observed (figure. 8). The reason for this enhanced structural stability in the stronger denaturant may originate from the ionic nature of GdmCl which, at such high concentrations, could stabilize the superstructure of the DNA origami.
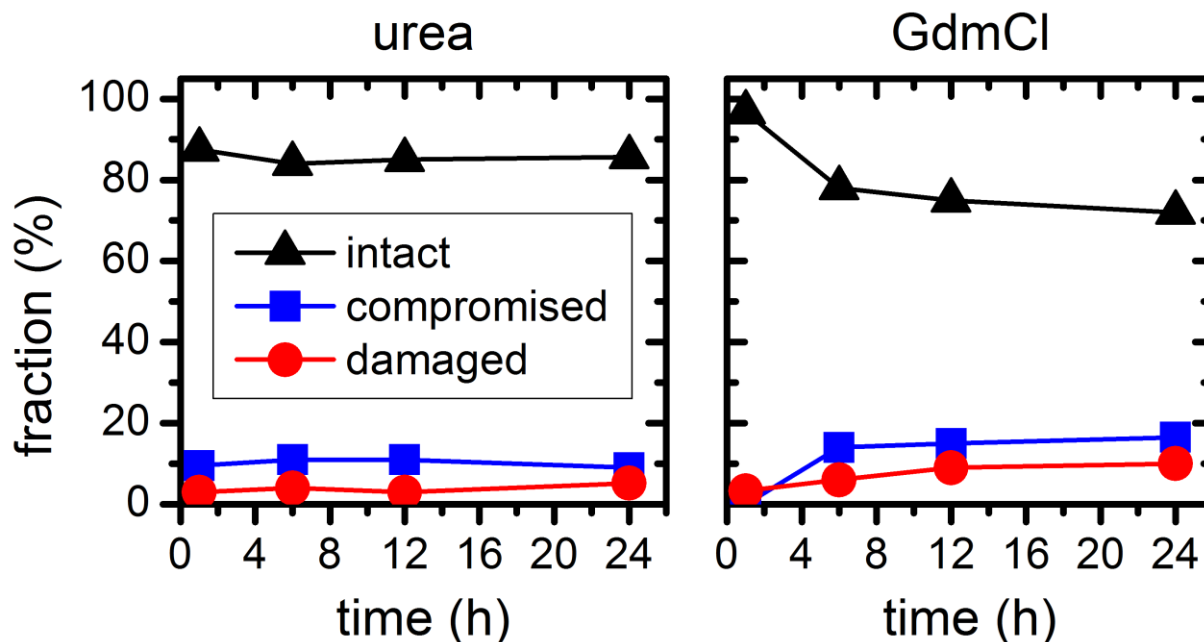
Figure 9. Relative fractions of intact, structurally compromised, and heavily damaged DNA origami after incubation with 6 M urea and GdmCl, respectively, at 23°C and increasing incubation times.[96]

In above experiments, the DNA origami remained largely intact even at denaturant concentrations of 6 M at 23°C temperature. To evaluate their long-term stability under these conditions, we have extended the incubation times up to 24 h . In the case of 6 M urea, the relative fractions of intact, structurally compromised, and heavily damaged DNA origami remain constant also at longer incubation times, with the fraction of intact DNA origami fluctuating around 85 % (figure. 9). For incubation with 6 M GdmCl, however, the fraction of intact DNA origami decreases from 97 %

after 1 h incubation to 78 % after 6 h. Longer incubation times result in a saturation of the fraction of intact DNA origami saturates at about 73 % (figure. 9). Although these results show that the GdmCl attack occurs on a rather long-time scale, the vast majority of DNA origami nanostructures remains intact also for extended periods of time, thereby enabling long-term experiments with DNA origami substrates under strongly denaturing conditions.

2.4 Denaturation of biotin-streptavidin complex on DNA origami

The biotin-streptavidin[201] complex is the strongest interaction known in molecular biology. Due to their high resistance to temperature[202–204], mechanical stress[205,206], denaturing agents induced denaturation[207–209], streptavidin-biotin complex has been widely used in chemical and biotechnological applications[210], e.g., surface coating for immunoassays. As a proof of concept that our experimental finding of DNA origami can be used as a platform for controlled denaturation of biomolecules in the presence of denaturing agents, an experiment was designed to study the chaotropic agent-induced denaturation of the biotin-streptavidin complex on DNA origami using 6M GdmCl.

DNA origami were synthesized[46] with three additional biotinylated staples (5'-(GCC)5-3' attached to t1s4i, t1s24i, t1s14i) . After purification, 30nM DNA origami in 1XTAE was incubated overnight with 300nM freshly prepared streptavidin in the same buffer. To quantify the yield of streptavidin bound biotinylated DNA origami, the sample was then adsorbed on mica and imaged under AFM. Figure 11 shows the AFM image of streptavidin functionalized DNA origami triangle at three positions. Minimum 200 origami were count for the statistical analysis of biotin-streptavidin complex on DNA origami and 97% streptavidin functionalization was achieved.
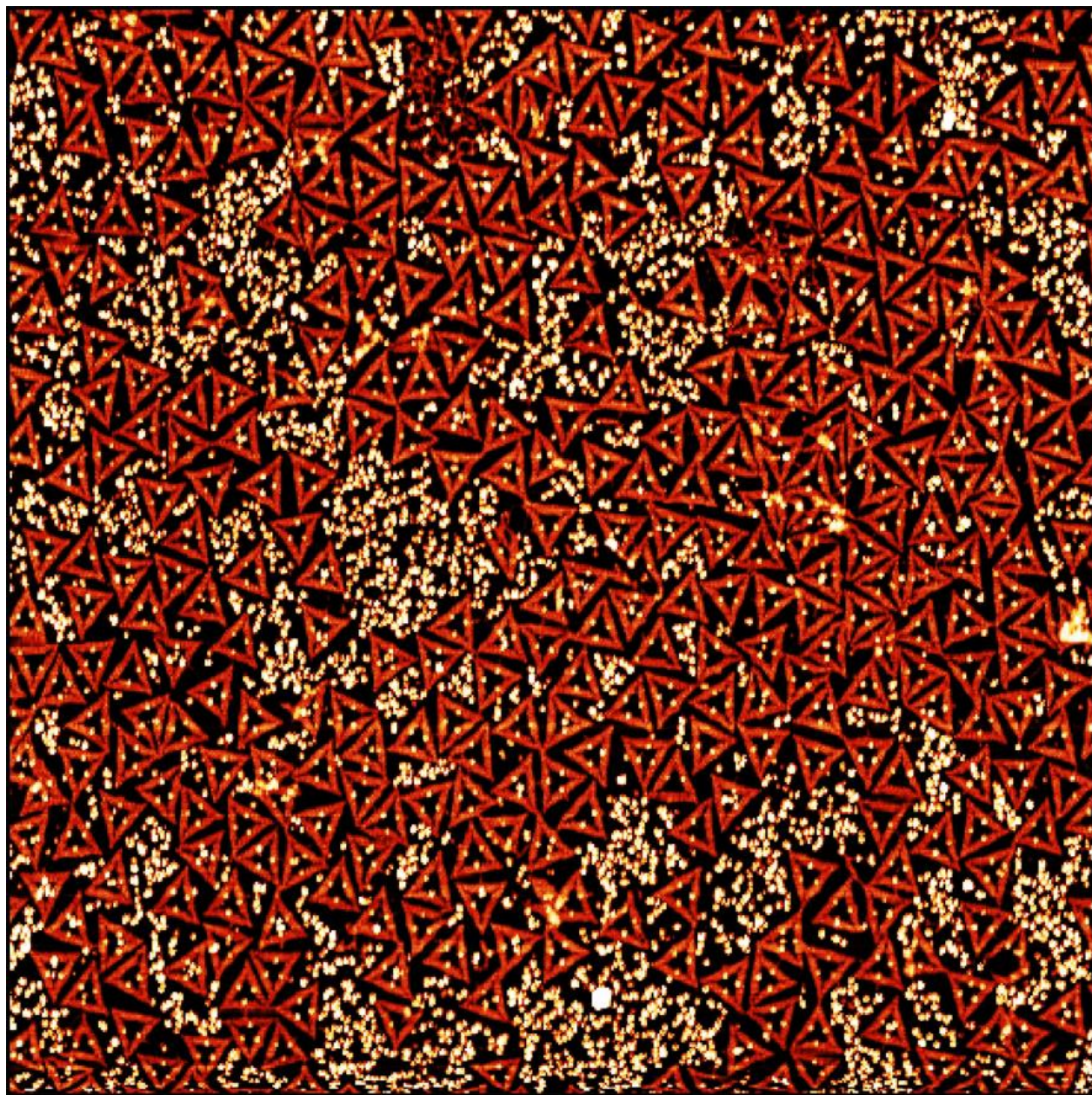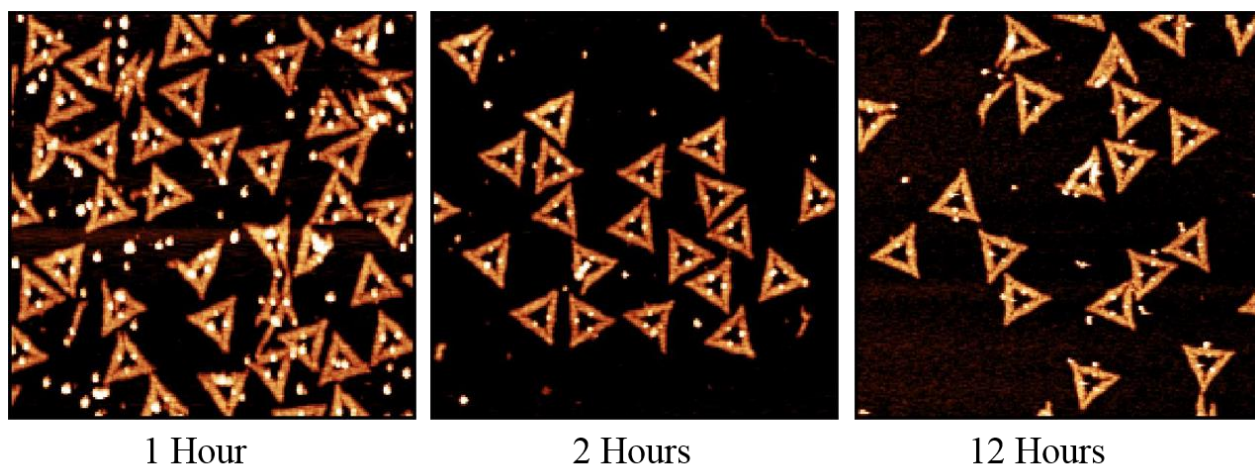
Figure 11. AFM image of streptavidin modified DNA origami triangles at three positions Image has a size of 3 x 3 µm². Height scale is 4 nm.

In the second step, without filtering the excess of streptavidin, three identical working solutions were prepared to study the time-dependent denaturation of the biotin-streptavidin complex at room temperature. 5nM DNA origami was mixed with 6M GdmCl in 1XTAE buffer and incubated at

room temperature. At three-time intervals (1 hour, 2 hours, 12 hours) samples were adsorbed on mica and imaged under AFM for statistical analysis.

Gonzalez et al.,[203,204] reported that, during thermally induced denaturation, the individual melting temperature for unliganded streptavidin in phosphate buffer is 73°C . Upon binding and fully ligand saturation, biotin increases the melting temperature of the streptavidin to 112°C. The maximum temperature that we can use in our experiment to maintain the increased percentage of intact origami is room temperature. However, due to the high stability, the streptavidin-biotin complex remained undisturbed even at 6M GdmCl concentration. The percentage of streptavidin bound DNA origami after 1 hour, 2 hours and overnight treatment with 6M urea is 90 %, 90.66%, 88 % respectively.

1 Hour   2 Hours   12 Hours

Figure 12. AFM images of DNA origami triangles after 1 hour, 2 hours, 12 hours incubation in 6M GdmCl at 23°C. Overview images have a size of 1.1 x 1.1 µm². Height scales are 3 nm.

Figure. 12 shows the AFM images of 6M GdmCl treated biotin-streptavidin modified DNA origami triangles at different time intervals. Only at 1 hour, 6 % percentage denaturation of the biotin-streptavidin complex was observed (figure 13). This trend did not increase even after the overnight treatment.

46
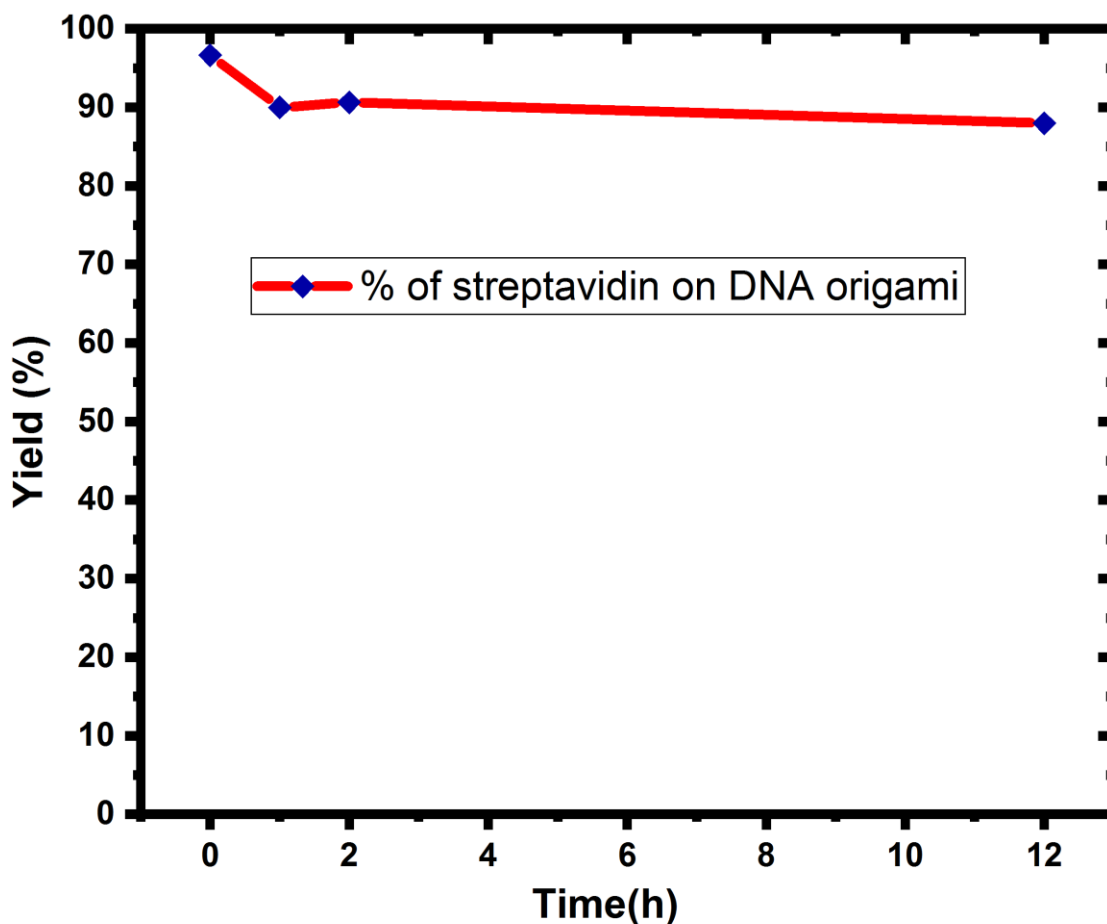
Figure 13. Yield of bound streptavidin per biotin on DNA origami after 1 hour, 2 hours, 12 hours incubation with 6M GdmCl at 23°C.

However, the origami were found intact along with the biotin-streptavidin complex. One possible experimental approach in this path is to introduce further entangling of temperature sensitive or denaturant sensitive proteins on the biotin-streptavidin complex for denaturation studies.

2.5 Conclusions

In summary, we have investigated the stability of the triangular DNA origami design by Rothemund[46] in the presence of two chaotropic denaturants by fluorimetry and AFM. Exposure to

both, urea and GdmCl, leads to a reduction of the melting temperature of the DNA origami. For urea, we observed in ensemble experiments a reduction by $2.76°C$ M^{-1}, while GdmCl leads to a reduction by $5.84°C$ M^{-1}. Strikingly, a comparison of the fluorimetry and single-molecule AFM data showed that the global melting temperature is not an adequate measure of the DNA origami's structural integrity. The latter strongly depends on the distribution of the melting temperatures of the individual staple strands. For the DNA origami triangle, we found that the bridging staples connecting the trapezoids have comparatively low melting temperatures and thus are particularly sensitive toward denaturant attacks. The dehybridization of those bridging staples leads to the collapse of the triangular shape with the trapezoids remaining largely intact. Thus, pure ensemble melting curve measurements tend to overestimate the stability of the DNA origami nanostructures.

At a given temperature, different degrees of structural damage were observed for urea and GdmCl concentrations that result in almost identical melting curves. Although GdmCl has a stronger effect on the global melting temperature, its attack results in less structural damage than observed for urea, indicating a structural stabilization due to its ionic nature.

At concentrations up to 6 M, the triangular DNA origami are stable for at least 24 h in both denaturants at room temperature. At 4 M concentrations, the window of stability extends to temperatures between 30°C and 37°C, while at 2 M concentrations, the DNA origami remain largely intact up to temperatures of 42°C. DNA origami stability may, however, be further enhanced, for instance by photo-cross-linking[211] or by the rational redesign of the bridging staples toward higher melting temperatures. Hence, the compatibility of DNA origami nanostructures with high concentrations of denaturing agents qualifies them for numerous applications including single-molecule protein folding studies.

3. Cation-induced stabilization and denaturation of DNA origami nanostructures in urea and guanidinium chloride

3.1 Introduction

In the previous chapter, we have investigated the stability of DNA origami nanostructures in the presence of the denaturing agents urea and guanidinium chloride (GdmCl).[96] Interestingly, we found that the global melting temperature of DNA origami triangles decreases linearly with increasing denaturant concentration,[96] in excellent agreement with studies on genomic DNA.[212] However, the integrity of the nanostructure was more susceptible toward environmental conditions than their melting curves suggested. In particular, GdmCl was found to have a strong effect on the global melting temperature whereas its attack resulted in less structural damage than observed for urea under comparable conditions.[96]

The interaction of urea with nucleic acids is well studied and involves stacking interactions and hydrogen bonding of urea with the nucleobases, resulting in a reduction of the melting temperature T_m.[191,212–215] Less is known about DNA denaturation by GdmCl which has mainly been investigated with regard to its effect on protein structure.[198,216–219] In general, GdmCl is often a more potent denaturant than urea.[198,217] Due to its ionic nature, however, the denaturation efficacy of GdmCl depends strongly on electrostatic interactions with the biomolecule and is thus sensitive toward molecular structure and the ionic strength of the buffer medium.[216,217] This suggests that ionic strength may play a pivotal role in modulating the denaturation effect of urea and GdmCl on DNA origami nanostructures. In this chapter, we therefore investigate the effects of cation concentrations on DNA origami denaturation by urea and GdmCl. We find that increasing Na^+ and Mg^{2+}

concentrations lead to a structural stabilization of the DNA origami nanostructures in urea. However, surprisingly, both cations promote DNA origami denaturation by GdmCl.

3.2 Methods

Buffer solutions

A stock of 1 M Tris acetate (TA) buffer (pH 8.0) was prepared by dissolving Trizma base (Sigma Aldrich) in HPLC-grade water (VWR) and adjusting the pH to 8.0 using 100 % glacial acetic acid (Merck). 7 M urea (Amresco) and 4 M GdmCl (Amresco) working solutions were prepared with different NaCl and $MgCl_2$ (Sigma Aldrich) concentrations in 40 mM TA buffer. To avoid volume restrictions, urea and GdmCl stock solutions with 2.7 M NaCl and 2 M $MgCl_2$ were prepared and diluted with cation free buffer to yield lower concentrations.

DNA origami synthesis

Triangular DNA origami nanostructures[46] were synthesized as described previously[96] from the single stranded M13mp18 genome (Tilibit) and 208 staple strands (Metabion). Thermal annealing was performed in 40 mM TA buffer containing 10 mM $MgCl_2$. The resulting triangular DNA origami were spin filtered (Amicon Ultra, 100K, Millipore) in 40 mM TA buffer containing 10 mM Mg^{2+} and 200 mM Na^+, respectively, to remove excess staple strands.

AFM imaging

DNA origami were mixed with 7 M urea and 4 M GdmCl with different ionic strengths to yield a final DNA origami concentration of 5 nM and then incubated for 1 hour at 42°C in a thermocycler Primus 25 advanced (PEQLAB). After incubation, 5 µL of DNA solution were adsorbed on freshly cleaved mica with 100 µL of 1 x TAE/10 mM $MgCl_2$ for 30 minutes. The samples were then carefully washed with plenty of ultrapure water and dried in a stream of ultrapure air. The samples

were imaged in air with an Agilent 5100 AFM operated in intermittent contact mode using HQ:NSC18/AL BS cantilevers (MikroMasch). A minimum of 300 individual DNA origami were analyzed at each condition for statistical evaluation.

3.3 Results and Discussion

Mono and divalent metal cations are known to reduce electrostatic repulsion and stabilize secondary and tertiary structures of nucleic acids by increasing their melting temperature.[91,158,220,221] Due to the tight packing of DNA strands within DNA origami nanostructures, cation-mediated screening of electrostatic repulsion between neighboring helices is of particular importance to maintain structural integrity.
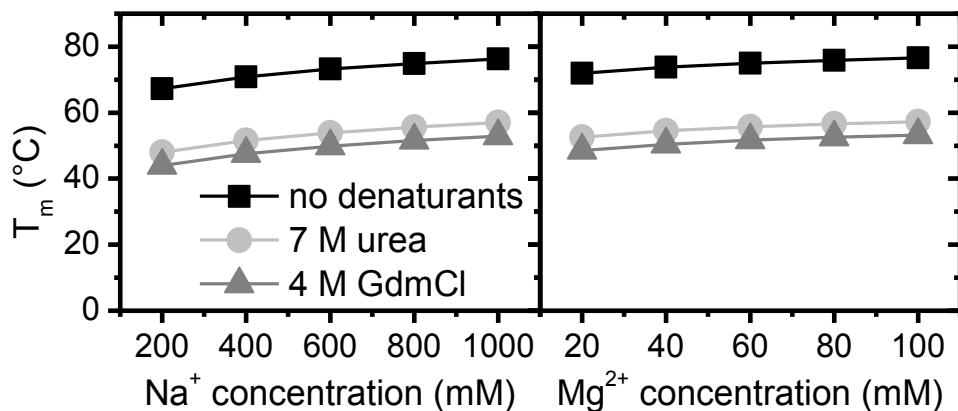
Figure 14. Calculated melting temperature of a representative staple strand (t-5s6e, GTGTGATAAGGCAGAGGCATTTTCAGTCCTGA) of the DNA origami triangle as a function of Na^+ (left) and Mg^{2+} (right) concentration, respectively.[222] T_m values without denaturants have been calculated using the DINAMelt web server.[200] Addition of 7 M urea and 4 M GdmCl is expected to result in an overall decrease of the T_m values by 19.3°C and 23.3°C, respectively, based on melting curve measurements.[96]

The expected melting temperature for a representative DNA staple strand increases with increasing Na^+ and Mg^{2+} concentrations (figure.14), while typically the stronger stabilizing effect of Mg^{2+} results in a similar T_m increase at 10-fold lower concentrations.[221] Based on our previous work, the global melting temperature of DNA origami nanostructures dropped by 2.76°C M^{-1} and 5.84°C M^{-1} for urea and GdmCl, respectively (figure.14).[96]

Consequently, in the absence of any additional effects, the denaturants would only lead to a reduction of the melting temperature values but not affect the general concentration dependencies (figure.14). However, we have found previously that global melting temperature analysis does not represent an accurate measure of DNA origami integrity and overestimates their structural stability.[96]

Nanostructural analysis, on the other hand, reports on DNA origami superstructure integrity and is able to detect environment-related structural effects.[92,93,96] Therefore, in this work, we carefully investigate the effect of NaCl and $MgCl_2$ on triangular DNA origami nanostructure stability using atomic force microscopy (AFM). In order to ensure precise control of the Na^+ and Mg^{2+} concentrations, all experiments were conducted in Tris-acetate buffer (pH 8.0) without ethylenediaminetetraacetic acid (EDTA).

In a first set of experiments, we increased the NaCl and $MgCl_2$ concentrations while incubating the triangular DNA origami in 7 M urea for 1 h at 42°C, close to but below the global melting temperature.[96] AFM analysis (figure.15) reveals that at low ionic strength (200 mM NaCl or 20 mM $MgCl_2$), this treatment leads to almost complete denaturation of the DNA origami in accordance with our previous experiments.[96] Increasing the cation concentrations results in gradual nanostructure preservation. At 600 mM NaCl or 60 mM $MgCl_2$, most DNA origami have a well-defined albeit damaged triangular shape. Further increase of the ionic strength to 1000 mM NaCl

or 100 mM MgCl$_2$ leads to additional stabilization with the majority of DNA origami remaining intact. In a statistical analysis of the AFM images, we quantified the fraction of structurally intact DNA nanostructures for each experimental condition. In this context, "structurally intact" refers to DNA origami triangles without any discernible distortions, holes or broken corners.
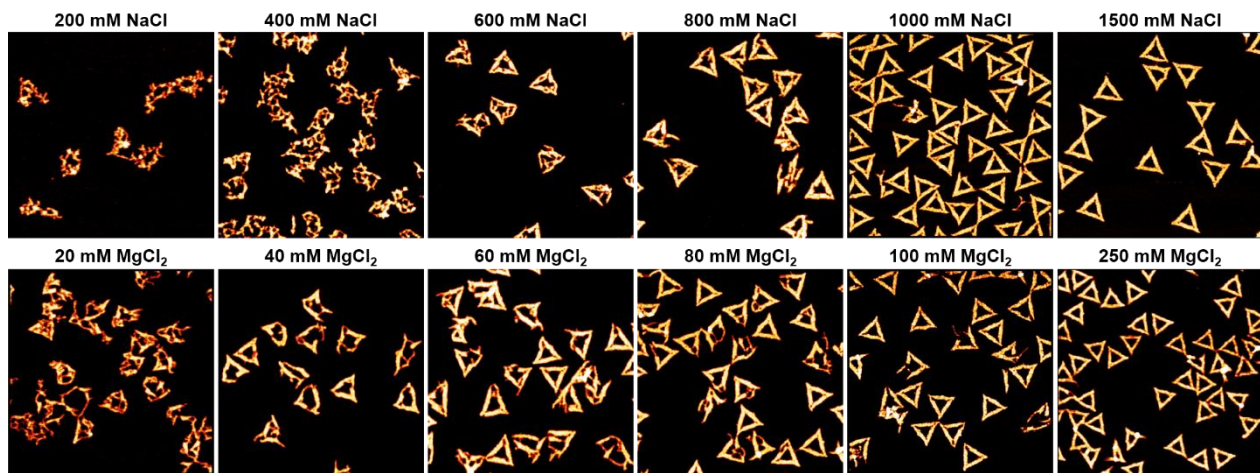
Figure 15. AFM images of DNA origami triangles after 1 h incubation at 42°C in 7 M urea and different concentrations of NaCl (upper row) and MgCl$_2$ (lower row). Images have a size of 1 x 1 µm² and height scales are 2 nm.[222]

As can be seen in figure.16, the fraction of intact DNA origami remains at 0 % until a rather sudden increase is observed at 800 mM NaCl or 60 mM MgCl$_2$, respectively. At first glance, this sudden increase seems contradictory to the expected behavior from the calculated melting temperatures in figure.14. However, the integrity of a DNA origami nanostructure is determined not by its global melting temperature but rather the distribution of melting temperatures of all staple strands, and in particular a few weak staples.[96] Therefore, while the DNA origami appear less and less damaged with increasing NaCl or MgCl$_2$ concentrations, completely intact DNA origami can be observed only at concentrations which result in the vast majority of staple melting temperatures being above 42°C. According to Figure 16, this transition occurs at ~1000 mM NaCl or ~100 mM MgCl$_2$,

respectively. At higher cation concentrations, the fraction of intact DNA origami nanostructures appears to saturate at around 80 %, in agreement with our previous results where we rarely observed 100 % intact DNA origami even at much lower urea concentrations.[96] We attribute this intrinsic damage to the comparatively harsh washing conditions that are required to remove the rather viscous urea solutions from the mica surface.

,
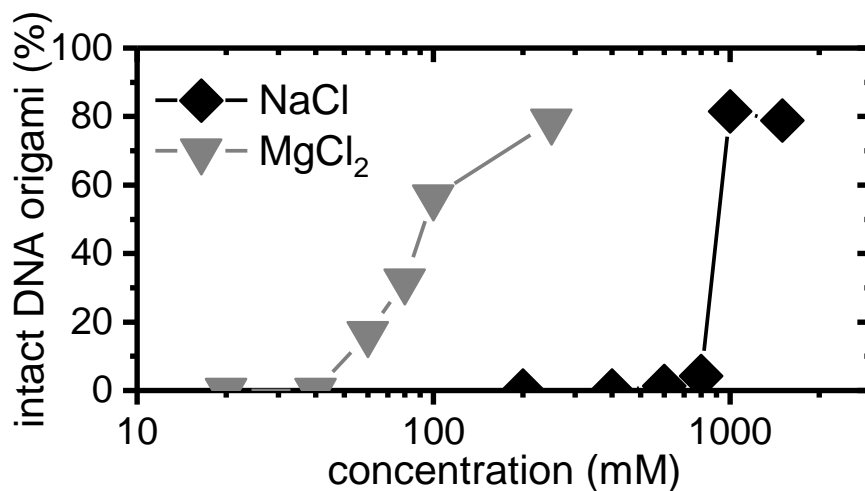
Figure 16. Relative fractions of structurally intact DNA origami triangles after treatment with 7 M urea in the presence of different concentration of NaCl and $MgCl_2$. For each data point, 3 AFM images with $300 - 500$ individual DNA origami triangles were analyzed.[222]

In a second set of experiments, we used 4 M GdmCl instead of 7 M urea and incubated the DNA nanostructures again at different NaCl and $MgCl_2$ concentrations for 1 h at 42°C. Nanostructural analysis using AFM reveals that the DNA origami triangles are comparatively stable in 200 mM NaCl or 20 mM $MgCl_2$ (figure.17), which is again in good agreement with our previous observations.[96] However, an increase of the ionic strength is leading to more and more damaged DNA origami structures, which is in huge contrast to the behavior observed in urea. At 400 mM NaCl or 100 mM $MgCl_2$, the vast majority of DNA origami triangles already appear broken and denatured. This trend further continues until all the triangles are completely denatured at 2000 mM

54

NaCl or 800 mM MgCl$_2$. The destabilizing effect of the cations further depends on the GdmCl concentration. In 2 M GdmCl, where more than 60 % of the DNA origami remain intact at low cation concentrations,[96] we still observe 56 % of intact DNA origami even in the presence of 2000 mM MgCl$_2$. This may indicate that the destabilizing effect of the cations becomes relevant only at temperatures close to the global melting temperature of the DNA origami nanostructures (58°C in 2 M GdmCl *vs.* 48°C in 4 M GdmCl according to our previous results).[96]
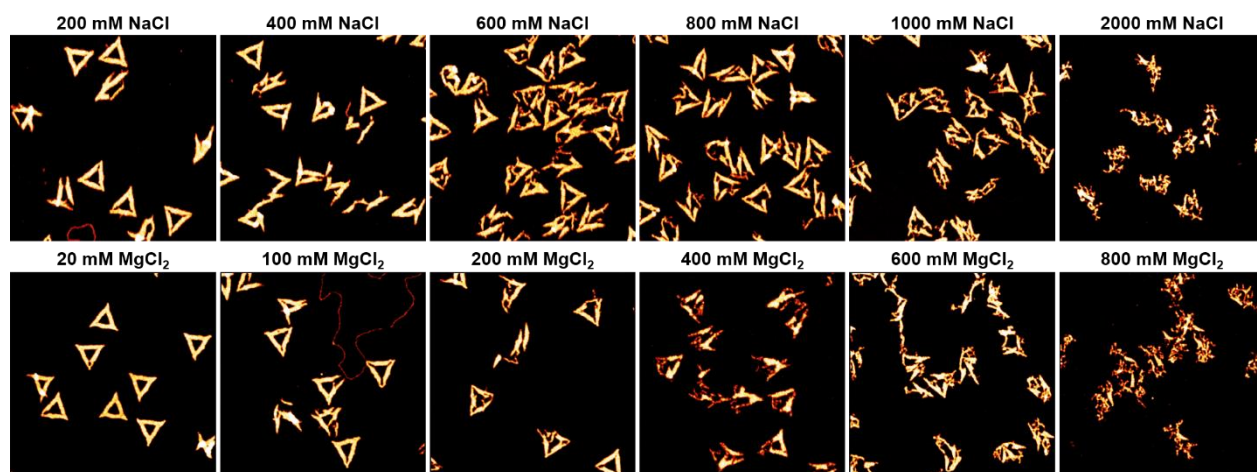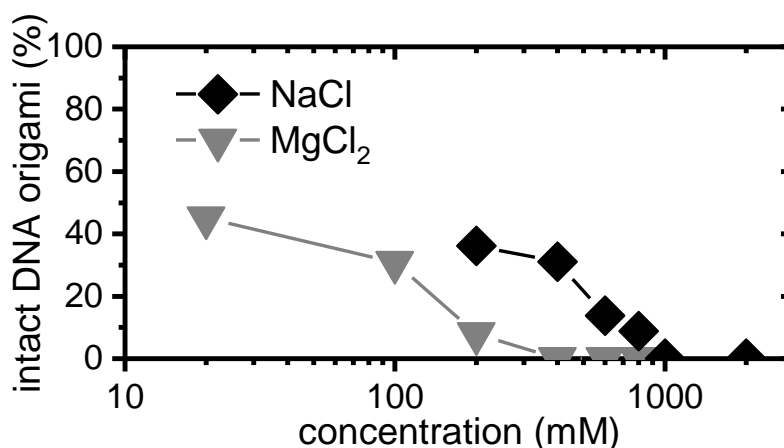

Figure 17. AFM images of DNA origami triangles after 1 h incubation at 42°C in 4 M GdmCl and different concentrations of NaCl (upper row) and MgCl$_2$ (lower row). Images have a size of 1 x 1 μm² and height scales are 2 nm.[222]

These inverse dependencies of DNA origami stabilization *vs.* denaturation by urea and GdmCl on ionic strength are indicative of fundamentally different mechanisms of action. This is reflected also in the structural differences of the denatured DNA origami nanostructures. While denatured DNA origami have a molten appearance in urea (figure.15), they appear rather shredded in GdmCl (figure.17). The statistical analyses further reveal differences in the efficiencies of the two ions to stabilize and destabilize the DNA origami, respectively (see figures.16 and Fig.18). In order to achieve a similar degree of DNA origami stabilization in urea, about ten-fold excess of NaCl over

55

MgCl$_2$ is required (figure 16), in agreement with the calculations shown in Fig.14. However, as can be seen in Fig.18, the destabilizing effects of both ion species in the presence of GdmCl are more similar. In particular, 36 % of intact DNA origami are observed at 200 mM NaCl and 31 % at 100 mM MgCl$_2$. Similarly, 100 % denaturation in 4 M GdmCl happens at 1000 mM NaCl or 400 mM MgCl$_2$. This mere two-fold higher denaturation efficacy of Mg^{2+} indicates that it is not the ionic species that affects DNA origami denaturation by GdmCl but rather ionic strength.

In aqueous solution, GdmCl dissolves into Gdm$^+$ and Cl$^-$. Although its interaction with biomolecules is still far from understood, Gdm$^+$ has been shown to form contacts not only with polar and negatively charged groups, but also hydrophobic and even positively charged molecular species.[218,219] Consequently, Gdm$^+$ can mask any charged surface available on a biomolecule and reduce stabilizing inter- or intramolecular electrostatic interactions.[216] Due to the extraordinarily high density of negative charges in DNA origami nanostructures, it appears likely that Gdm$^+$

Figure 18. Relative fractions of structurally intact DNA origami triangles after treatment with 4 M GdmCl in the presence of different concentration of NaCl and MgCl$_2$. For each data point, 3 AFM images with 300 – 500 individual DNA origami triangles were analyzed.[222]

cations interact with the appears likely that Gdm$^+$ cations interact with the negatively charged phosphates in the DNA backbone, thereby reducing the destabilizing electrostatic repulsion between neighboring helices. In contrast, urea is a neutral molecule that does not participate in electrostatic interactions and denatures DNA via the aromatic nucleobases.[191,213,214] This explains the higher stability of the DNA origami nanostructures in GdmCl at low cation concentrations, whereas much higher cation concentrations are required to achieve a similar stability in urea. This electrostatic stabilization will most likely depend on DNA origami superstructure. Lattice-based three-dimensional DNA origami nanostructures[223,224] for instance have a dense packing of helices and thus a high density of negative charges in their interior. Therefore, these structures may require higher cation concentrations for efficient stabilization in urea. On the other hand, they may withstand higher GdmCl concentrations by more efficient trapping of the Gdm$^+$ ions between the negatively charged helices. In contrast, wireframe-based or gridiron-like DNA origami nanostructures[225–227] with long and well-separated stretches of single helices or thin helix bundles will have lower charge densities than the two-dimensional DNA origami triangles investigated here. Therefore, we expect that these structures can be efficiently stabilized in urea already at lower cation concentrations, while stronger denaturation by Gdm$^+$ may occur.

The counterintuitive denaturation at increased ionic strength in the presence of Gdm$^+$ may result from a salting-out effect. Werner et al. recently observed a 30 % surface enrichment of Gdm$^+$ in a 2 M GdmCl solution after addition of 2 M NaCl.[228] This observation was explained by a salting-out of Gdm$^+$ towards the hydrophobic water–vapor interface by the strongly hydrated Na$^+$ ions. In our experiments, the base stacks of the double-stranded DNA represent similar hydrophobic interfaces. Increasing Na$^+$ or Mg^{2+} concentrations would therefore not only displace Gdm$^+$ cations from the backbone phosphates, but also drive them toward the stacking bases. This might lead to destabilizing forces, for instance by a disruption of the stacking interactions and introduction of

57

hydration water, which would consequently lead to a disruption of the B-DNA structure and eventually to DNA melting.

3.4 Conclusion

In conclusion, we have studied the effect of cations on the structural stability and denaturation of DNA origami triangles in urea and GdmCl. In 7 M urea at 42°C, we observe almost complete denaturation of the DNA origami at low ionic strength, which is prevented by an increasing cation concentration. Thereby, Mg^{2+} cations are ten times more effective than monovalent Na^+, which agrees well with general observations of bivalent ion stabilization of DNA.[91,158,220,221] Surprisingly, in 4 M GdmCl, an increased cation concentration promotes denaturation of the DNA origami. This inverse behavior can be explained by a stabilization of the DNA origami at low cation concentration by phosphate–Gdm^+ complexes and a salting-out[228] of Gdm^+ to the hydrophobic base stacks of the DNA origami at increasing cation concentrations. This effect of cation-induced DNA origami denaturation can be potentially exploited in future applications, e.g., in selective denaturation for purification purposes, and should be considered in experimental designs. We anticipate that future experimental and computational studies can elucidate the molecular mechanisms of cation–GdmCl mediated DNA origami nanostructure denaturation.

# 4. Regular Nanoscale Protein Patterns via Directed Adsorption through Self-Assembled DNA Origami Masks

4.1 Introduction

The introduction of the DNA origami technique by Rothemund in 2006 enabled the fabrication of larger DNA tiles with almost arbitrary shapes[46] that could be arranged into more complex lattices either by solution-based[46,57–62] or surface-assisted[63–67] hierarchical self-assembly. A number of the so synthesized DNA lattices have further been used as scaffolds for the assembly of protein arrays.[45,49,63,65] Various techniques for efficient protein immobilization on DNA origami nanostructures have been reported. The most common approach utilizes the specific binding of proteins to DNA-coupled ligands as exemplified by the widely used streptavidin-biotin system.[45,49,63,65,229–231] Alternative attachment strategies rely on different protein tags,[232,233] aptamers,[234,235] antibody-antigen binding,[72,236] and enzymatic ligation.[237,238] In contrast, classic protein patterning strategies typically utilize selective protein adsorption to fabricate highly-ordered, regular protein patterns over large surface areas. At micron and sub-micron scales, this can be achieved by direct printing techniques such as microcontact[239] and inkjet printing,[240] or by lithographic substrate prepatterning, using for instance electron beam,[241] nanoimprint,[242] dip pen,[243] or colloidal lithography.[244]

Recently, a number of works have reported the application of DNA origami nanostructures as masks in molecular lithography. In particular, single DNA origami shapes have been transferred into various oxide[245–247] and metallic materials[79] using DNA-mediated etching and masking,[245,247] chemical vapor deposition,[246] and physical vapor deposition.[79] Surwade et al. furthermore

demonstrated the fabrication of nanopatterned mixed organosilane self-assembled monolayers using single DNA origami as masks.[77]
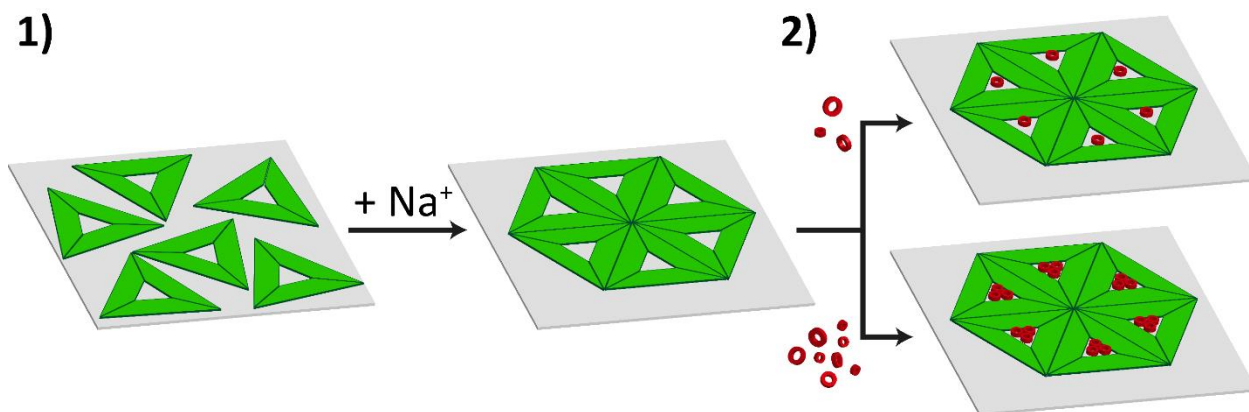
Figure 19. Experimental procedure for the fabrication of regular protein patterns. 1) A densely packed monolayer of triangular DNA origami tiles with internal cavities is assembled on a mica surface at high Na^+ concentration. 2) The monolayer is then used as a hole mask to direct the adsorption of proteins to the exposed surface areas in the holes. By adjusting the protein concentration and buffer conditions, the average number of proteins per hole can be varied from single proteins to densely packed monolayers.[78]

In this work, we utilize ordered monolayers of DNA origami nanostructures on mica surfaces as molecular lithography masks to direct the adsorption of different proteins. To this end, triangular DNA origami tiles with internal cavities are assembled into densely packed hexagonal lattices in the presence of monovalent cations (see Figure 19).[65] Exposure of the masked mica surface to negatively charged proteins in Mg^{2+}-containing buffer then results in the directed adsorption of the proteins onto the remaining exposed surface areas, i.e., the internal cavities in the DNA origami tiles. By adjusting the protein and Mg^{2+} concentrations, the protein coverage of the exposed areas can be tuned from single proteins to densely packed protein monolayers. To demonstrate the versatility of this approach, we fabricate regular nanopatterns of four proteins with different shapes

60

and molecular weights. For the quantitative evaluation of the efficiency of this approach and the optimization of the adsorption conditions, the single strand annealing proteins (SSAPs) Redβ and Sak which exhibit well-defined ring-like shapes are first employed. After successfully patterning these proteins, we turn to the technologically more relevant proteins ferritin and bovine serum albumin (BSA). Since selectivity in adsorption is achieved solely by electrostatic interactions between protein and exposed surface, our approach is however not restricted to proteins but may also enable the large-scale patterning of other charged molecular species or nanoparticles.

4.2 Methods

Assembly of DNA origami hole masks: Triangular DNA origami designed by Rothemund[46] were assembled as described previously [194] from the M13mp18 scaffold (Tilibit) and 208 staple strands (Metabion) by stepwise thermal annealing in 1 x TAE buffer (Calbiochem) containing 10 mM $MgCl_2$ (Sigma-Aldrich) using a thermocycler Primus 25 advanced (PEQLAB). After assembly, the DNA origami triangles were spin filtered using Amicon Ultra filters with 100 kDa MWCO (Millipore) to remove non-hybridized staple strands. DNA origami concentrations were determined using an IMPLEN NanoPhotometer P 330.

The DNA origami samples (20 nM) were incubated in 1 x TAE/Mg^{2+} supplemented with 200 mM NaCl (Sigma-Aldrich) on freshly cleaved mica surfaces for 15 minutes. After incubation, the surfaces were carefully rinsed several times with HPLC-grade water (VWR) and dried in a stream of ultrapure air.

Protein adsorption: For protein adsorption experiments, 10 µL of Redβ (prepared as previously described[248], Sak , horse spleen ferritin (Sigma-Aldrich), BSA (Sigma-Aldrich), thyroglobulin (Sigma-Aldrich) and immunoglobulin G (Sigma-Aldrich) in B1 buffer (200 mM KCl, 20 mM KH_2PO_4, pH 6.0) supplemented with different concentrations of $MgCl_2$ were gently dropped onto

61

the freshly prepared DNA origami masks and incubated for 15 minutes. After incubation, the protein patterned surfaces were rinsed several times with HPLC-grade water and dried with ultrapure air. Table 3 gives the molecular weight, shape, and pI of each of the proteins used for patterning.

protein	MW (kDa)	shape	pI
Redβ	339.9 – 370.8 (30.9 per monomer)	split lock washer-like	5.2
GFP-Redβ	635.8 – 693.6 (57.8 per labeled monomer)	crown-like	5.2 – 6.0
Sak	313.5 (28.5 per monomer)	ring-like	5.2
Ferritin	~ 900	spherical	4.4
BSA	66.5	ellipsoidal	4.7
Thyroglobulin	~ 660	globular	4.5
Immunoglobulin G	~150	Y- shaped	n.a

Table 3. Properties of the proteins used in the patterning experiments

**DNA origami desorption:** After BSA adsorption, the mica surface was rinsed with HPLC-grade water and kept wet. Immediately after rinsing with water, 1 x TAE buffer (without $MgCl_2$) supplemented with 200 mM NaCl was dropped onto the BSA patterned surface and incubated for 30 minutes. The sample surface then was rinsed slowly with HPLC-grade water to remove unbound DNA origami from the mica surface and dried in ultrapure air.

AFM imaging: All AFM images were recorded in air with an Agilent 5100 AFM operated in intermittent contact mode using HQ:NSC18/Al BS cantilevers (MikroMasch). For the statistical evaluation of the number of proteins adsorbed in the holes of the DNA origami mask, between 400 and 745 individual DNA origami tiles have been analyzed for each condition.

4.3 Results and Discussion

4.3.1 Assembly of DNA origami hole masks

Molecular lithography masks have been fabricated from the triangular DNA origami design of Rothemund[46] by surface-assisted, cation-mediated self-assembly according to the protocol of Rafat et al.[65] The DNA origami triangle has an edge length of about 130 nm and features an internal triangular cavity with about 50 nm edge length. Incubation of the DNA origami triangles on freshly cleaved mica surfaces in the presence of 10 mM Mg^{2+} and 200 mM Na^+ results in the formation of an ordered, densely packed DNA origami monolayer with hexagonal symmetry as shown in the AFM image and the corresponding two-dimensional Fourier transform in figure.20. The hexagonal symmetry arises from six triangular DNA origami tiles joining together. Therefore, also the internal triangular cavities display a hexagonal symmetry that in the following will be used to direct the adsorption of proteins and fabricate ordered protein patterns. Since the adsorption of the negatively charged DNA origami on the negatively charged mica surface is mediated by a bridging layer of Mg^{2+} ions, stability of the self-assembled DNA origami mask requires moderate Mg^{2+} concentrations also during protein adsorption. Therefore, only proteins with pI values in the acidic pH range have been used in the following patterning experiments to ensure efficient adsorption on the exposed, Mg^{2+}-presenting surface areas.
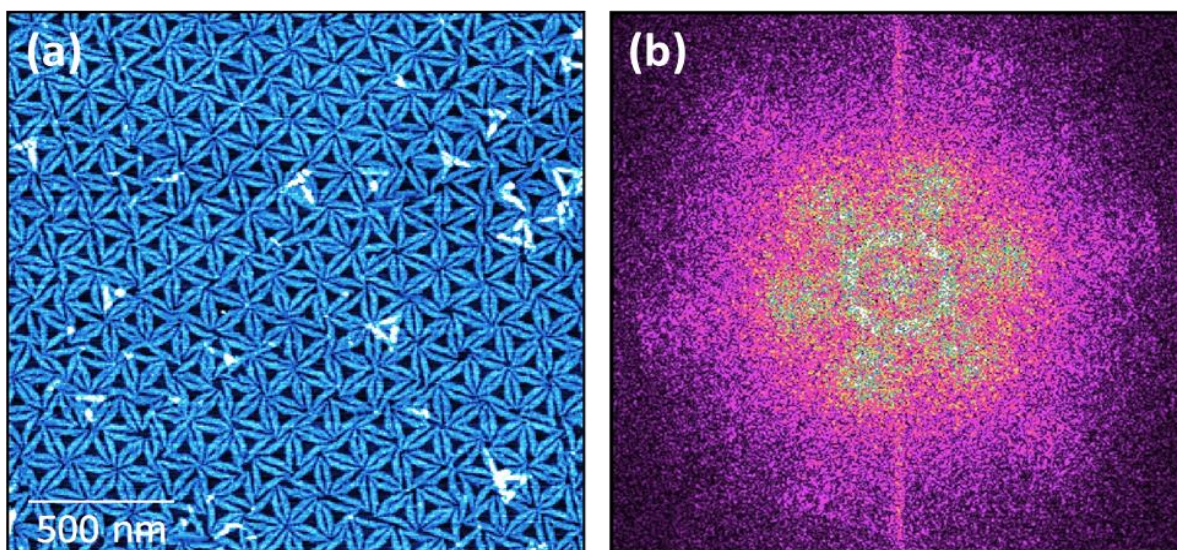
Figure 20. AFM image (a) and corresponding two-dimensional fast Fourier transform (b) of the molecular lithography mask on a mica surface.[78]

4.3.2 Redβ patterning

In order to study directed adsorption through the self-assembled DNA origami masks in detail, we have first used the SSAP Redβ (pI ~ 5.2). This protein forms large complexes composed of 11 to 12 monomers with a distinct split lock washer-like shape and an average outer diameter and height of about 17 nm and 3.5 nm, respectively, that can be easily identified in AFM images.[249] Protein adsorption on charged surfaces is influenced by several different factors, most importantly charge of the sorbent surface, protein concentration, and ionic strength of the buffer solution.[250] Therefore, we have investigated the adsorption of Redβ on the masked mica surface in B1 buffer (200 mM KCl, 20 mM KH_2PO_4, pH 6.0) containing different Redβ (1 − 3 µM) and Mg^{2+} (10 − 30 mM) concentrations.

Figure. 21 shows AFM images of the Redβ patterns obtained at the different protein and Mg^{2+} concentrations. A clear influence of both concentrations on the Redβ coverage of the exposed
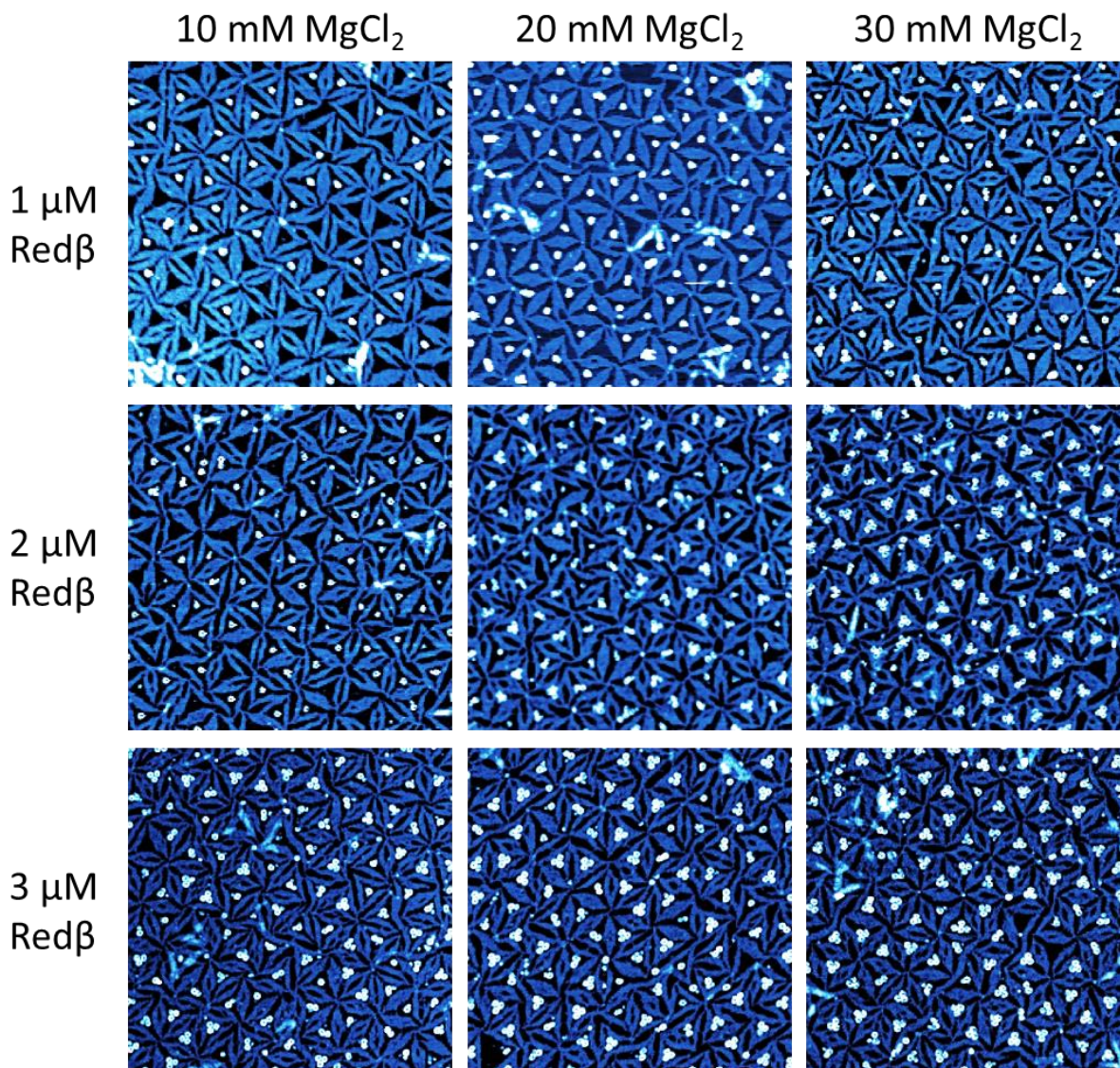
Figure 21. AFM images of Redβ adsorbed in the holes of ordered DNA origami masks obtained after 15 min incubation in B1 buffer at different Redβ and Mg^{2+} concentrations. All images have a size of 1.1 x 1.1 μm^2. Height scales are 3 nm.[78]

surface areas is visible. In general, increasing both the Redβ and Mg^{2+} concentrations seems to result in larger coverage of the exposed mica surface. At the highest concentrations, *i.e.*, 3 μM Redβ and 30 mM Mg^{2+}, the majority of the triangular holes in the DNA origami mask are occupied

by three proteins. Considering the comparatively large outer diameter of Redβ of about 17 nm,[249] this corresponds to the maximum number of proteins the holes can accommodate.

In order to analyze the effects of the protein and Mg^{2+} concentrations on the directed Redβ adsorption through the DNA origami mask more quantitatively, we have performed a statistical evaluation of the number of proteins per hole for each experimental condition (see figure.22). At a low Redβ and Mg^{2+} concentration of 1 µM and 10 mM, respectively, about 52 % of the holes are filled with one protein while the rest of them remains empty. Interestingly, increasing the incubation time from 15 to 60 min does not result in significant changes in these numbers (see figure.23). Increasing the Mg^{2+} concentration to 20 mM, on the other hand, results in almost 90 % of the holes being occupied by a single protein. At an even higher concentration of 30 mM, a broader distribution is obtained with about 13 % of the holes being completely filled with three proteins and 16 % with two, while the yield of holes filled with a single Redβ protein decreased to about 60 %. The observation that the surface coverage of the exposed mica areas is increasing with increasing Mg^{2+} concentration can be explained by the electrostatic interaction between the negatively charged mica surface and the negatively charged protein, which crucially depends on the number of available Mg^{2+} bridges at the surface.

In contrast to the Redβ concentration of 1 µM, however, a 2 µM concentration results already at 10 mM Mg^{2+} in about 68 % of the holes being filled with one protein (figure.22). At this protein concentration, the maximum of the distribution shifts immediately from one protein per hole to three proteins per hole upon increasing the Mg^{2+} concentration to 20 mM. At 30 mM Mg^{2+}, about 62 % of the holes are occupied by three proteins and about 24 % by two. At 3 µM Redβ and 10 mM Mg^{2+}, we observe almost identical yields for holes filled with one and three proteins while the
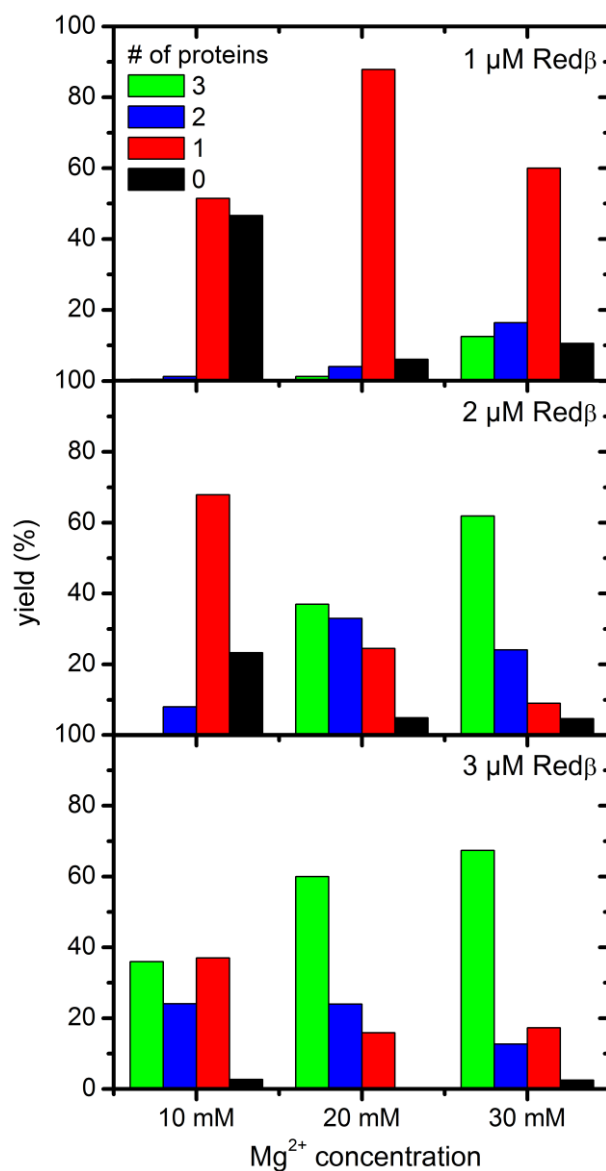
Figure 22. Statistical evaluation of the number of Redβ proteins per hole in dependence of the Redβ and Mg^{2+} concentrations.[78]

yield for two proteins is slightly lower. With increasing Mg^{2+} concentration, the yield of completely filled holes increases further until a value of almost 70 % is obtained at 30 mM. Interestingly, this value is rather close to the one obtained at the same Mg^{2+} concentration and 2 μM Redβ. Further increase of the Redβ concentration to 5 μM does not result in a significant increase of this yield either (see figure.23). This might indicate that complete surface coverage of all exposed areas in

67

the mask is hindered by parasitic adsorption of impurities and residual staple strands that have not been removed during protein and DNA origami purification, respectively.
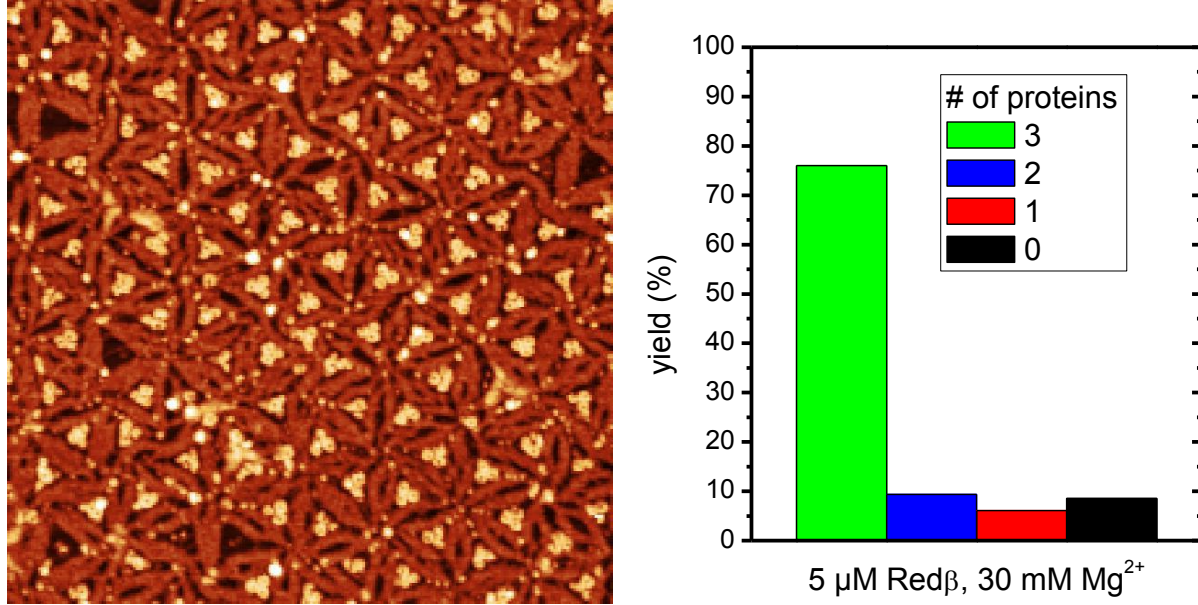
Figure 23: AFM image and corresponding statistical evaluation of the number of Redβ proteins per hole for 5 µM Redβ and 30 mM Mg^{2+}. The image size 1.1 x 1.1 µm².

Closer inspection of the AFM image shown in figure.23 indeed reveals the presence of small particles in the holes and between individual DNA origami triangles. These particles probably represent Redβ monomers at different stages of denaturation that block potential adsorption sites. Nevertheless, above results demonstrate that adjusting the protein and Mg^{2+} concentrations can control the number of proteins per hole. Under optimized conditions, even patterns consisting almost exclusively of single proteins can be realized. By applying other purification techniques, also full protein coverage in the holes of the DNA origami mask might be achieved.

4.3.3 Time-dependent adsorption of Redβ inside DNA origami mask

1µM Redβ protein/ 15 minutes   **1µM Redβ protein/ 60 minutes**
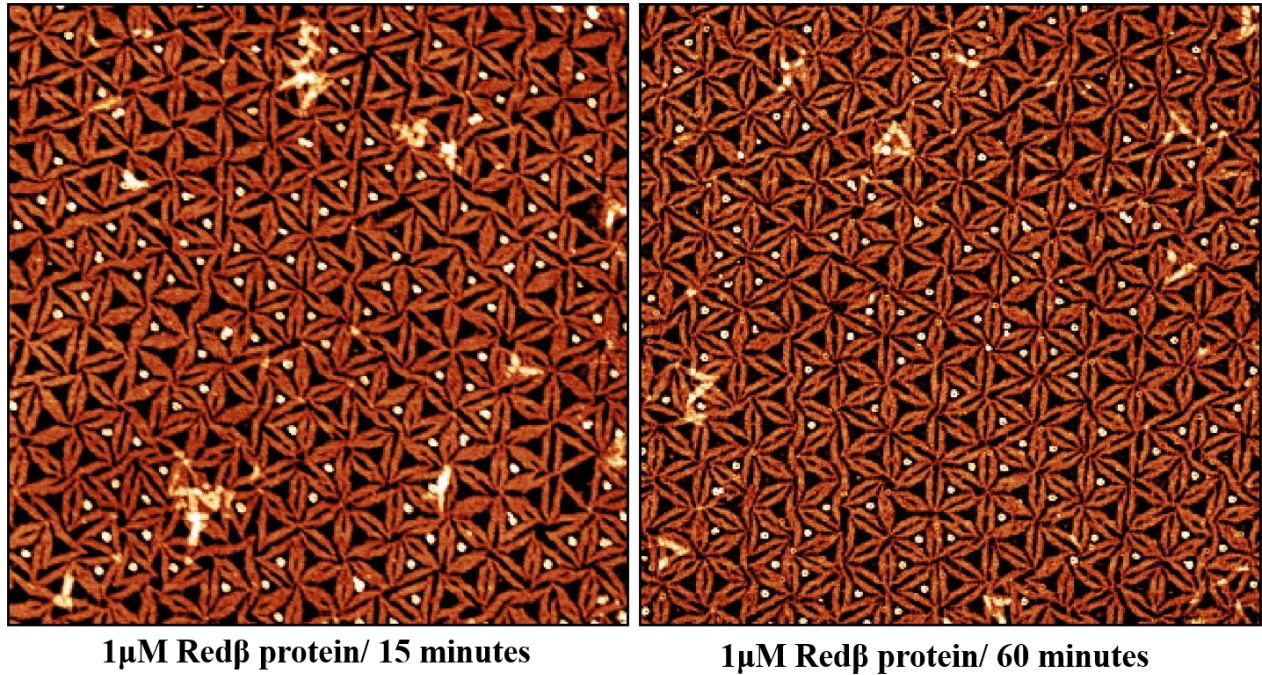
Figure 24. AFM images of Redβ adsorbed in the holes of ordered DNA origami masks obtained after 15 min and 60 minutes incubation in the B1 buffer at 1µM Redβ concentration. All images have a size of 2 x 2 µm^2. Height scales are 3 nm.[78]

One crucial fact that we have encountered during the protein adsorption experiments is increased adsorption time did not increase the number of single proteins inside masks. Figure.24 shows the AFM images of 15 minutes and 60 minutes incubation time-dependent protein adsorption. The statistical analysis (figure.25) shows that the number of single proteins occupied DNA origami did not change after 60 minutes.
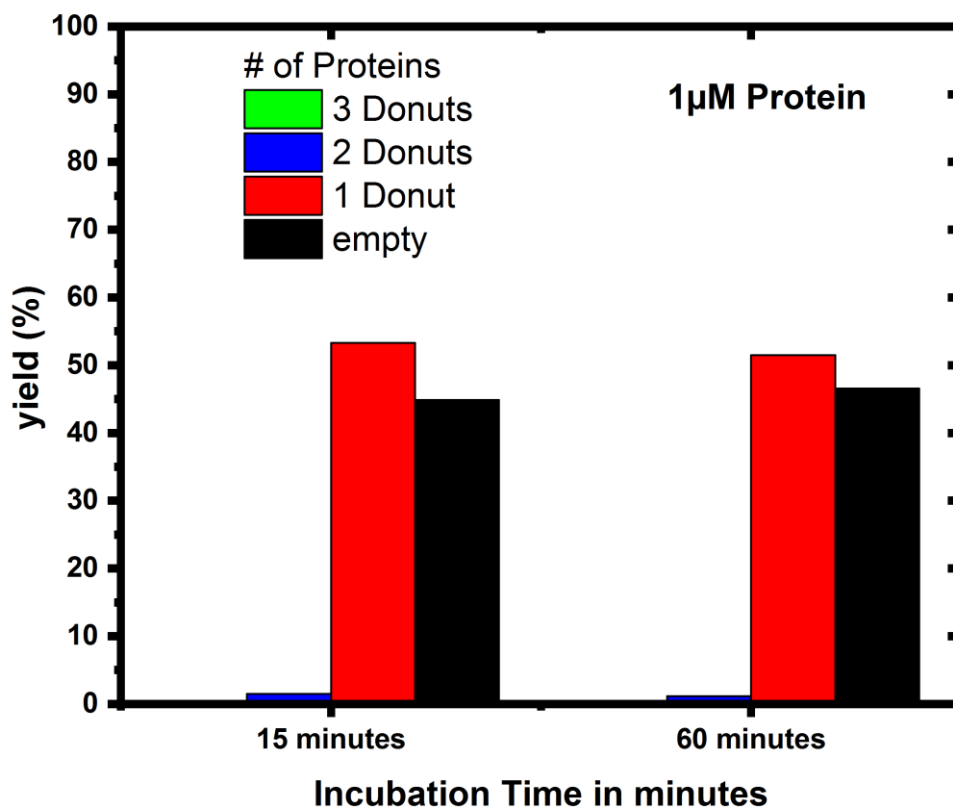
Figure 25. Statistical evaluation of the number of Redβ proteins per hole in dependence of the time

4.3.4 Irregular adsorption of Redβ inside DNA origami mask

During the SAM preparation, sometimes inefficient washing and reduced incubation time, may exhibit several number of defects such as shrinking of DNA origami. Due to the gaps between origami and one or more unfilled places in SAM, proteins tend to adsorb on the available free spaces especially at high ionic strength and eventually end up in irregular adsorption. Figure.26 shows the nonspecific adsorption of Redβ protein inside the gaps and unfilled triangular spaces. Redβ proteins are adsorbed in triangular shape, linear shape and irregular shapes in the DNA origami SAM.
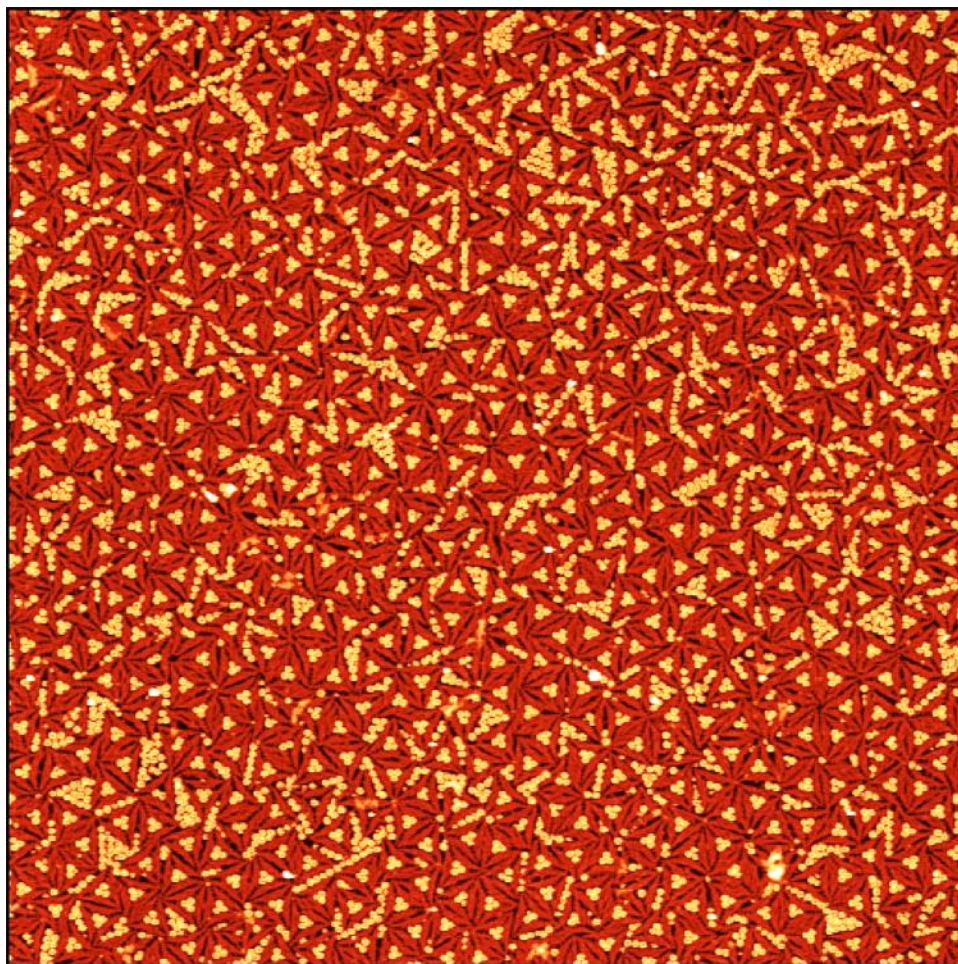
Figure 26. AFM images of 3μM Redβ with 30mM MgCl$_2$ nonspecifically adsorbed inside the defects of DNA origami mask, obtained after 15 min incubation in B1 buffer. Image has a size of 3 x 3 μm^2. Height scale is 6 nm.

4.3.5 GFP-Redβ patterning

Above experiments show that the relative dimensions of the holes and the proteins play a significant role in this patterning approach. For the triangular DNA origami used in mask assembly, each hole can accommodate a maximum of three Redβ proteins. A reduction in the hole size or an increase in the size of the protein will result in a lower number of immobilized proteins per hole. In order to study the effect of protein size, we have drastically increased the outer diameter of the Redβ

complex by labelling each Redβ monomer with a green fluorescent protein (GFP). The resulting GFP-Redβ complex has a crown-like shape with a maximum outer diameter of about 40 nm. Consequently, each hole in the DNA origami mask can accommodate only a single protein complex. This is demonstrated in figure 5 for two selected adsorption conditions. At 1 µM GFP-Redβ and 20 mM Mg^{2+} (figure.27a), about 75 % of the holes are filled with a single protein, while the remaining holes are empty. The distribution is thus quite similar to the one obtained for unlabeled Redβ under the same conditions which also has a clear maximum at a single protein per hole (see figure 22).
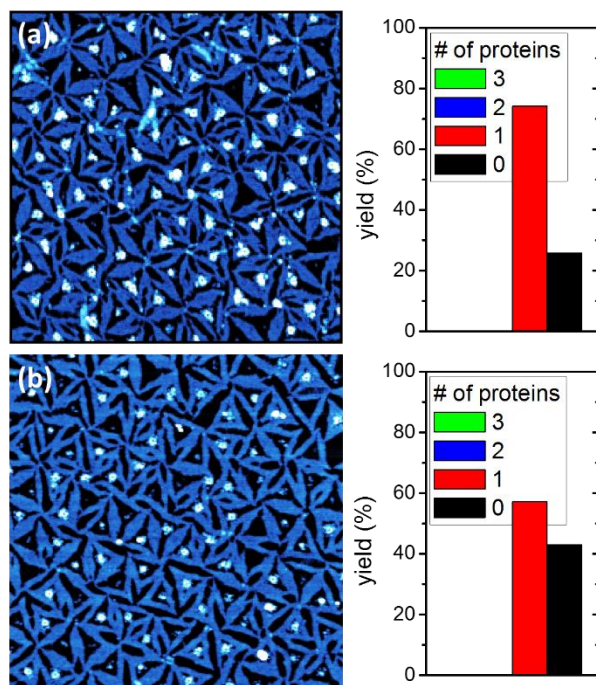
Figure 27. AFM images and corresponding statistical evaluation of the number of GFP-Redβ proteins per hole for 1 µM GFP-Redβ and 20 mM Mg^{2+} (a) and 3 µM GFP-Redβ and 10 mM Mg^{2+} (b), respectively. All images have a size of 1.1 x 1.1 µm². Height scales are 4 nm.[78]

However, the total yield is significantly decreased for GFP-Redβ compared to unlabeled Redβ which indicates weaker interaction with the mica surface. This weaker interaction may result from the higher pI of GFP (6.0) compared to Redβ (5.2). At a Redβ and Mg^{2+} concentration of 3 µM and 10 mM, the distribution in Fig.22 shows a similar yield of around 30 % for one, two, and three proteins per hole. For GFP-Redβ under the same conditions (Fig.27b), however, almost 60 % of the holes are filled with a single protein while the remaining holes are empty. This shows that even at high protein concentrations, only single GFP-Redβ complexes can adsorb in the holes of the DNA origami mask. The reduced yield compared to the low-protein, high-Mg^{2+} condition in Fig.27a can again be attributed to the weaker interaction of GFP-Redβ with the mica surface which obviously requires higher Mg^{2+} concentrations for efficient immobilization. However, higher Mg^{2+} concentrations at 3 µM GFP-Redβ were found to result in strong adsorption of residual unbound GFP which therefore hinders unambiguous identification of the GFP-Redβ complexes.

4.3.6 Sak patterning

In order to further investigate the influence of protein size, we have used another SSAP, *i.e.*, the Rad52 homolog Sak. Sak is a ring-shaped protein with similar pI and molecular weight as Redβ (see Materials and Methods) but a slightly smaller diameter of about 14 nm so that a larger number of proteins can be accommodated in the holes of the DNA origami mask.[251] In spite of all similarities, however, Sak is found to have a stronger affinity for the mica surface than Redβ. Therefore, Sak patterning experiments were carried out under the same conditions as above but at lower protein concentrations.

Figure.28 shows AFM images of Sak adsorbed through DNA origami masks at a protein and Mg^{2+} concentration ranging from 0.1 to 0.5 µM and 10 to 30 mM, respectively. Similar effects of both concentrations on the coverage of the exposed surface areas as in above Redβ experiments are

observed. At 0.1 µM Sak and 10 mM Mg^{2+}, more than half of the holes remain empty while a single protein occupies the other holes predominantly. With increasing Mg^{2+} concentration, a moderate increase in the yield of occupied holes is observed. At 20 and 30 mM Mg^{2+}, also a small population of holes filled with two proteins appears. At 0.3 µM Sak, both the fraction of occupied holes and the number of proteins per hole are increased.
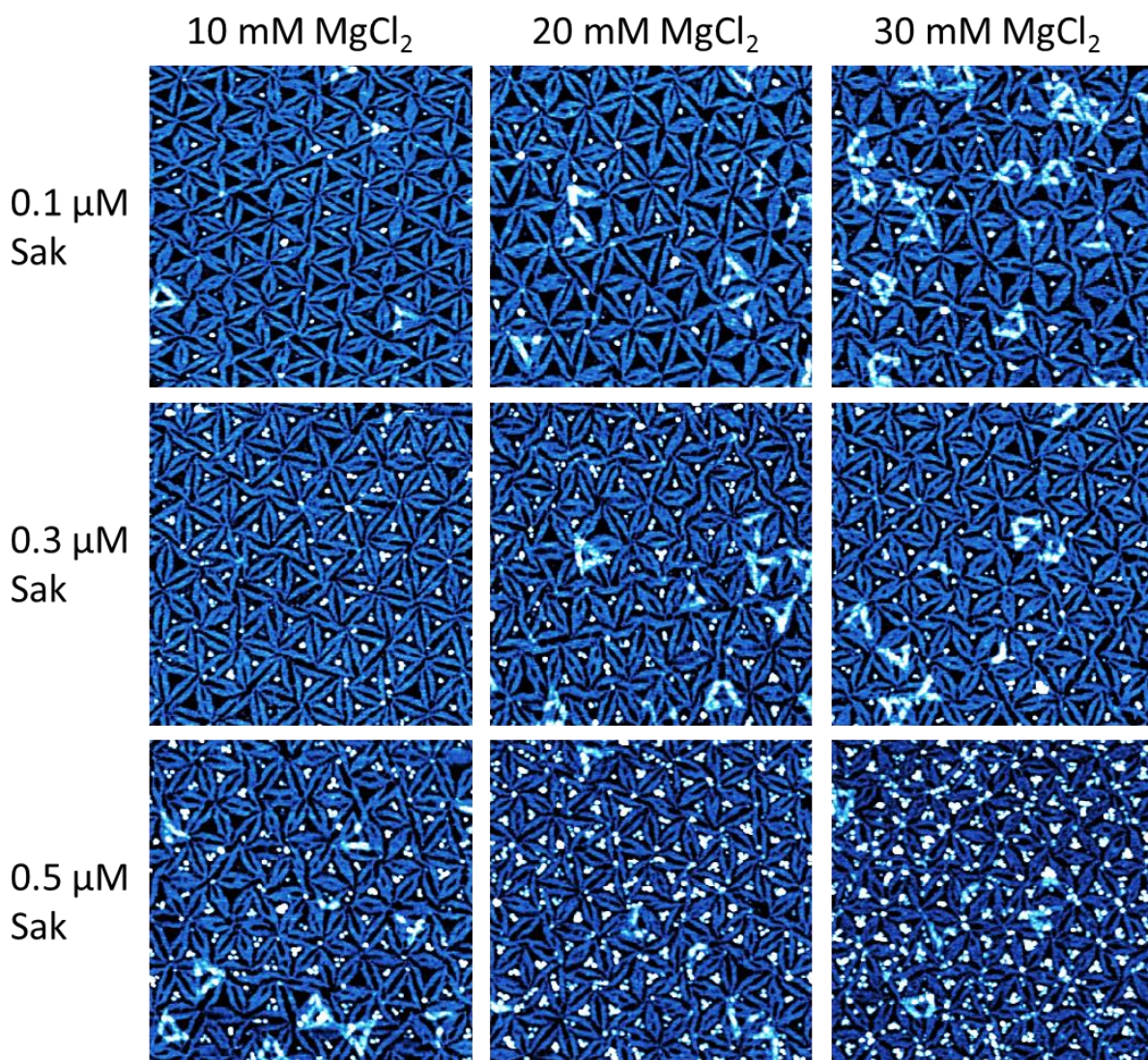
Figure 28. AFM images of Sak adsorbed in the holes of ordered DNA origami masks obtained after 15 min incubation in B1 buffer at different Sak and Mg^{2+} concentrations. All images have a size of 1.1 x 1.1 µm². Height scales are 3 nm.[78]

Further increase of both the protein and the Mg^{2+} concentration results in increased surface coverage, until at 0.5 µM protein with 30 mM Mg^{2+} concentration, the holes are almost completely filled by a dense Sak monolayer. Due to the small size of Sak, however, quantifying the surface coverage in the holes of the mask is rather difficult under these conditions. Furthermore, at the highest protein and Mg^{2+} concentrations, Sak is also occasionally found to adsorb in the narrow gaps between neighboring DNA origami tiles. Therefore, these gaps between individual DNA origami tiles, as well as small secondary cavities within the tiles such as the seams between the three trapezoids that form the triangular DNA origami,[46] may limit the applicability of this approach for proteins with small dimensions and a high affinity for the mica surface.

4.3.7 Ferritin patterning

After patterning SSAPs with well-defined shape, we turned to ferritin as a technologically more relevant protein. Ferritin is an universal iron-storage protein consisting of a cage-like shell with 12 nm diameter that encloses an 8 nm ferrihydrite core.[252] When empty, the protein shell has a molecular weight of 450 kDa. When filled, the shell can accommodate up to 4500 iron atoms, thereby increasing the weight of the protein up to 900 kDa. Ferritin has been widely studied with regard to the magnetic[253] and catalytic[254] properties of its iron-containing nanoparticle core. Motivated by these potential applications, also the controlled deposition of ferritin has received tremendous attention.[255–259]

For the selective adsorption of ferritin through the DNA origami mask, we have used the same buffer conditions as in the previous experiments. However, contrary to the behavior of Redβ and Sak, ferritin showed a tendency to aggregate in the presence of Mg^{2+}. Therefore, the AFM images shown in figure.29 were obtained only for the lowest Mg^{2+} concentration of 10 mM which resulted only in moderate aggregation. Although the heterogeneous shape and size of the adsorbed

75

aggregates prevents the identification of single proteins, an increase in protein coverage of the exposed mica surface with ferritin concentration is evident. At a ferritin concentration of 25 ng/µL, all holes in the DNA origami mask are almost completely occupied by proteins. Due to the further increased aggregation of ferritin at higher concentrations, however, the mica surface had to be washed intensively with water after adsorption to remove loosely adsorbed protein aggregates. This intense washing procedure also had an effect on the DNA origami mask. As can be seen in figure.29, the individual DNA origami tiles composing the mask are slightly shrunk in size, probably due to removal of Mg^{2+} ions from the surface. Although this shrinking results in rather large gaps between neighboring DNA origami tiles, the gaps are not filled with ferritin which further supports above interpretation that the gaps form during washing after successful protein adsorption. Therefore, despite protein aggregation and post-adsorption damage of the mask, acceptable patterning efficiency is obtained.
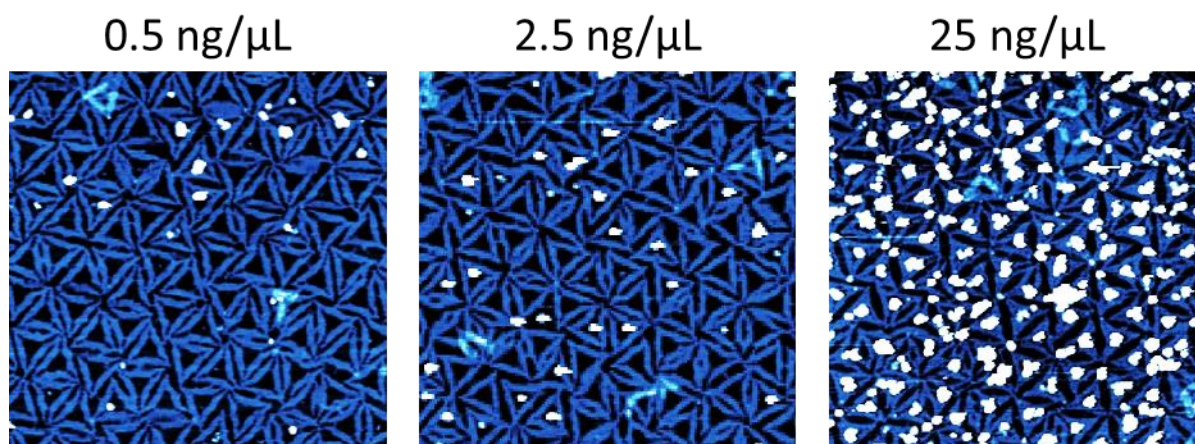

Figure 29. AFM images of ferritin adsorbed in the holes of ordered DNA origami masks obtained after 15 min incubation in B1 buffer at 10 mM Mg^{2+} and different ferritin concentrations. All images have a size of 1.1 x 1.1 µm^2. Height scales are 4.5 nm.[78]

4.3.8 BSA patterning

As a second technologically relevant example, patterning of BSA has been attempted using DNA origami masks. BSA is a soft globular protein of ellipsoidal shape with dimensions of 4 nm x 4 nm x 14 nm and a molecular weight of 66.5 kDa.[260] It has been widely used for surface passivation[261–263] to prevent nonspecific protein and cell interactions which is an important issue in biotechnology,[264] biosensing,[265] and medicine.[266] BSA is well-known for its ability to rapidly adsorb and strongly adhere to a huge variety of surfaces and nanoparticles with different physicochemical properties.[267–271] At high concentrations, BSA changes its conformation rapidly upon adsorption and tends to aggregate and partially unfold or denature completely, thereby maximizing the interaction with the surface.[272] Although the adsorption of BSA on mica surfaces is well-studied, the structure of the adsorbate films is still under discussion.[273–275]

In view of the strong tendency of BSA to denature upon adsorption, we have aimed at completely filling the holes of the DNA origami mask by using high BSA and Mg^{2+} concentrations of 5 µM and 30 mM, respectively. Figure.30a shows an AFM image of BSA adsorbed in the holes of the DNA origami mask. Although its strong denaturation makes the identification of adsorbed BSA quite difficult, most of the holes in the mask actually appear filled with a thin film and some small, differently sized particles. Since it was already shown that BSA adsorbed on hydrophilic surfaces is almost impossible to remove even at high NaCl concentrations,[267] we attempted to selectively desorb the DNA origami mask by incubation in buffer containing 200 mM Na^+ but no Mg^{2+} in order to visualize the BSA pattern on the surface. Under these conditions, the Na^+ ions will replace all the remaining Mg^{2+} ions at the mica surface which then becomes electrically neutral. In the absence of an attractive electrostatic force, the DNA origami will then desorb from the surface.[276] Figures.30b,c shows AFM images of the BSA pattern on the mica surface after desorption of the

DNA origami mask. Although the BSA-covered patches have a rather irregular shape due to the strong denaturation of the protein, they do reflect the hexagonal symmetry of the DNA origami mask, which is particularly apparent in the zoomed image in figure 30c. This proofs that also soft proteins that denature during adsorption can be efficiently patterned using DNA origami masks. In addition, the restored unoccupied areas of the mica surface that were originally covered by the mask may now serve as adsorption sites for another protein species. In this way, hierarchical protein patterns may be realized.
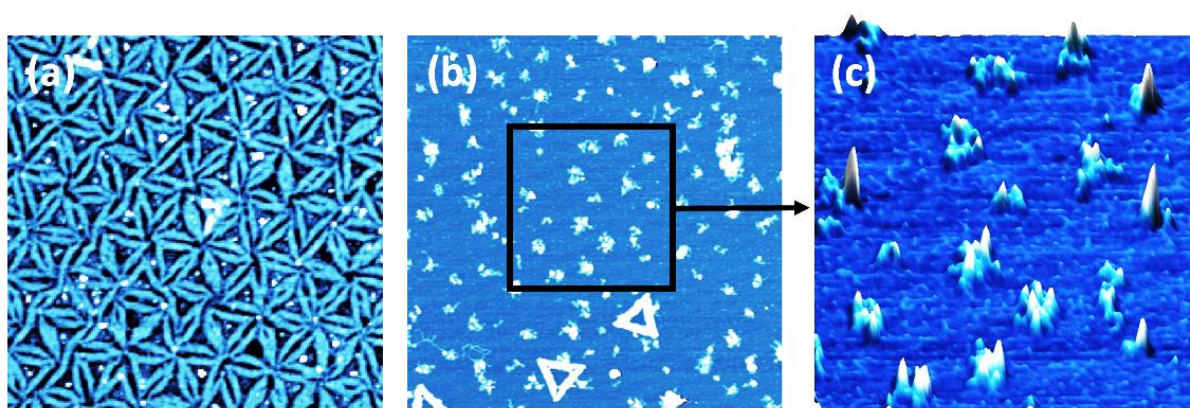
Figure 30. AFM images of (a) BSA adsorbed in the holes of an ordered DNA origami mask obtained after 15 min incubation in B1 buffer with 30 mM Mg^{2+} and 5 µM BSA, (b) BSA pattern on mica after desorption of the DNA origami mask by incubation in TAE buffer with 200 mM NaCl for 30 minutes, and (c) 3D zoom of the region marked in (b). Images have a size of 1.1 x 1.1 µm^2 (a,b) and 0.5 x 0.5 µm² (c), respectively. Height scales are 2 nm.[78]

4.3.9 Desorption experiments with Redβ protein

The desorption of DNA origami from mica surface can be achieved as low as from 50mM NaCl in 1XTAE buffer without Mg^{2+}. In figure.31a. the Redβ patterned DNA origami SAM was incubated with 50 mM NaCl and very few origami were desorbed from the mica, leaving Redβ proteins on surface. since the Redβ protein itself has the same possible adsorption mechanism as DNA origami

78

through divalent cation bridges, at 200mM NaCl concentration, several Redβ proteins were desorbed along with the DNA origami. In very few places, the patterned proteins were visible (see figure.31b). When proteins are very close in contact with DNA origami, the desorption of DNA origami may induce the removal of proteins, especially during washing. We have examined different incubation times and concentrations of NaCl, but the controlled desorption of DNA origami alone could not be achieved.
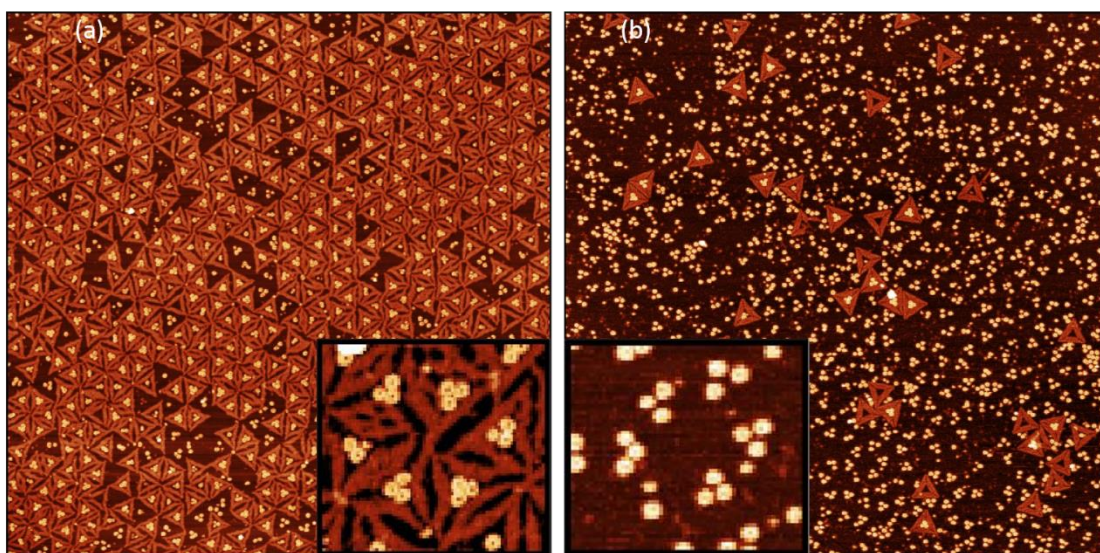
Figure 31. AFM images of (a) DNA origami desorbed from mica surface after Redβ protein patterning, using 50mM NaCl in 1XTAE without Mg^{2+} (b) DNA origami desorbed from mica surface after the Redβ protein patterning, using 200mM NaCl in 1XTAE without Mg. Images have a size of 3 x 3 μm^2 (a,b) and 0.3 x 0.3 μm^2 (insets), respectively. Height scales are 5 nm.

4.3.10 Factors limiting protein adsorption specificity

The selection of protein for patterning experiments is important not only in the context of pI value but also in aggregation, irregular shape, poor adsorption and nonspecific binding with DNA origami. Figure.32.a shows the adsorption of thyroglobulin protein inside the DNA origami SAM.

Due to the poor adsorption on mica, irregular shape and aggregation, the patterning was not successful. On the other hand, immunoglobulin G protein (IgG) (figure.32b) adsorbs on mica as well as on DNA origami structures. Such proteins should be avoided in the case of protein patterning experiments with DNA origami nanostructures.
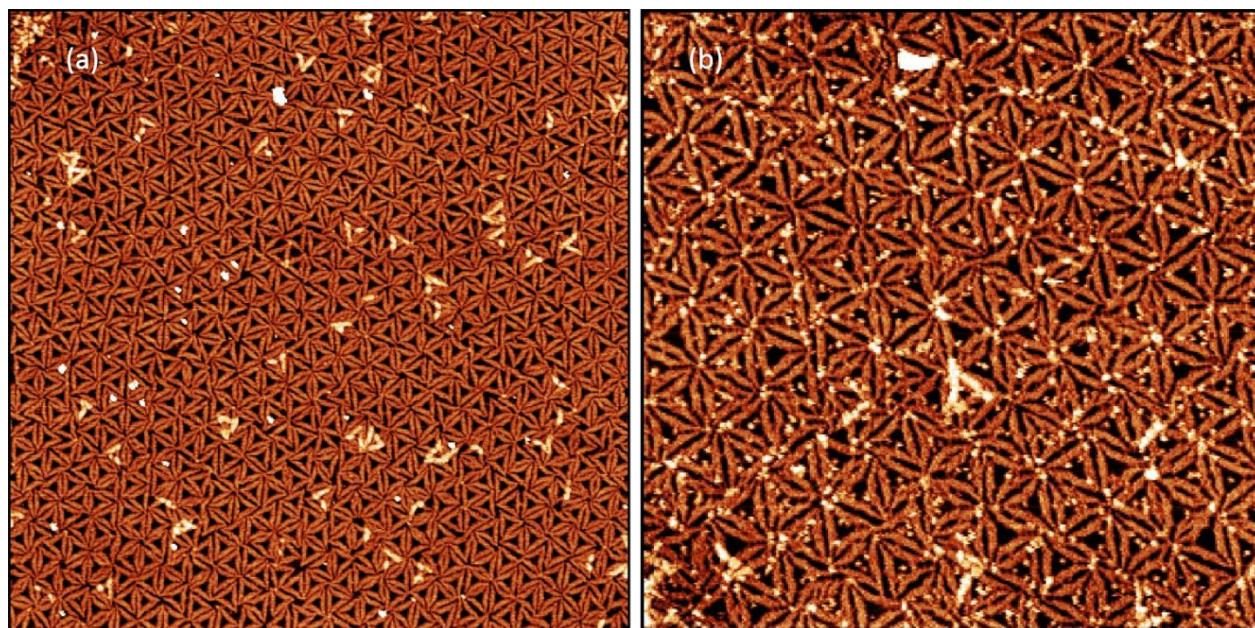
Figure 32. AFM images of (a) thyroglobulin (b) Immunoglobulin G adsorbed inside DNA origami masks obtained after 15 min incubation in B1 buffer at 10 mM Mg^{2+} . Image (a) has a size of 3.5 x 3.5 μm^2. Height scale is 3 nm. Image (b) has a size of 1.5 x 1.5 μm^2. Height scale is 3 nm.

4.4 Conclusion

In summary, we have demonstrated the fabrication of regular nanoscale protein patterns on mica surfaces using ordered DNA origami monolayers as molecular lithography masks. Spatially selective protein immobilization was achieved by directed adsorption of the proteins through internal cavities in the DNA origami tiles. Four different proteins were used in our experiments to investigate the versatility of the approach. Regular patterns consisting of different numbers of the SSAPs Redβ and Sak immobilized in the holes of the DNA origami mask were fabricated. For the

larger Redβ, the number of proteins per hole could be controlled from single proteins to densely packed monolayers consisting of three proteins by adjusting the protein and Mg^{2+} concentrations. A similar trend was also observed for the slightly smaller protein Sak, but with a larger number of proteins accommodated in the holes. In addition, due to its reduced size, Sak was able to adsorb in the gaps between neighboring DNA origami tiles at high protein concentrations. Increasing the size of the Redβ complex by labelling with GFP resulted in holes filled only with single protein complexes even at high protein concentrations.

The iron-storage protein ferritin was found rather prone to aggregation at the comparatively high Mg^{2+} concentrations required to maintain the stability of the DNA origami mask during protein adsorption. Nevertheless, ferritin patterns consisting of fully covered surface patches were achieved a 10 mM Mg^{2+} and high protein concentration. Also the soft protein BSA could be preferentially adsorbed in and completely fill the holes of the DNA origami mask to form a regular pattern. Due to the strong denaturation of BSA upon adsorption, however, visualization of the adsorbed proteins in the holes was rather difficult. Therefore, the DNA origami mask was desorbed from the mica surface by exposure to Mg^{2+}-free buffer containing 200 mM NaCl. Mask desorption revealed a pattern of BSA patches exhibiting a clear hexagonal symmetry on the mica surface.

This approach represents a simple and efficient means to fabricate regular protein patterns over large surface areas. Since directed adsorption is achieved solely by electrostatic interactions between the proteins and the mica surface, any negatively charged protein that is compatible with the Mg^{2+} concentrations required to ensure stability of the DNA origami mask can be patterned in this way. In addition, the approach can also be extended to other negatively charged entities including inorganic nanoparticles. By using different DNA origami tiles for mask assembly, the geometric structure of the resulting patterns can be designed and controlled. In particular, the size

81

and shape of the protein patches can be adjusted via the internal cavities of the DNA origami tiles, while the symmetry and periodicity of the pattern are governed by the tiles' outer shape and dimensions. By employing masks based on multilayer DNA origami designs,[247] also the thickness of the mask can be adjusted in order to improve lateral confinement, *e.g.*, when working with larger proteins. Furthermore, the possibility to desorb the mask after successful patterning may at least for some proteins such as BSA enable the fabrication of hierarchical patterns composed of different species.

5. On the Adsorption of DNA Origami Nanostructures in Nanohole Arrays

5.1 Introduction

Many of the technological applications of DNA origami nanostructures critically rely on their precise placement on a substrate surface. Consequently, a large number of previous studies have evaluated various methods for the controlled immobilization and/or alignment of DNA origami nanostructures on different application-relevant materials.[66,173–178,277–280] Most of the approaches reported in literature have employed top-down photo- or electron beam lithography to fabricate prepatterned substrate surfaces to direct DNA origami adsorption to chemically different micro- or nanoscale patches.[173–178,277] Other studies have utilized receding menisci for the manipulation of already adsorbed DNA origami,[66,278] or self-organized nanopatterns for the selective adsorption of DNA origami nanostructures.[279,280]

In this chapter, we investigate directed DNA origami adsorption in nanohole arrays patterned into thin Au films on Si wafers by nanosphere lithography (NSL). NSL is a technique based on self-organization that enables the large-area patterning of surfaces with nanoscale features.[281] To this end, (mono-) layers of nanospheres are assembled on solid surfaces by convective self-assembly of colloidal nanospheres from suspensions.[282,283] Evaporation fluxes of the liquid medium of the suspension lead to an increased nanosphere concentration at a forming triple phase boundary between the liquid suspension, the solid substrate, and the surrounding gas phase. Along this triple phase boundary, capillary forces act on the nanospheres and draw them together, resulting in hexagonally close-packed nanosphere arrangements. In NSL, such nanosphere layers are used as a

shadow mask in a subsequent deposition step[281] during which material is deposited onto the nanospheres as well as onto the substrate through the mask openings in the nanosphere layer.

NSL enables the fabrication of various and often surprisingly complex patterns over large surface areas,[244,284] which are for instance frequently used in protein patterning.[244,285,286] The here employed NSL-fabricated nanohole arrays in Au films, on the other hand, exhibit unique plasmonic properties[287,288] and are thus used extensively in biosensing and on-chip bioanalysis.[289,290] Immobilizing DNA origami nanostructures inside individual nanoholes may enable the introduction of single molecular capture sites and thereby provide additional benefits with regard to target specificity and sensitivity.[291] While the specific adsorption of single biotin-carrying DNA origami nanostructures inside similar nanoholes has already been demonstrated using neutravidin-modified substrate surfaces,[291] we here study non-specific DNA origami adsorption to the exposed SiO_2 surface at the bottom of the nanoholes in the Au film. In particular, we investigate the effect of buffer conditions on directed DNA origami adsorption in the nanohole arrays. We find that the strength of the adsorption buffer has a surprisingly strong influence and that the low surface mobility of once-adsorbed DNA origami is negatively affecting adsorption selectivity and positioning accuracy even under optimized conditions.

5.2 Methods

DNA origami assembly: DNA origami triangles[46] were synthesized as described previously,[78] using the M13mp18 scaffold (Tilibit) and 208 staple strands (Metabion). Assembly was performed in 1x TAE (Carl Roth) with 10 mM $MgCl_2$ (Sigma-Aldrich) by stepwise thermal annealing in a thermocycler Primus 25 advanced (PEQLAB). Excess staples were removed after assembly by spin filtering using 100 kDa MWCO filters (Amicon Ultra, Millipore). After filtering, the DNA origami concentration was measured by UV/Vis absorption with an Implen Nanophotometer P330.

DNA origami adsorption: The nanohole array substrates were first cleaned with ethanol and water. A mild oxygen plasma cleaning (Zepto, Diener electronic) was carried out for 1 min with 50 % power before DNA origami adsorption. For DNA origami adsorption, 1x TAE and 2.5x TAE stock solutions were prepared with 10 mM $MgCl_2$. For the higher $MgCl_2$ concentration of 50 mM, working solutions were freshly prepared by adding the required volume from a 1 M $MgCl_2$ stock solution. The DNA origami sample was then diluted in the respective buffer solutions to the desired concentrations. The nanohole array substrate was placed on a stage inside a humidity chamber to avoid evaporation and 100 µl of the resulting sample solution were slowly dropped on the surface. After incubation, the sample was carefully washed with 4 ml of HPLC-grade water (VWR) and dried in a stream of ultrapure air.

Self-assembled monolayer (SAM) fabrication: Plasma-cleaned nanohole array samples were immersed in 1 mM 1-octadecanethiol (ODT, Sigma-Aldrich) in ethanol for 24 h to form hydrophobic SAMs on the surfaces of the Au films. Immediately before the adsorption experiments, the SAM-coated nanohole arrays were rinsed with ethanol and dried in a stream of ultrapure air. The ODT SAMs formed under these conditions exhibit high packing densities and render the Au surface fully hydrophobic.[292]

Atomic force microscopy (AFM): The samples were imaged in intermittent contact mode in air using an Agilent 5100 AFM and HQ: NSC18/Al BS cantilevers (MikroMasch). A minimum 600 individual nanoholes were analyzed for each condition.

5.3 Results and discussion

The experimental strategy is schematically summarized in figure 33. Ordered nanohole arrays are fabricated by NSL (The samples were prepared and analysed in SEM by Ms. Katharina Brassat).

To this end, hexagonally close-packed monolayers of PS nanospheres are assembled on a Si wafer by convective self-assembly using the doctor blade technique.[293] The assembled PS nanospheres are then shrunk by exposure to an O_2/Ar plasma to create an array of well-separated yet hexagonally ordered nanospheres. The shrunk nanospheres then act as a shadow mask for physical vapor deposition. A 10 nm thin Au film is deposited onto the sample, *i.e.*, the shrunk nanospheres and bare SiO_2 in the gaps between the nanospheres. Lift-off of the nanospheres by dissolution uncovers the final surface pattern, *i.e.*, a thin Au film exhibiting hexagonally arranged nanoholes which expose the untreated SiO_2 surface at their bottoms. These confined SiO_2 surfaces at the bottoms of the nanoholes are then used to direct DNA origami adsorption.
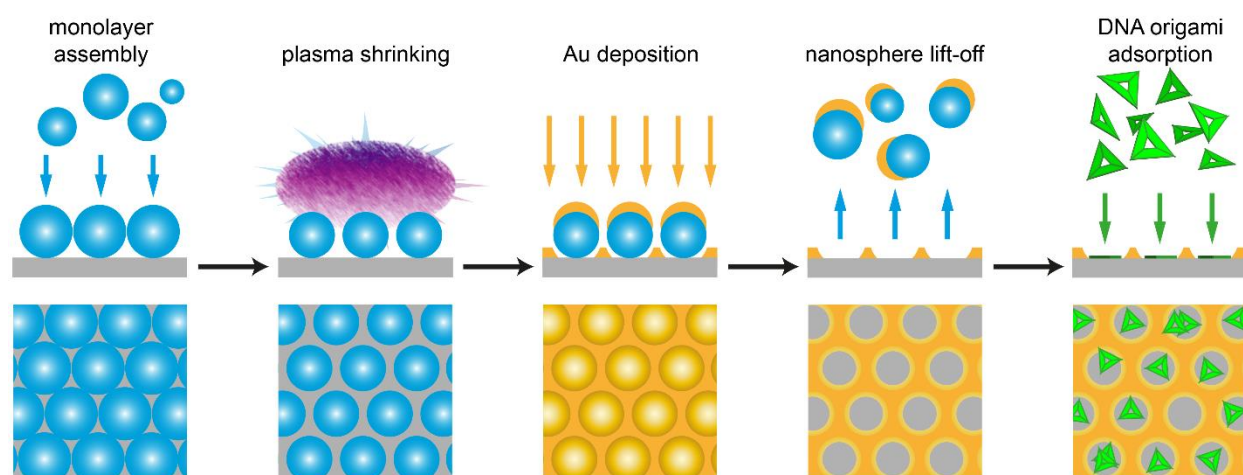
Figure 33. Experimental strategy: A hexagonally ordered pattern of nanoholes in a thin Au film on a Si wafer is fabricated by NSL and used to direct the adsorption of DNA origami nanostructures.

The fabricated nanohole patterns are characterized in figure 34. Analysis of the SEM images reveals a diameter of the nanoholes of 160 ± 16 nm and a nanohole density of 2.6×10^9 cm^{-2}. In addition, 95 % of the nanoholes show perfect sixfold coordination. The nanohole diameter of 160 nm allows for adsorbing single triangular DNA origami nanostructures with an edge length of about

120 nm. Due to the lateral confinement of the exposed SiO_2 area by the surrounding Au film, adsorption of more than one DNA origami triangle per nanohole should be restricted. However, since adsorption of the negatively charged DNA origami nanostructures to the negatively charged SiO_2 patches requires divalent cations such as Mg^{2+} in order to form salt bridges between DNA and surface, adsorption efficiency and especially selectivity can be expected to critically depend on buffer conditions.[278] Therefore, we have first evaluated the role of Mg^{2+} concentration and buffer strength on DNA origami adsorption in the nanoholes.
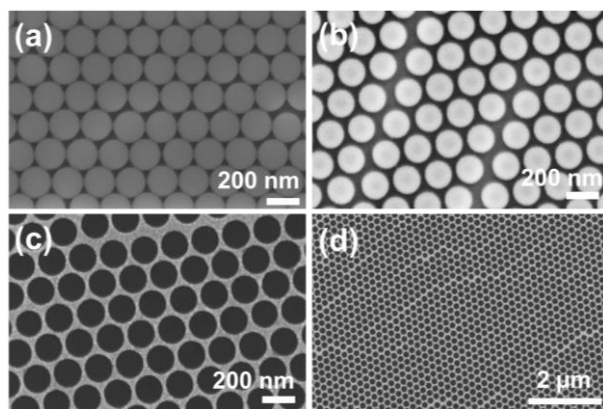
Figure 34. SEM images of the assembled nanosphere monolayers before (a) and after (b) plasma shrinking, and the resulting nanohole array (c,d). (The samples were prepared and analysed in SEM by Ms. Katharina Brassat)

Figure 35 shows AFM images of nanohole patterns after adsorption of 1 nM DNA origami triangles in different buffers for 1 h. Obviously, both buffer strength and Mg^{2+} concentration have significant effects on DNA origami adsorption. Increasing the $MgCl_2$ concentration from 10 to 50 mM in 1x TAE results in significantly higher DNA origami coverage of the exposed SiO_2 areas. In particular, as the statistical analysis in figure 35 reveals, the fraction of empty nanoholes decreases from more than 70 % at 10 mM $MgCl_2$ to only about 10 % in 50 mM $MgCl_2$. Surprisingly, however, this results in only about 40 % of the nanoholes being occupied by a single DNA origami, whereas half

of the nanoholes exhibit two or even three DNA origami nanostructures. Considering the nominal edge length of the triangles and the average diameter of the nanoholes of 120 nm and 160 nm, respectively, this double and triple occupation can result from two or three DNA origami triangles stacking on top of each other or from only partial adsorption of one or more DNA origami triangles inside the nanoholes with a part of the triangle crossing the boundary to the Au film. Upon closer inspection, examples of both mechanisms can be observed on one sample surface (see figure 36). However, a statistical analysis reveals that partial adsorption of DNA origami nanostructures accounts for about 63 % of multiply-occupied nanoholes, while only 37 % show vertical stacking. Note that partial adsorption is also frequently observed for singly-occupied nanoholes (see figure 36c).
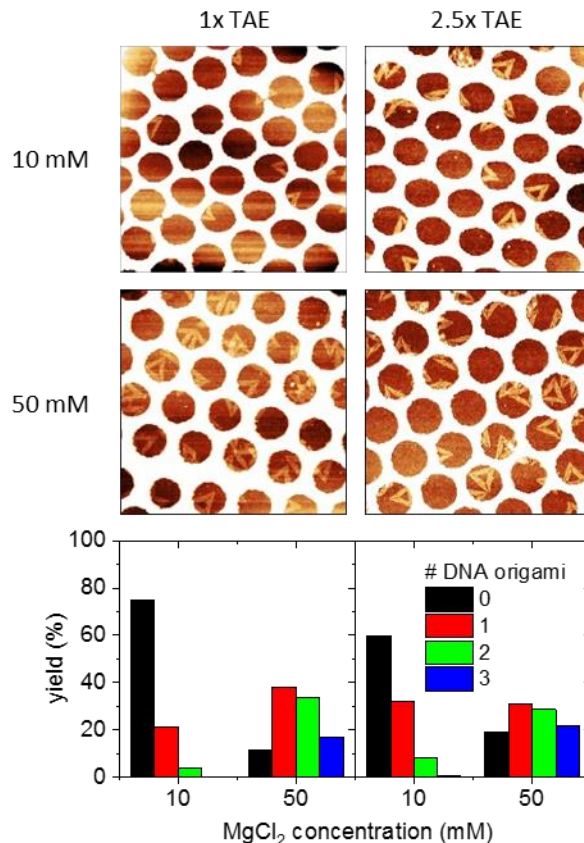
Figure 35. AFM images (1 x 1 µm², height scales 3 nm) and corresponding statistical analyses of DNA origami triangles adsorbed in the nanohole arrays for two buffer strengths and two $MgCl_2$ concentrations. The DNA origami concentration was 1 nM and the incubation time 1 h.

Increasing the buffer strength to 2.5x TAE at a constant $MgCl_2$ concentration of 10 mM results also in a decrease in the fraction of empty nanoholes and a moderate increase in the fraction of nanoholes occupied by a single DNA origami triangle to about 30 % (see figure 35). However, the fraction of higher occupancies remains below 10 %. Increasing the $MgCl_2$ concentration to 50 mM again leads to a further decrease in the fraction of empty nanoholes which, however, is not as strong as in the case of 1x TAE. This is also reflected in the fraction of singly-occupied nanoholes which remains rather constant. These results demonstrate the non-trivial interplay of buffer strength and Mg^{2+} concentration in DNA origami adsorption to SiO_2 surfaces.

89
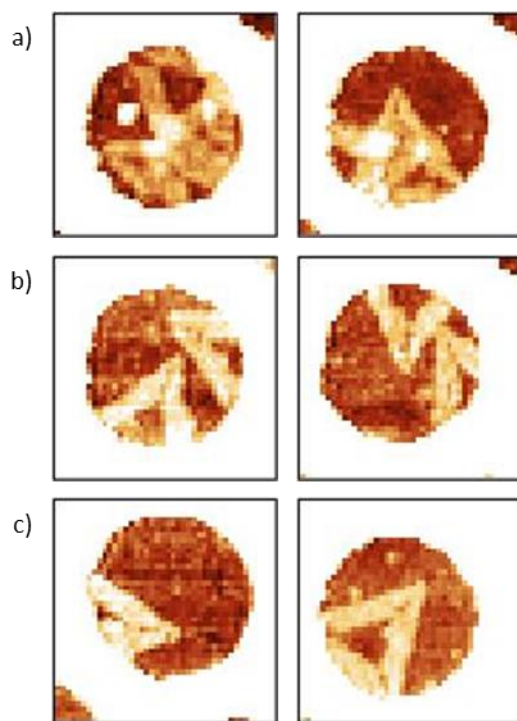
Figure 36. Zoomed AFM images of (a) multiple DNA origami nanostructures adsorbed in single nanoholes via vertical stacking, (b) multiple DNA origami nanostructures adsorbed in single nanoholes via partial adsorption, and (c) single DNA origami nanostructures adsorbed in single nanoholes via partial adsorption. The DNA origami concentration was 1 nM in 1x TAE with 50 mM $MgCl_2$ and the incubation time 1 h.

Due to the large fraction of nanoholes occupied by more than a single DNA origami triangle at high $MgCl_2$ concentrations, we have used the lower concentration of 10 mM in all the following experiments.Apart from the buffer conditions, also the DNA origami concentration will affect surface coverage and thereby the occupation of the nanoholes. The effect of DNA origami concentration is therefore evaluated in figure 37, again for two different buffer strengths.

Figure 37. AFM images (1 x 1 µm², height scales 3 nm) and corresponding statistical analyses of DNA origami triangles adsorbed in the nanohole arrays for two buffer strengths and three DNA origami concentrations. The $MgCl_2$ concentration was 10 mM and the incubation time 1 h.

Surprisingly, increasing the DNA origami concentration in 1x TAE from 1 nM to 5 nM does not result in any noticeable increase in the DNA origami density. In particular, the fraction of empty and singly-occupied nanoholes remains at about 70 % and about 25 %, respectively, independent of DNA origami concentration.

91

At the higher buffer strength of 2.5x, the situation is notably different. As can be seen in figure 37, increasing the DNA origami concentration from 1 nM to 2.5 nM results in a drastic decrease in the fraction of empty nanoholes from about 60 % to roughly 10 %. At the same time, the fraction of nanoholes occupied by a single DNA origami triangle increases from about 30 % to about 50 %. At this DNA origami concentration, the second most dominant population is represented by nanoholes occupied by two DNA origami triangles at about 35 %. Further increase of the DNA origami concentration to 5 nM, however, does not result in any significant changes in these numbers.

Finally, we set out to investigate the influence of adsorption time on directed DNA origami adsorption in the nanohole arrays. For these experiments, we used a DNA origami concentration of 1 nM since this concentration resulted in the lowest fractions of multiply-occupied nanoholes (see figure 37). Increasing the incubation time in 1x TAE was found to result in a continuous decrease in the fraction of empty nanoholes from about 75 % after 1 h incubation to about 40 % after 12 h (see figure 38). At the same time, the fraction of singly-occupied nanoholes increases from about 20 % to about 50 %. Remarkably, the fraction of multiply-occupied nanoholes increases only marginally with incubation time and reaches roughly 10 % after 12 h incubation.

A higher buffer strength of 2.5x again results in drastically different behavior. Here, the fraction of singly-occupied nanoholes is steadily decreasing with incubation time, from about 30 % after 1 h to almost 0 % already after 3 h of incubation. This decrease is due to a dramatic increase in the number of adsorbed DNA origami triangles per nanohole. After 3 h of incubation, the majority of nanoholes, *i.e.* around 50 %, is occupied already by three DNA origami, while more than 40 % of the nanoholes exhibit two DNA origami triangles. After 12 h of incubation, virtually all the nanoholes are occupied by three or more DNA origami nanostructures.
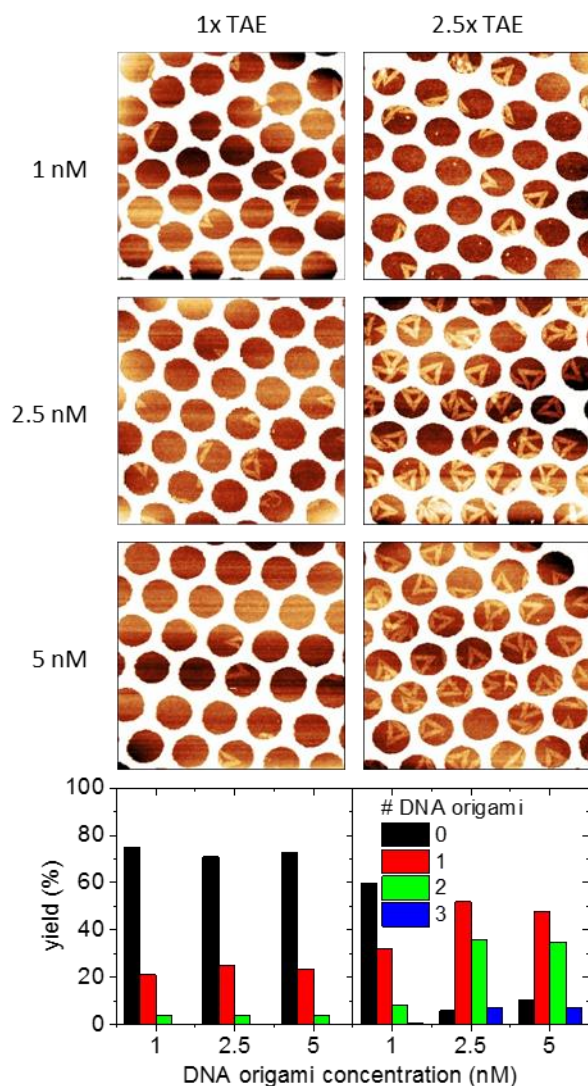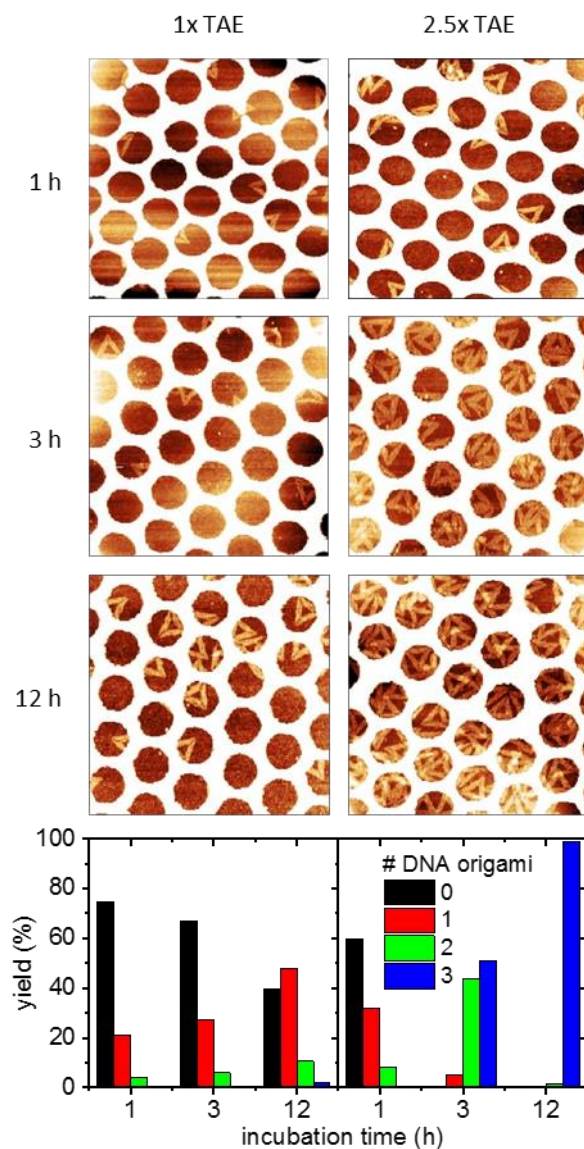
Figure 38. AFM images (1 x 1 µm², height scales 3 nm) and corresponding statistical analyses of DNA origami triangles adsorbed in the nanohole arrays for two buffer strengths and three incubation times. The $MgCl_2$ and DNA origami concentration was 10 mM and 1 nM, respectively.

Above results demonstrate the tremendous importance of buffer strength in DNA origami adsorption in general and directed adsorption in particular. Based on these data, it appears possible to obtain a yield of nanoholes occupied by only a single DNA origami triangle of more than 50 %, in particular by using low buffer strengths, low Mg^{2+} concentrations, low DNA origami

93

concentrations, and long incubation times of 12 h and more. However, even under optimized conditions, many of the single DNA origami nanostructures are not fully located inside the nanoholes but rather cross the boundary to the Au film (see figures 36 and 38). This partial DNA origami adsorption may result from two different effects. A low lateral mobility of the adsorbed DNA origami nanostructures at the SiO_2 surface may prevent them from maximizing their contact area with the oxide surface and thereby centering themselves in the nanoholes. On the other hand, DNA origami may also adsorb to the surface of the Au film which – in the case of comparable affinities for Au and SiO_2 – would result in random adsorption instead of directed immobilization.

If low surface mobility of the DNA origami on the SiO_2 surface was responsible for the observed partial adsorption in the nanoholes, reducing the diameter of the nanoholes to approach the size of the DNA origami should lead to higher yields of singly-occupied nanoholes due to stronger lateral confinement. Therefore, we have prolonged the plasma exposure of the assembled nanospheres to reduce their diameter to 120 nm so that it matches the size of the DNA origami triangles. Figure 39 shows AFM images and the corresponding statistical analyses of DNA origami triangles adsorbed in the nanohole patterns with 120 nm and 160 nm diameter. The adsorption conditions were chosen to result in a yield of about 50 % singly-occupied and 50 % multiply-occupied nanoholes with 160 nm diameter (see figure 37). As can be seen in figure 39, very similar distributions are obtained for both nanohole sizes. The only visible difference between the statistical distributions in figure 39 is the apparent lack of 120 nm nanoholes occupied by three DNA origami triangles. This may be a result of the small nanohole size that even in the case of partial adsorption cannot accommodate more than two DNA origami triangles. On the other hand, the small nanohole diameter makes identification of individual DNA origami nanostructures inside the nanoholes quite difficult and may thus introduce a bias in the statistical evaluation shown in figure 39. Nevertheless, these results demonstrate that partial adsorption of DNA origami

94

nanostructures cannot be significantly reduced by using smaller nanohole diameters, thus hinting at the relevance of parasitic adsorption to the surface of the Au film.
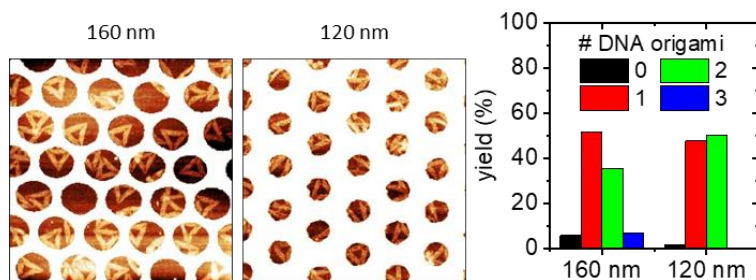

Figure 39. AFM images (1 x 1 µm², height scales 3 nm) and corresponding statistical analyses of DNA origami triangles adsorbed in a 160 nm nanohole array and a 120 nm nanohole array. Adsorption conditions were 2.5 nM DNA origami in 2.5x TAE with 10 mM $MgCl_2$ for 1 h.

Due to the comparatively high roughness of the deposited Au film, we are unable to identify DNA origami triangles crossing from the bottoms of the nanoholes to the surface of the Au film in the AFM images. On smoother template-stripped Au surfaces, however, a significant amount of adsorbed DNA origami can be detected even at low DNA origami and MgCl2 concentrations (see figure 40). This indeed suggests that parasitic DNA origami adsorption to the surface of the Au film interferes with directing adsorption to the bottoms of the nanoholes. Therefore, we have modified the surfaces of the Au films of 160 nm nanohole arrays with a hydrophobic, CH3-terminated thiol SAM in order to minimize non-specific DNA origami adsorption. The effect of this SAM has been evaluated for selected conditions which in the previous experiments resulted in high DNA origami coverage (figure 41). Indeed, for all conditions evaluated, application of the hydrophobic SAM resulted in significantly reduced DNA origami adsorption. This clearly demonstrates the strong influence of non-specific adsorption to the Au film. However, at low incubation times, the reduced overall adsorption results in a major fraction of the nanoholes

remaining empty, while long incubation times lead to distributions with significant, albeit drastically reduced fractions of multiply
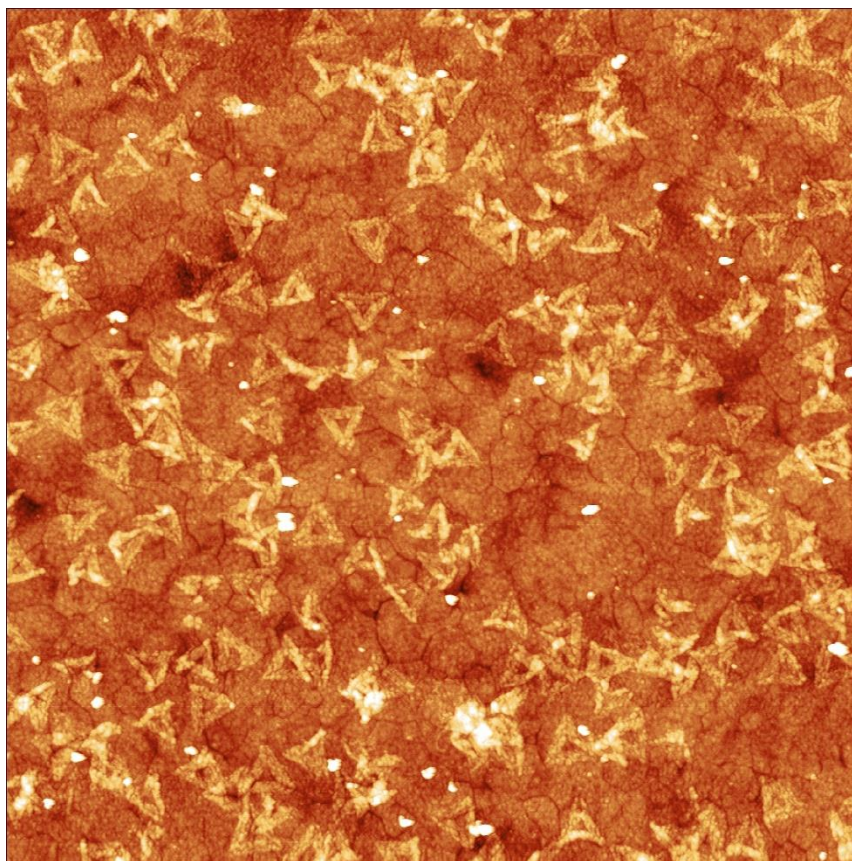
Figure 40. AFM image of a template-stripped Au surface after 1 h incubation with 1 nM DNA origami triangles in 1x TAE with 10 mM MgCl$_2$. The scan size is 2.5 x 2.5 µm² and the height scale 6 nm.

occupied nanoholes. The latter seems to be a direct result of the fact that many DNA origami are still not fully located inside the nanoholes but cross the boundary to the Au film. Since non-specific DNA origami adsorption to the gold film is blocked by the hydrophobic SAM, these observations can only be explained by the low lateral mobility of the adsorbed DNA origami nanostructures at the SiO$_2$ surface. These results thus proof that both effects, low surface mobility on the SiO$_2$ surface and parasitic adsorption to the Au surface, negatively affect adsorption specificity.

96

5.4 Conclusion

The here presented study has identified several key parameters for optimizing adsorption specificity of DNA origami nanostructures in nanohole arrays on SiO_2 surfaces.
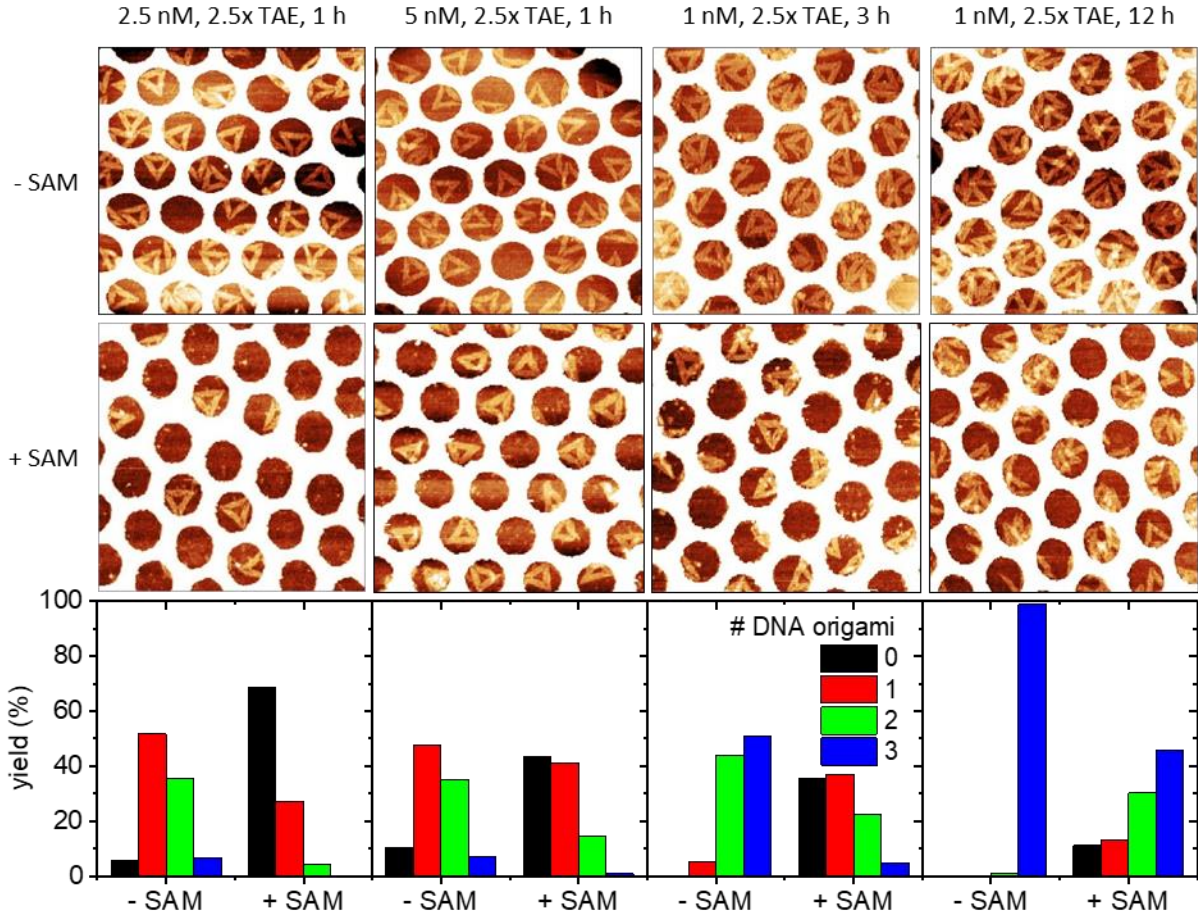
Figure 41. AFM images (1 x 1 µm², height scales 3 nm) and corresponding statistical analyses of DNA origami triangles adsorbed under different conditions in 160 nm nanohole arrays with (+ SAM) and without (- SAM) application of a hydrophobic thiol SAM. DNA origami concentrations, buffer strengths, and incubation times are given in the figure.

In particular, comparatively high yields of nanoholes occupied by single DNA origami may be obtained for low DNA origami and $MgCl_2$ concentrations of about 1 nM and 10 mM, respectively, low buffer strength, and long incubation times exceeding 12 h.

Furthermore, the strength of the adsorption buffer was found to have a surprisingly strong influence on directed DNA origami adsorption and may drastically alter the dependencies on the other parameters. However, even under optimized conditions, many of the adsorbed DNA origami are not located completely inside the nanoholes but rather cross the boundary to the surrounding Au film. This partial DNA origami adsorption can be attributed to parasitic adsorption of DNA origami to the surface of the Au film and the low surface mobility of adsorbed DNA origami on the SiO_2 surface which prevents them from maximizing their contact area with the oxide surface.

While we have shown that parasitic adsorption to the Au film can be minimized by application of a hydrophobic thiol SAM, the problem of reduced lateral mobility may be addressed in future experiments by using different substrate materials for nanohole array fabrication. Since most nanohole array sensors require optical access to both interfaces of the metal film,[290] various transparent substrates may be worth investigating with regard to DNA origami adsorption, especially the multitude of optical glasses but also other optically transparent substrates such as sapphire or indium tin oxide. Furthermore, surface mobility of the DNA origami nanostructures may also be affected by the fabrication process of the nanoholes and especially the different plasma treatment steps, as it is well known that the surface energy of SiO_2 crucially depends on the nature and history of the specimens.[294]

As an alternative strategy, the DNA origami design may be tailored with regard to the nanohole dimension and geometry. For the circular nanoholes used in the present study, a disk-shaped DNA origami with the same diameter as the nanoholes may occupy the whole surface area available at the bottom and thus be able to block or at least reduce partial adsorption of other DNA origami disks in the same nanohole. However, due to the limited scalability of DNA origami size, this approach will be restricted to a rather narrow range of nanohole diameters. Since single-layer DNA

origami nanostructures other than the triangles used here are typically rather floppy and show a certain tendency to rolling up,[295] stiffer multilayer DNA origami are most likely more efficient in avoiding partial adsorption. This, however, will restrict the accessible size range even further.

Finally, the nanohole arrays employed in above studies feature a rather thin Au film of nominally 12 nm thickness in order to facilitate imaging of the bottoms of the nanoholes by AFM. For most plasmonics-based sensing applications, however, films with thicknesses of the order of 100 nm are required.[290] For such nanohole arrays, diffusion of the comparatively large DNA origami nanostructures through the narrow nanochannels will affect adsorption kinetics and become more and more dominant the closer the nanohole diameter approaches the size of the DNA origami.[296] On the other hand, higher sidewalls may also more efficiently confine the DNA origami to the exposed SiO_2 surface and thus further reduce the occurrence of partial DNA origami adsorption, especially for mechanically rigid DNA origami designs.

6. Summary

In this thesis, DNA origami triangle's structural stability under denaturing conditions and their application in molecular patterning are discussed. DNA origami nanostructures have been extensively reported for immobilization of biomolecules, inorganic, organic nanomaterials for biophysical, biochemical characterization, drug delivery, nanorobotics, plasmonic studies. Owing to their efficient addressability for attachment of molecules of interest, for instance, to study drug delivery and the conformation dynamics of proteins using FRET, there is a growing need to study the structural stability of DNA origami nanostructures under nonbiological and biological conditions.

Therefore, in chapter 2, the structural stability of DNA origami triangles was investigated under the denaturing conditions with dependent to temperature using AFM. Guanidium chloride (GdmCl) and urea were used in this experiment which are potent denaturing agents that disrupt the native structure of a biomolecule. In our study, we have treated DNA origami triangles with 1M, 2M, 4M and 6M concentrations of chaotropes at 23°C, 30°C, 37°C and 42°C for 1 hour. Previously, melting temperature of DNA origami triangles was analyzed using fluorimetry in the presence of chaotropes. The reduction in melting temperature by chaotropes was measured as 2.76°C M^{-1} for urea and 5.84°C M^{-1} for GdmCl. Due to the number of staples strands with a large spectrum of individual melting temperature, the global melting temperature of DNA origami triangle cannot be assessed using fluorimetry analysis alone. AFM analysis of chaotropes treated DNA origami triangles showed that there is a different degree of structural damages for both the chaotropes. Since the trapezoids in DNA origami triangle has relatively less melting temperature than other staples in a triangle, the attack begins in the trapezoids and thus are particularly sensitive toward denaturant attacks. At a 6M concentration of both the chaotropes, the DNA origami structures were found to

be completely intact at 23°C and denatured at 42°C. However, at 2M concentration, the percentage of intact triangles are higher at all temperatures than 4M treated triangles. At room temperature, the triangles were found to be stable at 6M urea and GdmCl for overnight. As a proof of concept, DNA origami triangles were functionalized with biotin-streptavidin complex and further treated with 6M urea and GdmCl at 23°C. Due to the high melting temperature of the biotin-streptavidin complex when bound, the protein complex was not denatured on DNA origami triangle, even after the overnight treatment. However, the origami found to be stable along with the protein complex. The structural stability of DNA origami triangles in the presence of urea and GdmCl at low temperatures proves that the DNA origami triangle structures are suitable, particularly for single molecule protein conformation dynamics studies.

In chapter 3, the role of cations on the stability of DNA origami triangles at 42°C in the presence of 4M GdmCl and 7M urea was studied. The concentrations were selected for urea and GdmCl to have the same reduction in melting temperature per Molar. The influence of the cation concentration on the melting temperature reduction of a staple strand from DNA origami triangle was calculated using DINAMelt web server. Presence of 7M urea and 4M GdmCl reduce the melting temperature by 19.3°C and 23.3°C respectively. From AFM investigation, it is found that the stability of DNA origami triangles at 7M urea was gradually improved by increasing concentration of Mg^{2+} and Na^+. The effect of Mg^{2+} was found to be ten times higher than Na^+. However, both the cation species promote the denaturation of DNA origami triangles in the presence of 4M GdmCl, probably due to the salting-out effect of Gdm^+. This crucial finding can be further used in DNA origami-based selective denaturation of proteins.

In chapter 4, the self-assembling property of DNA origami triangles on mica in the presence of high Na^+ concentration was used to pattern the proteins with different size, pI value and adsorbing

properties on mica. The regular nanoscale protein patterns were obtained inside the DNA origami triangle cavities and the adsorption efficiency was studied in detail with regards to the concentration of Mg^{2+} and incubation time on the surface. In the case of single-stranded annealing proteins Redβ and SAK, the number of proteins inside the DNA masks can be varied and controlled from single proteins to multiple proteins. Mg^{2+} in the adsorption buffer increases the number of Redβ proteins with increasing concentration. Additionally, to assess the influence of the size of a protein in adsorption, a GFP tagged Redβ protein was used in one adsorption experiment. GFP tagged Redβ has bulky extensions from outer circle, so only one GFP tagged protein occupied the cavity at a prominent adsorption condition for 3 Redβ proteins. Moreover, due to the small size of SAK proteins, the exact number of absorbed proteins couldn't be quantified. The aggregating property of iron storage protein – ferritin, reduces the efficiency of patterning whereas a soft protein BSA immediately and efficiently occupies the available cavities. The firm attachment of BSA proteins on mica helps in selective removal of DNA origami masks using 200mM Na^+ and thus provides a nanoscale protein pattern on mica. Further, the selection of proteins for the patterning experiment and regular problems in the DNA origami self-assembled monolayer preparation have been discussed with examples.

In the last chapter, the criteria to optimize the adsorption of DNA origami triangles inside nanohole arrays was studied. Firstly, the influence of different DNA origami and Mg^{2+} concentrations in adsorption buffer on patterning was characterized. The low concentration of DNA origami, low Mg^{2+} concentration, low adsorption buffer strength and maximum incubation time were found to be optimal for the high yield. Apparently higher adsorption buffer strength also drastically influences the adsorption from single origami to multiple origami. Due to the random adsorption of DNA origami triangles on gold film and week mobility of DNA origami on the SiO_2 surface, the yield of single origami in nanohole arrays did not achieve more than 50%. However, this study

with detailed information on the role of buffer strength, DNA origami concentration and incubation time in DNA origami adsorption gives a basic knowledge to improve the criteria further.

7. References

(1) Abbott, S., Fairbanks, D. J. Experiments on Plant Hybrids by Gregor Mendel. *Genetics* **2016**, *204*, 407–422.

(2) Gericke, N. M., Hagberg, M. Definition of historical models of gene function and their relation to students' understanding of genetics. *Sci & Educ* **2007**, *16*, 849–881.

(3) Heard, E., Martienssen, R. A. Transgenerational epigenetic inheritance: Myths and mechanisms. *Cell* **2014**, *157*, 95–109.

(4) Carroll, S. B. Evo-devo and an expanding evolutionary synthesis: A genetic theory of morphological evolution. *Cell* **2008**, *134*, 25–36.

(5) Hopkin, K. The Evolving Definition of a Gene. *BioScience* **2009**, *59*, 928–931.

(6) Griffith, F. The Significance of Pneumococcal Types. *J. Hyg.* **1928**, *27*, 113–159.

(7) Avery, O. T. Studies on the chemical nature of the substance inducing transformation of pneumococcal types: induction of transformation by a desoxyribonucleic acid fraction isolated from pneumococcus type iii. *Journal of Experimental Medicine* **1944**, *79*, 137–158.

(8) Hershey, A. D., Chase, M. Independent functions of viral protein and nucleic acid in growth of bacteriophage. *The Journal of general physiology* **1952**, *36*, 39–56.

(9) Wilkins, M. H. F., Stokes, A. R., Wilson, H. R. Molecular structure of deoxypentose nucleic acids. *Nature* **1953**, *171*, 738–740.

(10) Franklin, R. E., Gosling, R. G. Molecular Configuration in Sodium Thymonucleate. *Nature* **1953**, *171*, 740–741.

(11) Watson, J. D., Crick, F. H. C. Molecular Structure of Nucleic Acids: A Structure for Deoxyribose Nucleic Acid. *Nature* **1953**, *171*, 737–738.

(12) Pauling, L., Corey, R. B. A Proposed Structure For The Nucleic Acids. *Proceedings of the National Academy of Sciences of the United States of America* **1953**, *39*, 84–97.

(13) Elson, D., Chargaff, E. On the desoxyribonucleic acid content of sea urchin gametes. *Experientia* **1952**, *8*, 143–145.

(14) Chargaff, E., Lipshitz, R., Green, C. Composition of the desoxypentose nucleic acids of four genera of sea-urchin. *The Journal of biological chemistry* **1952**, *195*, 155–160.

(15) Crick, F. Central Dogma of Molecular Biology. *Nature* **1970**, *227*, 561–563.

(16) Michelson, A. M., Todd, A. R. Nucleotides part XXXII. Synthesis of a dithymidine dinucleotide containing a 3′: 5′-internucleotidic linkage. *J. Chem. Soc.* **1955**, *0*, 2632–2638.

(17) Khorana, H. Total synthesis of a gene. *Science* **1979**, *203*, 614–625.

(18) Nishimura, S., Jones, D. S., Khorana, H. G. Studies on polynucleotides. 48. The in vitro synthesis of a co-polypeptide containing two amino acids in alternating sequence dependent upon a DNA-like polymer containing two nucleotides in alternating sequence. *Journal of Molecular Biology* **1965**, *13*, 302–324.

(19) Holley, R. W., Everett, G. A., Madison, J. T., Zamir, A. Nucleotide sequences in the yeast alanine transfer ribonucleic acid. *The Journal of biological chemistry* **1965**, *240*, 2122–2128.

(20) Huberman, J. A., Riggs, A. D. On the mechanism of DNA replication in mammalian chromosomes. *Journal of Molecular Biology* **1968**, *32*, 327–341.

(21) Lehman, I. R. Discovery of DNA polymerase. *The Journal of biological chemistry* **2003**, *278*, 34733–34738.

(22) Lehman, I. R., Bessman, M. J., Simms, E. S., Kornberg, A. Enzymatic Synthesis of Deoxyribonucleic Acid I. Preparation of substrates and partial purification of an enzyme from Escherichia Coli. *J. Biol. Chem.* **1958**, *233*, 163–170.

(23) Bessman, M. J., Lehman, I. R., Simms, E. S., Kornberg, A. Enzymatic Synthesis of Deoxyribonucleic Acid II. General properties of the reaction. *J. Biol. Chem.* **1958**, *233*, 171–177.

(24) Mullis, K. B., Faloona, F. A. [21] Specific synthesis of DNA in vitro via a polymerase-catalyzed chain reaction. In *Recombinant DNA*; Wu, R., Ed.; Academic Press: San Diego, Calif., 1987; Vols. 155, pp. 335–350.

(25) Aaij, C., Borst, P. The gel electrophoresis of DNA. *Biochimica et Biophysica Acta (BBA) - Nucleic Acids and Protein Synthesis* **1972**, *269*, 192–200.

(26) Asenjo, J. A., Andrews, B. A. Protein purification using chromatography: Selection of type, modelling and optimization of operating conditions. *Journal of molecular recognition JMR* **2009**, *22*, 65–76.

(27) Feynman, R. P. There's plenty of room at the bottom [data storage]. *J. Microelectromech. Syst.* **1992**, *1*, 60–66.

(28) N.Taniguchi, Ed. (1974). On the Basic Concept of Nano-Technology: Tokyo; Proc. Intl. Conf. Prod. Eng. Japan Society of Precision Engineering.

(29) Dowling, A. P. Development of nanotechnologies. *Materials Today* **2004**, *7*, 30–35.

(30) Fang, F. Z., Zhang, X. D., Gao, W., Guo, Y. B., Byrne, G., Hansen, H. N. Nanomanufacturing—Perspective and applications. *CIRP Annals* **2017**, *66*, 683–705.

(31) Bai C. *Scanning tunneling microscopy and its applications,* 2nd ed.; Springer: Shanghai, 2000.

(32) Binnig, Quate, Gerber. Atomic force microscope. *Physical review letters* **1986**, *56*, 930–933.

(33) Cappella, B., Dietler, G. Force-distance curves by atomic force microscopy. *Surface Science Reports* **1999**, *34*, 1–104.

(34) Cohen, S. N., Chang, A. C., Boyer, H. W., Helling, R. B. Construction of biologically functional bacterial plasmids in vitro. *Proceedings of the National Academy of Sciences of the United States of America* **1973**, *70*, 3240–3244.

(35) Baeshen, N. A., Baeshen, M. N., Sheikh, A., Bora, R. S., Ahmed, M. M. M., Ramadan, H. A. I., Saini, K. S., Redwan, E. M. Cell factories for insulin production. *Microbial cell factories* **2014**, *13*, 141.

(36) Seeman, N. C. Nucleic Acid Junctions and Lattices. *J. Theor. Biol.* **1982**, *99*, 237–247.

(37) Holliday, R. A mechanism for gene conversion in fungi. *Genet. Res.* **1964**, *5*, 282.

(38) Meselson, M. S., Radding, C. M. A general model for genetic recombination. *Proceedings of the National Academy of Sciences of the United States of America* **1975**, *72*, 358–361.

(39) Broker, T. R., Lehman, I. R. Branched DNA molecules: Intermediates in T4 recombination. *Journal of Molecular Biology* **1971**, *60*, 131–149.

(40) Lu, M., Guo, Q., Mueller, J. E., Kemper, B., Studier, F. W., Seeman, N. C., Kallenbach, N. R. Characterization of a bimobile DNA junction. *The Journal of biological chemistry* **1990**, *265*, 16778–16785.

(41) Chen, J. H., Seeman, N. C. Synthesis from DNA of a molecule with the connectivity of a cube. *Nature* **1991**, *350*, 631–633.

(42) Goodman, R. P., Berry, R. M., Turberfield, A. J. The single-step synthesis of a DNA tetrahedron. *Chem. Commun.* **2004**, 1372–1373.

(43) Zhang, Y., Seeman, N. C. Construction of a DNA-Truncated Octahedron. *Journal of the American Chemical Society* **1994**, *116*, 1661–1669.

(44) Fu, T. J., Seeman, N. C. DNA double-crossover molecules. *Biochemistry* **1993**, *32*, 3211–3220.

(45) Winfree, E., Liu, F., Wenzler, L. A., Seeman, N. C. Design and Self-Assembly of Two-Dimensional DNA Crystals. *Nature* **1998**, *394*, 539–544.

(46) Rothemund, P. W. K. Folding DNA to create nanoscale shapes and patterns. *Nature* **2006**, *440*, 297–302.

(47) He, Y., Chen, Y., Liu, H., Ribbe, A. E., Mao, C. Self-Assembly of Hexagonal DNA Two-Dimensional (2D) Arrays. *J. Am. Chem. Soc.* **2005**, *127*, 12202–12203.

(48) LaBean, T. H., Yan, H., Kopatsch, J., Liu, F., Winfree, E., Reif, J. H., Seeman, N. C. Construction, Analysis, Ligation, and Self-Assembly of DNA Triple Crossover Complexes. *J. Am. Chem. Soc.* **2000**, *122*, 1848–1860.

(49) Yan, H., Park, S. H., Finkelstein, G., Reif, J. H., LaBean, T. H. DNA-Templated Self-Assembly of Protein Arrays and Highly Conductive Nanowires. *Science* **2003**, *301*, 1882–1884.

(50) Zheng, J., Birktoft, J. J., Chen, Y., Wang, T., Sha, R., Constantinou, P. E., Ginell, S. L., Mao, C., Seeman, N. C. From Molecular to Macroscopic via the Rational Design of a Self-Assembled 3D DNA Crystal. *Nature* **2009**, *461*, 74–77.

(51) Zhang, F., Nangreave, J., Liu, Y., Yan, H. Structural DNA nanotechnology: state of the art and future perspective. *Journal of the American Chemical Society* **2014**, *136*, 11198–11211.

(52) Pinheiro, A. V., Han, D., Shih, W. M., Yan, H. Challenges and opportunities for structural DNA nanotechnology. *Nature nanotechnology* **2011**, *6*, 763–772.

(53) Zahid, M., Kim, B., Hussain, R., Amin, R., Park, S. H. DNA nanotechnology: a future perspective. *Nanoscale research letters* **2013**, *8*, 119.

(54) Nangreave, J., Han, D., Liu, Y., Yan, H. DNA origami: a history and current perspective. *Current opinion in chemical biology* **2010**, *14*, 608–615.

(55) Tørring, T., Voigt, N. V., Nangreave, J., Yan, H., Gothelf, K. V. DNA origami: a quantum leap for self-assembly of complex structures. *Chemical Society reviews* **2011**, *40*, 5636–5646.

(56) Seeman, N. C. Nanomaterials based on DNA. *Annual review of biochemistry* **2010**, *79*, 65–87.

(57) Li, Z., Liu, M., Wang, L., Nangreave, J., Yan, H., Liu, Y. Molecular Behavior of DNA Origami in Higher-Order Self-Assembly. *J. Am. Chem. Soc.* **2010**, *132*, 13545–13552.

(58) Endo, M., Sugita, T., Katsuda, Y., Hidaka, K., Sugiyama, H. Programmed-Assembly System Using DNA Jigsaw Pieces. *Chem. - Eur. J.* **2010**, *16*, 5362–5368.

(59) Liu, W., Zhong, H., Wang, R., Seeman, N. C. Crystalline Two-Dimensional DNA-Origami Arrays. *Angew. Chem. Int. Ed.* **2011**, *50*, 264–267.

(60) Rajendran, A., Endo, M., Katsuda, Y., Hidaka, K., Sugiyama, H. Programmed Two-Dimensional Self-Assembly of Multiple DNA Origami Jigsaw Pieces. *ACS nano* **2011**, *5*, 665–671.

(61) Zhao, Z., Yan, H., Liu, Y. A Route to Scale up DNA Origami using DNA Tiles as Folding Staples. *Angew. Chem. Int. Ed.* **2010**, *49*, 1414–1417.

(62) Zhao, Z., Liu, Y., Yan, H. Organizing DNA Origami Tiles into Larger Structures using Preformed Scaffold Frames. *Nano Lett.* **2011**, *11*, 2997–3002.

(63) Suzuki, Y., Endo, M., Sugiyama, H. Lipid-Bilayer-Assisted Two-Dimensional Self-Assembly of DNA Origami Nanostructures. *Nat. Commun.* **2015**, *6*, 8052.

(64) Woo, S., Rothemund, P. W. K. Self-assembly of two-dimensional DNA origami lattices using cation-controlled surface diffusion. *Nature communications* **2014**, *5*, 4889.

(65) Aghebat Rafat, A., Pirzer, T., Scheible, M. B., Kostina, A., Simmel, F. C. Surface-Assisted Large-Scale Ordering of DNA Origami Tiles. *Angew. Chem. Int. Ed.* **2014**, *53*, 7665–7668.

(66) Kopielski, A., Csaki, A., Fritzsche, W. Surface Mobility and Ordered Rearrangement of Immobilized DNA Origami. *Langmuir* **2015**, *31*, 12106–12110.

(67) Kocabey, S., Kempter, S., List, J., Xing, Y., Bae, W., Schiffels, D., Shih, W. M., Simmel, F. C., Liedl, T. Membrane-Assisted Growth of DNA Origami Nanostructure Arrays. *ACS nano* **2015**, *9*, 3530–3539.

(68) Kuzyk, A., Schreiber, R., Fan, Z., Pardatscher, G., Roller, E.-M., Högele, A., Simmel, F. C., Govorov, A. O., Liedl, T. DNA-based self-assembly of chiral plasmonic nanostructures with tailored optical response. *Nature* **2012**, *483*, 311–314.

(69) Samanta, A., Deng, Z., Liu, Y. Infrared emitting quantum dots: DNA conjugation and DNA origami directed self-assembly. *Nanoscale* **2014**, *6*, 4486–4490.

(70) Wang, D., Capehart, S. L., Pal, S., Liu, M., Zhang, L., Schuck, P. J., Liu, Y., Yan, H., Francis, M. B., Yoreo, J. J. de. Hierarchical assembly of plasmonic nanostructures using virus capsid scaffolds on DNA origami templates. *ACS nano* **2014**, *8*, 7896–7904.

(71) Steinhauer, C., Jungmann, R., Sobey, T. L., Simmel, F. C., Tinnefeld, P. DNA origami as a nanoscopic ruler for super-resolution microscopy. *Angewandte Chemie (International ed. in English)* **2009**, *48*, 8870–8873.

(72) Yamazaki, T., Heddle, J. G., Kuzuya, A., Komiyama, M. Orthogonal enzyme arrays on a DNA origami scaffold bearing size-tunable wells. *Nanoscale* **2014**, *6*, 9122–9126.

(73) Keller, A., Rackwitz, J., Cauët, E., Liévin, J., Körzdörfer, T., Rotaru, A., Gothelf, K. V., Besenbacher, F., Bald, I. Sequence dependence of electron-induced DNA strand breakage revealed by DNA nanoarrays. *Scientific reports* **2014**, *4*, 7391.

(74) Rajendran, A., Endo, M., Hidaka, K., Sugiyama, H. Direct and single-molecule visualization of the solution-state structures of G-hairpin and G-triplex intermediates. *Angewandte Chemie (International ed. in English)* **2014**, *53*, 4107–4112.

(75) Bald, I., Keller, A. Molecular processes studied at a single-molecule level using DNA origami nanostructures and atomic force microscopy. *Molecules (Basel, Switzerland)* **2014**, *19*, 13803–13823.

(76) Rajendran, A., Endo, M., Sugiyama, H. Single-molecule analysis using DNA origami. *Angewandte Chemie (International ed. in English)* **2012**, *51*, 874–890.

(77) Surwade, S. P., Zhou, F., Li, Z., Powell, A., O'Donnell, C., Liu, H. Nanoscale Patterning of Self-Assembled Monolayers using DNA Nanostructure Templates. *Chem. Commun.* **2016**, *52*, 1677–1680.

(78) Ramakrishnan, S., Subramaniam, S., Stewart, A. F., Grundmeier, G., Keller, A. Regular Nanoscale Protein Patterns via Directed Adsorption through Self-Assembled DNA Origami Masks. *ACS applied materials & interfaces* **2016**, *8*, 31239–31247.

(79) Shen, B., Linko, V., Tapio, K., Kostiainen, M. A., Toppari, J. J. Custom-Shaped Metal Nanostructures Based on DNA Origami Silhouettes. *Nanoscale* **2015**, *7*, 11267–11272.

(80) Pearson, A. C., Liu, J., Pound, E., Uprety, B., Woolley, A. T., Davis, R. C., Harb, J. N. DNA origami metallized site specifically to form electrically conductive nanowires. *J. Phys. Chem. B* **2012**, *116*, 10551–10560.

(81) Uprety, B., Westover, T., Stoddard, M., Brinkerhoff, K., Jensen, J., Davis, R. C., Woolley, A. T., Harb, J. N. Anisotropic Electroless Deposition on DNA Origami Templates To Form Small Diameter Conductive Nanowires. *Langmuir* **2017**, *33*, 726–735.

(82) Teschome, B., Facsko, S., Schonherr, T., Kerbusch, J., Keller, A., Erbe, A. Temperature-Dependent Charge Transport through Individually Contacted DNA Origami-Based Au Nanowires. *Langmuir* **2016**, *32*, 10159–10165.

(83) Vogele, K., List, J., Pardatscher, G., Holland, N. B., Simmel, F. C., Pirzer, T. Self-Assembled Active Plasmonic Waveguide with a Peptide-Based Thermomechanical Switch. *ACS Nano* **2016**, *10*, 11377–11384.

(84) Prinz, J., Schreiber, B., Olejko, L., Oertel, J., Rackwitz, J., Keller, A., Bald, I. DNA Origami Substrates for Highly Sensitive Surface-Enhanced Raman Scattering. *J. Phys. Chem. Lett.* **2013**, *4*, 4140–4145.

(85) Acuna, G. P., Möller, F. M., Holzmeister, P., Beater, S., Lalkens, B., Tinnefeld, P. Fluorescence enhancement at docking sites of DNA-directed self-assembled nanoantennas. *Science (New York, N.Y.)* **2012**, *338*, 506–510.

(86) Zhao, Y.-X., Shaw, A., Zeng, X., Benson, E., Nyström, A. M., Högberg, B. DNA origami delivery system for cancer therapy with tunable release properties. *ACS nano* **2012**, *6*, 8684–8691.

(87) Zhuang, X., Ma, X., Xue, X., Jiang, Q., Song, L., Dai, L., Zhang, C., Jin, S., Yang, K., Ding, B., Wang, P. C., Liang, X.-J. A Photosensitizer-Loaded DNA Origami Nanosystem for Photodynamic Therapy. *ACS Nano* **2016**, *10*, 3486–3495.

(88) Ora, A., Jarvihaavisto, E., Zhang, H., Auvinen, H., Santos, H. A., Kostiainen, M. A., Linko, V. Cellular delivery of enzyme-loaded DNA origami. *Chem. Commun.* **2016**, *52*, 14161–14164.

(89) Vert, M., Doi, Y., Hellwich, K.-H., Hess, M., Hodge, P., Kubisa, P., Rinaudo, M., Schué, F. Terminology for biorelated polymers and applications (IUPAC Recommendations 2012). *Pure and Applied Chemistry* **2012**, *84*, 1410.

(90) Yakovchuk, P., Protozanova, E., Frank-Kamenetskii, M. D. Base-stacking and base-pairing contributions into thermal stability of the DNA double helix. *Nucleic acids research* **2006**, *34*, 564–574.

(91) Tan, Z.-J., Chen, S.-J. Nucleic acid helix stability: effects of salt concentration, cation valence and size, and chain length. *Biophysical Journal* **2006**, *90*, 1175–1190.

(92) Kim, H., Surwade, S. P., Powell, A., O'Donnell, C., Liu, H. Stability of DNA Origami Nanostructure under Diverse Chemical Environments. *Chem. Mater.* **2014**, *26*, 5265–5273.

(93) Jiang, Z., Zhang, S., Yang, C., Kjems, J., Huang, Y., Besenbacher, F., Dong, M. Serum-induced degradation of 3D DNA box origami observed with high-speed atomic force microscopy. *Nano Res.* **2015**, *8*, 2170–2178.

(94) Wang, D., Da, Z., Zhang, B., Isbell, M. A., Dong, Y., Zhou, X., Liu, H., Heng, J. Y. Y., Yang, Z. Stability study of tubular DNA origami in the presence of protein crystallisation buffer. *RSC Adv* **2015**, *5*, 58734–58737.

(95) Hahn, J., Wickham, S. F. J., Shih, W. M., Perrault, S. D. Addressing the instability of DNA nanostructures in tissue culture. *ACS nano* **2014**, *8*, 8765–8775.

(96) Ramakrishnan, S., Krainer, G., Grundmeier, G., Schlierf, M., Keller, A. Structural stability of DNA origami nanostructures in the presence of chaotropic agents. *Nanoscale* **2016**, *8*, 10398–10405.

(97) Castro, C. E., Kilchherr, F., Kim, D.-N., Shiao, E. L., Wauer, T., Wortmann, P., Bathe, M., Dietz, H. A primer to scaffolded DNA origami. *Nature methods* **2011**, *8*, 221–229.

(98) Mei, Q., Wei, X., Su, F., Liu, Y., Youngbull, C., Johnson, R., Lindsay, S., Yan, H., Meldrum, D. Stability of DNA origami nanoarrays in cell lysate. *Nano letters* **2011**, *11*, 1477–1482.

(99) Shen, X., Jiang, Q., Wang, J., Dai, L., Zou, G., Wang, Z.-G., Chen, W.-Q., Jiang, W., Ding, B. Visualization of the intracellular location and stability of DNA origami with a label-free fluorescent probe. *Chemical communications (Cambridge, England)* **2012**, *48*, 11301–11303.

(100) Rossetti, G., Dans, P. D., Gomez-Pinto, I., Ivani, I., Gonzalez, C., Orozco, M. The structural impact of DNA mismatches. *Nucleic acids research* **2015**, *43*, 4309–4321.

(101) Hanawalt, P. C., Spivak, G. Transcription-coupled DNA repair: two decades of progress and surprises. *Nature reviews. Molecular cell biology* **2008**, *9*, 958–970.

(102) Mackintosh, S. G., Raney, K. D. DNA unwinding and protein displacement by superfamily 1 and superfamily 2 helicases. *Nucleic acids research* **2006**, *34*, 4154–4159.

(103) Nishino, T., Morikawa, K. Structure and function of nucleases in DNA repair: shape, grip and blade of the DNA scissors. *Oncogene* **2002**, *21*, 9022–9032.

(104) Loenen, W. A. M., Dryden, D. T. F., Raleigh, E. A., Wilson, G. G., Murray, N. E. Highlights of the DNA cutters: A short history of the restriction enzymes. *Nucleic acids research* **2014**, *42*, 3–19.

(105) Nagata, S., Nagase, H., Kawane, K., Mukae, N., Fukuyama, H. Degradation of chromosomal DNA during apoptosis. *Cell death and differentiation* **2003**, *10*, 108–116.

(106) Kawane, K., Motani, K., Nagata, S. DNA degradation and its defects. *Cold Spring Harbor perspectives in biology* **2014**, *6*.

(107) Samejima, K., Earnshaw, W. C. Trashing the genome: the role of nucleases during apoptosis. *Nature reviews. Molecular cell biology* **2005**, *6*, 677–688.

(108) Xu, H., Ren, D. Lysosomal physiology. *Annual review of physiology* **2015**, *77*, 57–80.

(109) Fujiwara, Y., Kikuchi, H., Aizawa, S., Furuta, A., Hatanaka, Y., Konya, C., Uchida, K., Wada, K., Kabuta, T. Direct uptake and degradation of DNA by lysosomes. *Autophagy* **2013**, *9*, 1167–1171.

(110) Köckritz-Blickwede, M. von, Chow, O. A., Nizet, V. Fetal calf serum contains heat-stable nucleases that degrade neutrophil extracellular traps. *Blood* **2009**, *114*, 5245–5246.

(111) Lechardeur, D., Sohn, K. J., Haardt, M., Joshi, P. B., Monck, M., Graham, R. W., Beatty, B., Squire, J., O'Brodovich, H., Lukacs, G. L. Metabolic instability of plasmid DNA in the cytosol: a potential barrier to gene transfer. *Gene therapy* **1999**, *6*, 482–497.

(112) Kishi, K., Yasuda, T., Ikehara, Y., Sawazaki, K., Sato, W., Iida, R. Human serum deoxyribonuclease I (DNase I) polymorphism: pattern similarities among isozymes from serum, urine, kidney, liver, and pancreas. *American journal of human genetics* **1990**, *47*, 121–126.

(113) Prince, Baker, Dodge, Ahmed, Chestnut, Sinicropi. Pharmacodynamics of recombinant human DNase I in serum. *Clin Exp Immunol* **1998**, *113*, 289–296.

(114) Suri, S. S., Fenniri, H., Singh, B. Nanotechnology-based drug delivery systems. *Journal of occupational medicine and toxicology (London, England)* **2007**, *2*, 16.

(115) Jong, W. H. de, Borm, P. J. A. Drug delivery and nanoparticles:applications and hazards. *International journal of nanomedicine* **2008**, *3*, 133–149.

(116) Winter, E., Dal Pizzol, C., Locatelli, C., Crezkynski-Pasa, T. B. Development and Evaluation of Lipid Nanoparticles for Drug Delivery: Study of Toxicity In, Vitro and In Vivo. *Journal of nanoscience and nanotechnology* **2016**, *16*, 1321–1330.

(117) Sharma, A., Madhunapantula, S. V., Robertson, G. P. Toxicological considerations when creating nanoparticle-based drugs and drug delivery systems. *Expert opinion on drug metabolism & toxicology* **2012**, *8*, 47–69.

(118) Aryal, S., Jack Hu, C.-M., Fu, V., Zhang, L. Nanoparticledrug delivery enhances the cytotoxicity of hydrophobic–hydrophilic drug conjugates. *J. Mater. Chem.* **2012**, *22*, 994–999.

(119) Qu, C., Wang, L., He, J., Tan, J., Liu, W., Zhang, S., Zhang, C., Wang, Z., Jiao, S., Liu, S., Jiang, G. Carbon nanotubes provoke inflammation by inducing the pro-inflammatory genes IL-1β and IL-6. *Gene* **2012**, *493*, 9–12.

(120) Kobayashi, N., Izumi, H., Morimoto, Y. Review of toxicity studies of carbon nanotubes. *Journal of occupational health* **2017**, *59*, 394–407.

(121) Petersen, E. J., Henry, T. B. Ecotoxicity of Fullerenes and Carbon Nanotubes: A Critical Review of Evidence for Nano-Size Effects. In *Biotechnology and nanotechnology risk assessment: Minding and managing the potential threats around us*; Ripp, S., Henry, T. B., Eds.; American Chemical Soc: Washington, DC, 2011; Vols. 1079, pp. 103–119.

(122) Tamura, I., Kagota, K.-I., Yasuda, Y., Yoneda, S., Morita, J., Nakada, N., Kameda, Y., Kimura, K., Tatarazako, N., Yamamoto, H. Ecotoxicity and screening level ecotoxicological risk assessment of five antimicrobial agents: Triclosan, triclocarban, resorcinol, phenoxyethanol and p-thymol. *Journal of applied toxicology JAT* **2013**, *33*, 1222–1229.

(123) Manshian, B. B., Abdelmonem, A. M., Kantner, K., Pelaz, B., Klapper, M., Nardi Tironi, C., Parak, W. J., Himmelreich, U., Soenen, S. J. Evaluation of quantum dot cytotoxicity: Interpretation of nanoparticle concentrations versus intracellular nanoparticle numbers. *Nanotoxicology* **2016**, *10*, 1318–1328.

(124) Zhao, Y., Lin, K., Zhang, W., Liu, L. Quantum dots enhance Cu2+ -induced hepatic L02 cells toxicity. *Journal of environmental sciences (China)* **2010**, *22*, 1987–1992.

(125) Manke, A., Wang, L., Rojanasakul, Y. Mechanisms of nanoparticle-induced oxidative stress and toxicity. *BioMed research international* **2013**, *2013*, 942916.

(126) Feng, X., Chen, A., Zhang, Y., Wang, J., Shao, L., Wei, L. Central nervous system toxicity of metallic nanoparticles. *International journal of nanomedicine* **2015**, *10*, 4321–4340.

(127) Sercombe, L., Veerati, T., Moheimani, F., Wu, S. Y., Sood, A. K., Hua, S. Advances and Challenges of Liposome Assisted Drug Delivery. *Frontiers in pharmacology* **2015**, *6*, 286.

(128) Erben, C. M., Goodman, R. P., Turberfield, A. J. Single-molecule protein encapsulation in a rigid DNA cage. *Angewandte Chemie (International ed. in English)* **2006**, *45*, 7414–7417.

(129) Bui, H., Onodera, C., Kidwell, C., Tan, Y., Graugnard, E., Kuang, W., Lee, J., Knowlton, W. B., Yurke, B., Hughes, W. L. Programmable periodicity of quantum dot arrays with DNA origami nanotubes. *Nano letters* **2010**, *10*, 3367–3372.

(130) Du, K., Ko, S. H., Gallatin, G. M., Yoon, H. P., Liddle, J. A., Berglund, A. J. Quantum dot-DNA origami binding: a single particle, 3D, real-time tracking study. *Chemical communications (Cambridge, England)* **2013**, *49*, 907–909.

(131) Peer, D., Karp, J. M., Hong, S., Farokhzad, O. C., Margalit, R., Langer, R. Nanocarriers as an emerging platform for cancer therapy. *Nature nanotechnology* **2007**, *2*, 751–760.

(132) Jiang, Q., Song, C., Nangreave, J., Liu, X., Lin, L., Qiu, D., Wang, Z.-G., Zou, G., Liang, X., Yan, H., Ding, B. DNA origami as a carrier for circumvention of drug resistance. *Journal of the American Chemical Society* **2012**, *134*, 13396–13403.

(133) Mindell, J. A. Lysosomal acidification mechanisms. *Annual review of physiology* **2012**, *74*, 69–86.

(134) Ke, Y., Lindsay, S., Chang, Y., Liu, Y., Yan, H. Self-assembled water-soluble nucleic acid probe tiles for label-free RNA hybridization assays. *Science (New York, N.Y.)* **2008**, *319*, 180–183.

(135) Subramanian, H. K. K., Chakraborty, B., Sha, R., Seeman, N. C. The label-free unambiguous detection and symbolic display of single nucleotide polymorphisms on DNA origami. *Nano letters* **2011**, *11*, 910–913.

(136) Godonoga, M., Lin, T.-Y., Oshima, A., Sumitomo, K., Tang, M. S. L., Cheung, Y.-W., Kinghorn, A. B., Dirkzwager, R. M., Zhou, C., Kuzuya, A., Tanner, J. A., Heddle, J. G. A DNA aptamer recognising a malaria protein biomarker can function as part of a DNA origami assembly. *Scientific reports* **2016**, *6*, 21266.

(137) Conway, J. W., McLaughlin, C. K., Castor, K. J., Sleiman, H. DNA nanostructure serum stability: greater than the sum of its parts. *Chemical communications (Cambridge, England)* **2013**, *49*, 1172–1174.

(138) Linko, V., Ora, A., Kostiainen, M. A. DNA Nanostructures as Smart Drug-Delivery Vehicles and Molecular Devices. *Trends in biotechnology* **2015**, *33*, 586–594.

(139) Douglas, S. M., Bachelet, I., Church, G. M. A logic-gated nanorobot for targeted transport of molecular payloads. *Science (New York, N.Y.)* **2012**, *335*, 831–834.

(140) Andersen, E. S., Dong, M., Nielsen, M. M., Jahn, K., Subramani, R., Mamdouh, W., Golas, M. M., Sander, B., Stark, H., Oliveira, C. L. P., Pedersen, J. S., Birkedal, V., Besenbacher, F., Gothelf, K. V., Kjems, J. Self-assembly of a nanoscale DNA box with a controllable lid. *Nature* **2009**, *459*, 73–76.

(141) Marras, A. E., Zhou, L., Su, H.-J., Castro, C. E. Programmable motion of DNA origami mechanisms. *Proceedings of the National Academy of Sciences of the United States of America* **2015**, *112*, 713–718.

(142) Takenaka, T., Endo, M., Suzuki, Y., Yang, Y., Emura, T., Hidaka, K., Kato, T., Miyata, T., Namba, K., Sugiyama, H. Photoresponsive DNA nanocapsule having an open/close system for capture and release of nanomaterials. *Chemistry (Weinheim an der Bergstrasse, Germany)* **2014**, *20*, 14951–14954.

(143) Langecker, M., Arnaut, V., Martin, T. G., List, J., Renner, S., Mayer, M., Dietz, H., Simmel, F. C. Synthetic lipid membrane channels formed by designed DNA nanostructures. *Science (New York, N.Y.)* **2012**, *338*, 932–936.

(144) Pedersen, R. O., Loboa, E. G., LaBean, T. H. Sensitization of transforming growth factor-β signaling by multiple peptides patterned on DNA nanostructures. *Biomacromolecules* **2013**, *14*, 4157–4160.

(145) Schaffert, D. H., Okholm, A. H., Sørensen, R. S., Nielsen, J. S., Tørring, T., Rosen, C. B., Kodal, A. L. B., Mortensen, M. R., Gothelf, K. V., Kjems, J. Intracellular Delivery of a Planar DNA Origami Structure by the Transferrin-Receptor Internalization Pathway. *Small (Weinheim an der Bergstrasse, Germany)* **2016**, *12*, 2634–2640.

(146) Arnon, S., Dahan, N., Koren, A., Radiano, O., Ronen, M., Yannay, T., Giron, J., Ben-Ami, L., Amir, Y., Hel-Or, Y., Friedman, D., Bachelet, I. Thought-Controlled Nanoscale Robots in a Living Host. *PloS one* **2016**, *11*, e0161227.

(147) Amir, Y., Ben-Ishay, E., Levner, D., Ittah, S., Abu-Horowitz, A., Bachelet, I. Universal computing by DNA origami robots in a living animal. *Nature nanotechnology* **2014**, *9*, 353–357.

(148) Walsh, A. S., Yin, H., Erben, C. M., Wood, M. J. A., Turberfield, A. J. DNA cage delivery to mammalian cells. *ACS nano* **2011**, *5*, 5427–5432.

(149) Keum, J.-W., Bermudez, H. Enhanced resistance of DNA nanostructures to enzymatic digestion. *Chemical communications (Cambridge, England)* **2009**, 7036–7038.

(150) Perrault, S. D., Shih, W. M. Virus-inspired membrane encapsulation of DNA nanostructures to achieve in vivo stability. *ACS nano* **2014**, *8*, 5132–5140.

(151) Kiviaho, J. K., Linko, V., Ora, A., Tiainen, T., Järvihaavisto, E., Mikkilä, J., Tenhu, H., Nonappa, Kostiainen, M. A. Cationic polymers for DNA origami coating - examining their binding efficiency and tuning the enzymatic reaction rates. *Nanoscale* **2016**, *8*, 11674–11680.

(152) Agarwal, N. P., Matthies, M., Gür, F. N., Osada, K., Schmidt, T. L. Block Copolymer Micellization as a Protection Strategy for DNA Origami. *Angewandte Chemie (International ed. in English)* **2017**, *56*, 5460–5464.

(153) Ponnuswamy, N., Bastings, M. M. C., Nathwani, B., Ryu, J. H., Chou, L. Y. T., Vinther, M., Li, W. A., Anastassacos, F. M., Mooney, D. J., Shih, W. M. Oligolysine-based coating protects DNA nanostructures from low-salt denaturation and nuclease degradation. *Nat. Commun.* **2017**, *8*, 15654.

(154) Chopra, A., Krishnan, S., Simmel, F. C. Electrotransfection of Polyamine Folded DNA Origami Structures. *Nano Lett.* **2016**, *16*, 6683–6690.

(155) Auvinen, H., Zhang, H., Nonappa, Kopilow, A., Niemelä, E. H., Nummelin, S., Correia, A., Santos, H. A., Linko, V., Kostiainen, M. A. Protein Coating of DNA Nanostructures for Enhanced Stability and Immunocompatibility. *Adv. Healthc. Mater.* **2017**.

(156) Estrich, N. A., Hernandez-Garcia, A., Vries, R. de, LaBean, T. H. Engineered Diblock Polypeptides Improve DNA and Gold Solubility during Molecular Assembly. *ACS Nano* **2017**, *11*, 831–842.

(157) Russell, A. P., Holleman, D. S. The thermal denaturation of DNA: average length and composition of denatured areas. *Nucl Acids Res* **1974**, *1*, 959–978.

(158) Owczarzy, R., Moreira, B. G., You, Y., Behlke, M. A., Walder, J. A. Predicting stability of DNA duplexes in solutions containing magnesium and monovalent cations. *Biochemistry* **2008**, *47*, 5336–5353.

(159) Gerling, T., Wagenbauer, K. F., Neuner, A. M., Dietz, H. Dynamic DNA devices and assemblies formed by shape-complementary, non-base pairing 3D components. *Science (New York, N.Y.)* **2015**, *347*, 1446–1452.

(160) Jungmann, R., Liedl, T., Sobey, T. L., Shih, W., Simmel, F. C. Isothermal assembly of DNA origami structures using denaturing agents. *Journal of the American Chemical Society* **2008**, *130*, 10062–10063.

(161) Kopielski, A., Schneider, A., Csáki, A., Fritzsche, W. Isothermal DNA origami folding: avoiding denaturing conditions for one-pot, hybrid-component annealing. *Nanoscale* **2015**, *7*, 2102–2106.

(162) Zhang, Z., Song, J., Besenbacher, F., Dong, M., Gothelf, K. V. Self-assembly of DNA origami and single-stranded tile structures at room temperature. *Angewandte Chemie (International ed. in English)* **2013**, *52*, 9219–9223.

(163) Koirala, D., Shrestha, P., Emura, T., Hidaka, K., Mandal, S., Endo, M., Sugiyama, H., Mao, H. Single-molecule mechanochemical sensing using DNA origami nanostructures. *Angewandte Chemie (International ed. in English)* **2014**, *53*, 8137–8141.

(164) Iwaki, M., Wickham, S. F., Ikezaki, K., Yanagida, T., Shih, W. M. A programmable DNA origami nanospring that reveals force-induced adjacent binding of myosin VI heads. *Nat. Commun.* **2016**, *7*, 13715.

(165) Nickels, P. C., Wünsch, B., Holzmeister, P., Bae, W., Kneer, L. M., Grohmann, D., Tinnefeld, P., Liedl, T. Molecular force spectroscopy with a DNA origami-based nanoscopic force clamp. *Science (New York, N.Y.)* **2016**, *354*, 305–307.

(166) Pfitzner, E., Wachauf, C., Kilchherr, F., Pelz, B., Shih, W. M., Rief, M., Dietz, H. Rigid DNA beams for high-resolution single-molecule mechanics. *Angewandte Chemie (International ed. in English)* **2013**, *52*, 7766–7771.

(167) Shrestha, P., Emura, T., Koirala, D., Cui, Y., Hidaka, K., Maximuck, W. J., Endo, M., Sugiyama, H., Mao, H. Mechanical properties of DNA origami nanoassemblies are determined by Holliday junction mechanophores. *Nucleic acids research* **2016**, *44*, 6574–6582.

(168) Kauert, D. J., Kurth, T., Liedl, T., Seidel, R. Direct mechanical measurements reveal the material properties of three-dimensional DNA origami. *Nano letters* **2011**, *11*, 5558–5563.

(169) Zhou, L., Marras, A. E., Su, H.-J., Castro, C. E. DNA origami compliant nanostructures with tunable mechanical properties. *ACS nano* **2014**, *8*, 27–34.

(170) Schena, M., Shalon, D., Davis, R. W., Brown, P. O. Quantitative Monitoring of Gene Expression Patterns with a Complementary DNA Microarray. *Science* **1995**, *270*, 467–470.

(171) Gad, M., Sugiyama, S., Ohtani, T. Method for patterning stretched DNA molecules on mica surfaces by soft lithography. *Journal of biomolecular structure & dynamics* **2003**, *21*, 387–393.

(172) Gállego, I., Manning, B., Prades, J. D., Mir, M., Samitier, J., Eritja, R. DNA-Origami-Driven Lithography for Patterning on Gold Surfaces with Sub-10 nm Resolution. *Advanced materials (Deerfield Beach, Fla.)* **2017**, *29*.

(173) Ding, B., Wu, H., Xu, W., Zhao, Z., Liu, Y., Yu, H., Yan, H. Interconnecting gold islands with DNA origami nanotubes. *Nano letters* **2010**, *10*, 5065–5069.

(174) Gao, B., Sarveswaran, K., Bernstein, G. H., Lieberman, M. Guided deposition of individual DNA nanostructures on silicon substrates. *Langmuir the ACS journal of surfaces and colloids* **2010**, *26*, 12680–12683.

(175) Gerdon, A. E., Oh, S. S., Hsieh, K., Ke, Y., Yan, H., Soh, H. T. Controlled delivery of DNA origami on patterned surfaces. *Small (Weinheim an der Bergstrasse, Germany)* **2009**, *5*, 1942–1946.

(176) Kershner, R. J., Bozano, L. D., Micheel, C. M., Hung, A. M., Fornof, A. R., Cha, J. N., Rettner, C. T., Bersani, M., Frommer, J., Rothemund, P. W. K., Wallraff, G. M. Placement and orientation of individual DNA shapes on lithographically patterned surfaces. *Nature nanotechnology* **2009**, *4*, 557–561.

(177)   Gopinath, A., Rothemund, P. W. K. Optimized assembly and covalent coupling of single-molecule DNA origami nanoarrays. *ACS nano* **2014**, *8*, 12030–12040.

(178)   Gopinath, A., Miyazono, E., Faraon, A., Rothemund, P. W. K. Engineering and mapping nanocavity emission via precision placement of DNA origami. *Nature* **2016**, *535*, 401–405.

(179)   Knudsen, J. B., Liu, L., Bank Kodal, A. L., Madsen, M., Li, Q., Song, J., Woehrstein, J. B., Wickham, S. F. J., Strauss, M. T., Schueder, F., Vinther, J., Krissanaprasit, A., Gudnason, D., Smith, A. A. A., Ogaki, R., Zelikin, A. N., Besenbacher, F., Birkedal, V., Yin, P., Shih, W. M., Jungmann, R., Dong, M., Gothelf, K. V. Routing of individual polymers in designed patterns. *Nature Nanotech* **2015**, *10*, 892–898.

(180)   Liber, M., Tomov, T. E., Tsukanov, R., Berger, Y., Nir, E. A Bipedal DNA Motor that Travels Back and Forth between Two DNA Origami Tiles. *Small* **2015**, *11*, 568–575.

(181)   Tateishi-Karimata, H., Sugimoto, N. Structure, stability and behaviour of nucleic acids in ionic liquids. *Nucleic acids research* **2014**, *42*, 8831–8844.

(182)   Schuler, B., Hofmann, H. Single-molecule spectroscopy of protein folding dynamics--expanding scope and timescales. *Current opinion in structural biology* **2013**, *23*, 36–47.

(183)   Gietl, A., Holzmeister, P., Grohmann, D., Tinnefeld, P. DNA origami as biocompatible surface to match single-molecule and ensemble experiments. *Nucleic acids research* **2012**, *40*, e110-e110.

(184)   Tsukanov, R., Tomov, T. E., Berger, Y., Liber, M., Nir, E. Conformational Dynamics of DNA Hairpins at Millisecond Resolution Obtained from Analysis of Single-Molecule FRET Histograms. *J. Phys. Chem. B* **2013**, *117*, 16105–16109.

(185)   Tsukanov, R., Tomov, T. E., Masoud, R., Drory, H., Plavner, N., Liber, M., Nir, E. Detailed Study of DNA Hairpin Dynamics Using Single-Molecule Fluorescence Assisted by DNA Origami. *J. Phys. Chem. B* **2013**, *117*, 11932–11942.

(186)   Krainer, G., Hartmann, A., Schlierf, M. farFRET: Extending the Range in Single-Molecule FRET Experiments beyond 10 nm. *Nano letters* **2015**, *15*, 5826–5829.

(187)   Borgia, A., Williams, P. M., Clarke, J. Single-molecule studies of protein folding. *Annual review of biochemistry* **2008**, *77*, 101–125.

(188)   Hartmann, A., Krainer, G., Keller, S., Schlierf, M. Quantification of Millisecond Protein-Folding Dynamics in Membrane-Mimetic Environments by Single-Molecule Förster Resonance Energy Transfer Spectroscopy. *Analytical chemistry* **2015**, *87*, 11224–11232.

(189) Salvi, G., Los Rios, P. de, Vendruscolo, M. Effective interactions between chaotropic agents and proteins. *Proteins* **2005**, *61*, 492–499.

(190) Lim, V. I., Curran, J. F., Garber, M. B. Hydration shells of molecules in molecular association: A mechanism for biomolecular recognition. *Journal of theoretical biology* **2012**, *301*, 42–48.

(191) Nordstrom, L. J., Clark, C. A., Andersen, B., Champlin, S. M., Schwinefus, J. J. Effect of ethylene glycol, urea, and N-methylated glycines on DNA thermal stability: the role of DNA base pair composition and hydration. *Biochemistry* **2006**, *45*, 9604–9614.

(192) Hutton, J. R. Renaturation Kinetics and thermal stability of DNA in aqueous solutions of formamide and urea. *Nucl Acids Res* **1977**, *4*, 3537–3555.

(193) Chao, J., Zhang, P., Wang, Q., Wu, N., Zhang, F., Hu, J., Fan, C. H., Li, B. Single-molecule imaging of DNA polymerase I (Klenow fragment) activity by atomic force microscopy. *Nanoscale* **2016**, *8*, 5842–5846.

(194) Keller, A., Bald, I., Rotaru, A., Cauët, E., Gothelf, K. V., Besenbacher, F. Probing electron-induced bond cleavage at the single-molecule level using DNA origami templates. *ACS nano* **2012**, *6*, 4392–4399.

(195) Keller, A., Kopyra, J., Gothelf, K. V., Bald, I. Electron-induced damage of biotin studied in the gas phase and in the condensed phase at a single-molecule level. *New J. Phys.* **2013**, *15*, 83045.

(196) Prinz, J., Heck, C., Ellerik, L., Merk, V., Bald, I. DNA origami based Au–Ag-core–shell nanoparticle dimers with single-molecule SERS sensitivity. *Nanoscale* **2016**, *8*, 5612–5620.

(197) Vogel, S., Rackwitz, J., Schürman, R., Prinz, J., Milosavljević, A. R., Réfrégiers, M., Giuliani, A., Bald, I. Using DNA Origami Nanostructures To Determine Absolute Cross Sections for UV Photon-Induced DNA Strand Breakage. *J. Phys. Chem. Lett.* **2015**, *6*, 4589–4593.

(198) Greene, R. F., Pace, C. N. Urea and guanidine hydrochloride denaturation of ribonuclease, lysozyme, alpha-chymotrypsin, and beta-lactoglobulin. *The Journal of biological chemistry* **1974**, *249*, 5388–5393.

(199) Song, J., Arbona, J.-M., Zhang, Z., Liu, L., Xie, E., Elezgaray, J., Aime, J.-P., Gothelf, K. V., Besenbacher, F., Dong, M. Direct visualization of transient thermal response of a DNA origami. *Journal of the American Chemical Society* **2012**, *134*, 9844–9847.

(200) Markham, N. R., Zuker, M. DINAMelt web server for nucleic acid melting prediction. *Nucleic acids research* **2005**, *33*, 81.

(201) Green, N. M. Avidin and streptavidin. *Methods in enzymology* **1990**, *184*, 51–67.

(202) Holmberg, A., Blomstergren, A., Nord, O., Lukacs, M., Lundeberg, J., Uhlén, M. The biotin-streptavidin interaction can be reversibly broken using water at elevated temperatures. *Electrophoresis* **2005**, *26*, 501–510.

(203) González, M., Argaraña, C. E., Fidelio, G. D. Extremely high thermal stability of streptavidin and avidin upon biotin binding. *Biomolecular engineering* **1999**, *16*, 67–72.

(204) González, M., Bagatolli, L. A., Echabe, I., Arrondo, J. L. R., Argaraña, C. E., Cantor, C. R., Fidelio, G. D. Interaction of Biotin with Streptavidin. *The Journal of biological chemistry* **1997**, *272*, 11288–11294.

(205) Grubmüller, H., Heymann, B., Tavan, P. Ligand binding: molecular mechanics calculation of the streptavidin-biotin rupture force. *Science* **1996**, *271*, 997–999.

(206) Izrailev, S., Stepaniants, S., Balsera, M., Oono, Y., Schulten, K. Molecular dynamics study of unbinding of the avidin-biotin complex. *Biophys. J.* **1997**, *72*, 1568–1581.

(207) Waner, M. J., Navrotskaya, I., Bain, A., Oldham, E. D., Mascotti, D. P. Thermal and sodium dodecylsulfate induced transitions of streptavidin. *Biophysical Journal* **2004**, *87*, 2701–2713.

(208) Kurzban, G. P., Bayer, E. A., Wilchek, M., Horowitz, P. M. The quaternary structure of streptavidin in urea. *The Journal of biological chemistry* **1991**, *266*, 14470–14477.

(209) Green, N. M., Toms, E. J. The dissociation of avidin–biotin complexes by guanidinium chloride. *Biochem. J.* **1972**, *130*, 707–711.

(210) Dundas, C. M., Demonte, D., Park, S. Streptavidin-biotin technology: improvements and innovations in chemical and biological applications. *Applied microbiology and biotechnology* **2013**, *97*, 9343–9353.

(211) Rajendran, A., Endo, M., Katsuda, Y., Hidaka, K., Sugiyama, H. Photo-cross-linking-assisted thermal stability of DNA origami structures and its application for higher-temperature self-assembly. *Journal of the American Chemical Society* **2011**, *133*, 14488–14491.

(212) Hutton, J. R. Renaturation kinetics and thermal stability of DNA in aqueous solutions of formamide and urea. *Nucleic Acids Res.* **1977**, *4*, 3537–3555.

(213) Priyakumar, U. D., Hyeon, C., Thirumalai, D., Mackerell, A. D., JR. Urea destabilizes RNA by forming stacking interactions and multiple hydrogen bonds with nucleic acid bases. *J. Am. Chem. Soc.* **2009**, *131*, 17759–17761.

(214) Kasavajhala, K., Bikkina, S., Patil, I., Mackerell, A. D., JR, Priyakumar, U. D. Dispersion interactions between urea and nucleobases contribute to the destabilization of RNA by urea in aqueous solution. *J. Phys. Chem. B* **2015**, *119*, 3755–3761.

(215) Klump, H., Burkart, W. Calorimetric measurements of the transition enthalpy of DNA in aqueous urea solutions. *Biochimica et Biophysica Acta (BBA) - Nucleic Acids and Protein Synthesis* **1977**, *475*, 601–604.

(216) Monera, O. D., Kay, C. M., Hodges, R. S. Protein denaturation with guanidine hydrochloride or urea provides a different estimate of stability depending on the contributions of electrostatic interactions. *Protein Sci.* **1994**, *3*, 1984–1991.

(217) Smith, J. S., Scholtz, J. M. Guanidine hydrochloride unfolding of peptide helices: separation of denaturant and salt effects. *Biochemistry* **1996**, *35*, 7292–7297.

(218) Dempsey, C. E., Piggot, T. J., Mason, P. E. Dissecting contributions to the denaturant sensitivities of proteins. *Biochemistry* **2005**, *44*, 775–781.

(219) Kubíčková, A., Křížek, T., Coufal, P., Wernersson, E., Heyda, J., Jungwirth, P. Guanidinium Cations Pair with Positively Charged Arginine Side Chains in Water. *J. Phys. Chem. Lett.* **2011**, *2*, 1387–1389.

(220) Anderson, C. F., Record, M. T., JR. Salt-nucleic acid interactions. *Annu. Rev. Phys. Chem.* **1995**, *46*, 657–700.

(221) Nakano, S., Fujimoto, M., Hara, H., Sugimoto, N. Nucleic acid duplex stability: Influence of base composition on cation effects. *Nucleic Acids Res.* **1999**, *27*, 2957–2965.

(222) Ramakrishnan, S., Krainer, G., Grundmeier, G., Schlierf, M., Keller, A. Cation-Induced Stabilization and Denaturation of DNA Origami Nanostructures in Urea and Guanidinium Chloride. *Small (Weinheim an der Bergstrasse, Germany)* **2017**, *13*.

(223) Douglas, S. M., Dietz, H., Liedl, T., Högberg, B., Graf, F., Shih, W. M. Self-assembly of DNA into nanoscale three-dimensional shapes. *Nature* **2009**, *459*, 414–418.

(224) Dietz, H., Douglas, S. M., Shih, W. M. Folding DNA into twisted and curved nanoscale shapes. *Science* **2009**, *325*, 725–730.

(225) Zhang, F., Jiang, S., Wu, S., Li, Y., Mao, C., Liu, Y., Yan, H. Complex wireframe DNA origami nanostructures with multi-arm junction vertices. *Nat. Nanotechnol.* **2015**, *10*, 779–784.

(226) Han, D., Pal, S., Yang, Y., Jiang, S., Nangreave, J., Liu, Y., Yan, H. DNA gridiron nanostructures based on four-arm junctions. *Science* **2013**, *339*, 1412–1415.

(227) Benson, E., Mohammed, A., Gardell, J., Masich, S., Czeizler, E., Orponen, P., Högberg, B. DNA rendering of polyhedral meshes at the nanoscale. *Nature* **2015**, *523*, 441–444.

(228) Werner, J., Wernersson, E., Ekholm, V., Ottosson, N., Ohrwall, G., Heyda, J., Persson, I., Soderstrom, J., Jungwirth, P., Bjorneholm, O. Surface behavior of hydrated guanidinium and ammonium ions: a comparative study by photoelectron spectroscopy and molecular dynamics. *J. Phys. Chem. B* **2014**, *118*, 7119–7127.

(229) Kuzyk, A., Laitinen, K. T., Törmä, P. DNA origami as a nanoscale template for protein assembly. *Nanotechnology* **2009**, *20*, 235305.

(230) Wu, N., Zhou, X., Czajkowsky, D. M., Ye, M., Zeng, D., Fu, Y., Fan, C., Hu, J., Li, B. In Situ Monitoring of Single Molecule Binding Reactions with Time-Lapse Atomic Force Microscopy on Functionalized DNA Origami. *Nanoscale* **2011**, *3*, 2481–2484.

(231) Wong, N. Y., Xing, H., Tan, L. H., Lu, Y. Nano-Encrypted Morse Code: A Versatile Approach to Programmable and Reversible Aanoscale Assembly and Disassembly. *J. Am. Chem. Soc.* **2013**, *135*, 2931–2934.

(232) Sacca, B., Meyer, R., Erkelenz, M., Kiko, K., Arndt, A., Schroeder, H., Rabe, K. S., Niemeyer, C. M. Orthogonal Protein Decoration of DNA Origami. *Angew. Chem. Int. Ed.* **2010**, *49*, 9378–9383.

(233) Shen, W., Zhong, H., Neff, D., Norton, M. L. NTA Directed Protein Nanopatterning on DNA Origami Nanoconstructs. *J. Am. Chem. Soc.* **2009**, *131*, 6660–6661.

(234) Rinker, S., Ke, Y., Liu, Y., Chhabra, R., Yan, H. Self-Assembled DNA Nanostructures for Distance-Dependent Multivalent Ligand-Protein Binding. *Nat. Nanotechnol.* **2008**, *3*, 418–422.

(235) Chhabra, R., Sharma, J., Ke, Y., Liu, Y., Rinker, S., Lindsay, S., Yan, H. Spatially Addressable Multiprotein Nanoarrays Templated by Aptamer-Tagged DNA Nanoarchitectures. *J. Am. Chem. Soc.* **2007**, *129*, 10304–10305.

(236) Kuzuya, A., Sakai, Y., Yamazaki, T., Xu, Y., Komiyama, M. Nanomechanical DNA Origami 'Single-Molecule Beacons' Directly Imaged by Atomic Force Microscopy. *Nat. Commun.* **2011**, *2*, 449.

(237) Jahn, K., Torring, T., Voigt, N. V., Sorensen, R. S., Bank Kodal, A. L., Andersen, E. S., Gothelf, K. V., Kjems, J. Functional Patterning of DNA Origami by Parallel Enzymatic Modification. *Bioconjugate Chem.* **2011**, *22*, 819–823.

(238) Sørensen, R. S., Okholm, A. H., Schaffert, D., Kodal, A. L. B., Gothelf, K. V., Kjems, J. Enzymatic ligation of large biomolecules to DNA. *ACS nano* **2013**, *7*, 8098–8104.

(239) Filipponi, L., Livingston, P., Kaspar, O., Tokarova, V., Nicolau, D. V. Protein Patterning by Microcontact Printing using Pyramidal PDMS Stamps. *Biomed. Microdevices* **2016**, *18*, 9.

(240) Delaney, J. T., Smith, P. J., Schubert, U. S. Inkjet Printing of Proteins. *Soft Matter* **2009**, *5*, 4866.

(241) Denis, F. A., Pallandre, A., Nysten, B., Jonas, A. M., Dupont-Gillain, C. C. Alignment and Assembly of Adsorbed Collagen Molecules Induced by Anisotropic Chemical Nanopatterns. *Small* **2005**, *1*, 984–991.

(242) Hoff, J. D., Cheng, L.-J., Meyhöfer, E., Guo, L. J., Hunt, A. J. Nanoscale Protein Patterning by Imprint Lithography. *Nano Lett.* **2004**, *4*, 853–857.

(243) Wu, C.-C., Reinhoudt, D. N., Otto, C., Subramaniam, V., Velders, A. H. Strategies for Patterning Biomolecules with Dip-Pen Nanolithography. *Small* **2011**, *7*, 989–1002.

(244) Singh, G., Gohri, V., Pillai, S., Arpanaei, A., Foss, M., Kingshott, P. Large-Area Protein Patterns Generated by Ordered Binary Colloidal Assemblies as Templates. *ACS nano* **2011**, *5*, 3542–3551.

(245) Surwade, S. P., Zhao, S., Liu, H. Molecular Lithography Through DNA-Mediated Etching and Masking of SiO2. *J. Am. Chem. Soc.* **2011**, *133*, 11868–11871.

(246) Surwade, S. P., Zhou, F., Wei, B., Sun, W., Powell, A., O'Donnell, C., Yin, P., Liu, H. Nanoscale Growth and Patterning of Inorganic Oxides using DNA Nanostructure Templates. *J. Am. Chem. Soc.* **2013**, *135*, 6778–6781.

(247) Diagne, C. T., Brun, C., Gasparutto, D., Baillin, X., Tiron, R. DNA Origami Mask for Sub-Ten-Nanometer Lithography. *ACS nano* **2016**, *10*, 6458–6463.

(248) Subramaniam, S., Erler, A., Fu, J., Kranz, A., Tang, J., Gopalswamy, M., Ramakrishnan, S., Keller, A., Grundmeier, G., Müller, D., Sattler, M., Stewart, A. F. DNA Annealing by Redbeta is Insufficient for Homologous Recombination and the Additional Requirements Involve Intra- and Inter-Molecular Interactions. *Sci. Rep.* **2016**, *6*, 34525.

(249) Erler, A., Wegmann, S., Elie-Caille, C., Bradshaw, C. R., Maresca, M., Seidel, R., Habermann, B., Muller, D. J., Stewart, A. F. Conformational Adaptability of Redbeta during DNA Annealing and Implications for its Structural Relationship with Rad52. *J. Mol. Biol.* **2009**, *391*, 586–598.

(250)   Wagner, P. Immobilization Strategies for Biological Scanning Probe Microscopy. *FEBS Lett.* **1998**, *430*, 112–115.

(251)   Ploquin, M., Bransi, A., Paquet, E. R., Stasiak, A. Z., Stasiak, A., Yu, X., Cieslinska, A. M., Egelman, E. H., Moineau, S., Masson, J.-Y. Functional and Structural Basis for a Bacteriophage Homolog of Human RAD52. *Curr. Biol.* **2008**, *18*, 1142–1146.

(252)   Theil, E. C. Ferritin: Structure, Gene Regulation, and Cellular Function in Animals, Plants, and Microorganisms. *Annu. Rev. Biochem.* **1987**, *56*, 289–315.

(253)   Gider, S., Awschalom, D., Douglas, T., Mann, S., Chaparala, M. Classical and Quantum Magnetic Phenomena in Natural and Artificial Ferritin Proteins. *Science* **1995**, *268*, 77–80.

(254)   Bonard, J.-M., Chauvin, P., Klinke, C. Monodisperse Multiwall Carbon Nanotubes Obtained with Ferritin as Catalyst. *Nano Lett.* **2002**, *2*, 665–667.

(255)   Bellido, E., Miguel, R. de, Ruiz-Molina, D., Lostao, A., Maspoch, D. Controlling the Number of Proteins with Dip-Pen Nanolithography. *Adv. Mater.* **2010**, *22*, 352–355.

(256)   Martinez, E., Pla-Roca, M., Samitier, J. Micro/Nanopatterning of Proteins using a Nanoimprint-Based Contact Printing Technique. *Methods Mol. Biol.* **2012**, *811*, 79–87.

(257)   Martinez, R. V., Martinez, J., Chiesa, M., Garcia, R., Coronado, E., Pinilla-Cienfuegos, E., Tatay, S. Large-Scale Nanopatterning of Single Proteins used as Carriers of Magnetic Nanoparticles. *Adv. Mater.* **2010**, *22*, 588–591.

(258)   Zhang, F., Gates, R. J., Smentkowski, V. S., Natarajan, S., Gale, B. K., Watt, R. K., Asplund, M. C., Linford, M. R. Direct Adsorption and Detection of Proteins, Including Ferritin, onto Microlens Array Patterned Bioarrays. *J. Am. Chem. Soc.* **2007**, *129*, 9252–9253.

(259)   Kumagai, S., Yoshii, S., Yamada, K., Matsukawa, N., Fujiwara, I., Iwahori, K., Yamashita, I. Electrostatic Placement of Single Ferritin Molecules. *Appl. Phys. Lett.* **2006**, *88*, 153103.

(260)   Wright, A. K., Thompson, M. R. Hydrodynamic Structure of Bovine Serum Albumin Determined by Transient Electric Birefringence. *Biophys. J.* **1975**, *15*, 137–141.

(261)   Reimhult, K., Petersson, K., Krozer, A. QCM-D Analysis of the Performance of Blocking Agents on Gold and Polystyrene Surfaces. *Langmuir* **2008**, *24*, 8695–8700.

(262)   Jeyachandran, Y. L., Mielczarski, J. A., Mielczarski, E., Rai, B. Efficiency of Blocking of Non-Specific Interaction of Different Proteins by BSA Adsorbed on Hydrophobic and Hydrophilic Surfaces. *J. Colloid Interface Sci.* **2010**, *341*, 136–142.

(263)   Sweryda-Krawiec, B., Devaraj, H., Jacob, G., Hickman, J. J. A New Interpretation of Serum Albumin Surface Passivation. *Langmuir* **2004**, *20*, 2054–2056.

(264) Yang, B., Wyman, C. E. BSA Treatment to Enhance Enzymatic Hydrolysis of Cellulose in Lignin Containing Substrates. *Biotechnol. Bioeng.* **2006**, *94*, 611–617.

(265) Liu, Y.-H., Li, H.-N., Chen, W., Liu, A.-L., Lin, X.-H., Chen, Y.-Z. Bovine Serum Albumin-Based Probe Carrier Platform for Electrochemical DNA Biosensing. *Anal. Chem.* **2013**, *85*, 273–277.

(266) An, Y. H., Stuart, G. W., McDowell, S. J., McDaniel, S. E., Kang, Q., Friedman, R. J. Prevention of Bacterial Adherence to Implant Surfaces with a Crosslinked Albumin Coating In Vitro. *J. Orthop. Res.* **1996**, *14*, 846–849.

(267) Jeyachandran, Y. L., Mielczarski, E., Rai, B., Mielczarski, J. A. Quantitative and Qualitative Evaluation of Adsorption/Desorption of Bovine Serum Albumin on Hydrophilic and Hydrophobic Surfaces. *Langmuir* **2009**, *25*, 11614–11620.

(268) Azioune, A., Siroti, F., Tanguy, J., Jouini, M., Chehimi, M. M., Miksa, B., Slomkowski, S. Interactions and Conformational Changes of Human Serum Albumin at the Surface of Electrochemically Synthesized Thin Polypyrrole Films. *Electrochim. Acta* **2005**, *50*, 1661–1667.

(269) Khullar, P., Singh, V., Mahal, A., Dave, P. N., Thakur, S., Kaur, G., Singh, J., Singh Kamboj, S., Singh Bakshi, M. Bovine Serum Albumin Bioconjugated Gold Nanoparticles: Synthesis, Hemolysis, and Cytotoxicity toward Cancer Cell Lines. *J. Phys. Chem. C* **2012**, *116*, 8834–8843.

(270) Alam, S., Mukhopadhyay, A. Conjugation of Gold Nanorods with Bovine Serum Albumin Protein. *J. Phys. Chem. C* **2014**, *118*, 27459–27464.

(271) Nakane, Y., Sasaki, A., Kinjo, M., Jin, T. Bovine Serum Albumin-Coated Quantum Dots as a Cytoplasmic Viscosity Probe in a Single Living Cell. *Anal. Methods* **2012**, *4*, 1903.

(272) Lensun, L., Smith, T. A., Gee, M. L. Partial Denaturation of Silica-Adsorbed Bovine Serum Albumin Determined by Time-Resolved Evanescent Wave-Induced Fluorescence Spectroscopy. *Langmuir* **2002**, *18*, 9924–9931.

(273) Terashima, H., Tsuji, T. Adsorption of Bovine Serum Albumin onto Mica Surfaces Studied by a Direct Weighing Technique. *Colloids Surf., B* **2003**, *27*, 115–122.

(274) Fitzpatrick, H., Luckham, P. F., Eriksen, S., Hammond, K. Bovine Serum Albumin Adsorption to Mica Surfaces. *Colloids and Surf.* **1992**, *65*, 43–49.

(275) Mori, O., Imae, T. AFM Investigation of the Adsorption Process of Bovine Serum Albumin on Mica. *Colloids Surf., B* **1997**, *9*, 31–36.

125

(276)   Kan, Y., Tan, Q., Wu, G., Si, W., Chen, Y. Study of DNA Adsorption on Mica Surfaces Using a Surface Force Apparatus. *Sci. Rep.* **2015**, *5*, 8442.

(277)   Yun, J. M., Kim, K. N., Kim, J. Y., Shin, D. O., Lee, W. J., Lee, S. H., Lieberman, M., Kim, S. O. DNA origami nanopatterning on chemically modified graphene. *Angew. Chem. Int. Ed. Engl.* **2012**, *51*, 912–915.

(278)   Teschome, B., Facsko, S., Gothelf, K. V., Keller, A. Alignment of Gold Nanoparticle-Decorated DNA Origami Nanotubes: Substrate Prepatterning versus Molecular Combing. *Langmuir* **2015**, *31*, 12823–12829.

(279)   Teshome, B., Facsko, S., Keller, A. Topography-controlled alignment of DNA origami nanotubes on nanopatterned surfaces. *Nanoscale* **2014**, *6*, 1790–1796.

(280)   Pearson, A. C., Pound, E., Woolley, A. T., Linford, M. R., Harb, J. N., Davis, R. C. Chemical alignment of DNA origami to block copolymer patterned arrays of 5 nm gold nanoparticles. *Nano Lett.* **2011**, *11*, 1981–1987.

(281)   Hulteen, J. C., van Duyne, R. P. Nanosphere lithography: A materials general fabrication process for periodic particle array surfaces. *J. Vac. Sci. Technol. A* **1995**, *13*, 1553–1558.

(282)   Dimitrov, A. S., Nagayama, K. Continuous Convective Assembling of Fine Particles into Two-Dimensional Arrays on Solid Surfaces. *Langmuir* **1996**, *12*, 1303–1311.

(283)   Born, P., Blum, S., Munoz, A., Kraus, T. Role of the meniscus shape in large-area convective particle assembly. *Langmuir* **2011**, *27*, 8621–8633.

(284)   Fredriksson, H., Alaverdyan, Y., Dmitriev, A., Langhammer, C., Sutherland, D. S., Zäch, M., Kasemo, B. Hole–Mask Colloidal Lithography. *Adv. Mater.* **2007**, *19*, 4297–4302.

(285)   Agheli, H., Malmström, J., Larsson, E. M., Textor, M., Sutherland, D. S. Large area protein nanopatterning for biological applications. *Nano Lett.* **2006**, *6*, 1165–1171.

(286)   Ogaki, R., Bennetsen, D. T., Bald, I., Foss, M. Dopamine-assisted rapid fabrication of nanoscale protein arrays by colloidal lithography. *Langmuir* **2012**, *28*, 8594–8599.

(287)   Coe, J. V., Heer, J. M., Teeters-Kennedy, S., Tian, H., Rodriguez, K. R. Extraordinary transmission of metal films with arrays of subwavelength holes. *Annu. Rev. Phys. Chem.* **2008**, *59*, 179–202.

(288)   Genet, C., Ebbesen, T. W. Light in tiny holes. *Nature* **2007**, *445*, 39–46.

(289)   Masson, J.-F., Murray-Méthot, M.-P., Live, L. S. Nanohole arrays in chemical analysis: Manufacturing methods and applications. *Analyst* **2010**, *135*, 1483–1489.

(290) Escobedo, C. On-chip nanohole array based sensing: A review. *Lab Chip* **2013**, *13*, 2445–2463.

(291) Pibiri, E., Holzmeister, P., Lalkens, B., Acuna, G. P., Tinnefeld, P. Single-molecule positioning in zeromode waveguides by DNA origami nanoadapters. *Nano Lett.* **2014**, *14*, 3499–3503.

(292) Hajiraissi, R., Hanke, M., Yang, Y., Duderija, B., Gonzalez Orive, A., Grundmeier, G., Keller, A. Adsorption and fibrillization of islet amyloid polypeptide at self-assembled monolayers studied by QCM-D, AFM, and PM-IRRAS. *submitted*, *2018*.

(293) Brassat, K., Assion, F., Hilleringmann, U., Lindner, J. K. N. Self-organization of nanospheres in trenches on silicon surfaces. *Phys. Status Solidi A* **2013**, *210*, 1485–1489.

(294) Keller, A., Facsko, S., Möller, W. Evolution of ion-induced ripple patterns on SiO2 surfaces. *Nucl. Instrum. Methods Phys. Res., Sect. B* **2009**, *267*, 656–659.

(295) Li, Z., Wang, L., Yan, H., Liu, Y. Effect of DNA hairpin loops on the twist of planar DNA origami tiles. *Langmuir* **2012**, *28*, 1959–1965.

(296) Martin, F., Walczak, R., Boiarski, A., Cohen, M., West, T., Cosentino, C., Shapiro, J., Ferrari, M. Tailoring width of microfabricated nanochannels to solute size can be used to control diffusion kinetics. *J. Control. Release* **2005**, *102*, 123–133.

8. Appendix

8.1 Abbreviations

Deoxy ribonucleic acids	DNA
Ribonucleic acids	RNA
Nucleotides	nt
Double stranded DNA	ds-DNA
Atomic force microscopy	AFM
Scanning tunneling microscope	STM
Scanning probe microscope	SPM
Two dimensional , Three dimentional	2D, 3D
Tris acetate EDTA buffer	TAE buffer
Tris acetate buffer	TA buffer
Ethylenediaminetetraacetic acid	EDTA
Deoxyribonuclease	DNase
Caspase-activated DNase	CAD
Three prime repair exonuclease 1	TREX1
DNase II-like acid DNase	DLAD
Fetal bovine serum	FBS
Bovine serum albumin	BSA
6-Helix bundles	6HB
Förster resonance energy transfer	FRET
Single-molecule Förster resonance energy transfer	smFRET
Ultra violet	UV
Human epithelial carcinoma cell lysate	HeLa cell lysate
Roswell Park Memorial Institute medium	RPMI medium
Human embryonic kidney cells	HEK cells
Sodium chloride	NaCl
Magnesium chloride	$MgCl_2$
Potassium chloride	KCl

128

Potassium dihydrogen phosphate KH_2PO_4

Molar M

Guanidinium chloride GdmCl

Melting temperature T_m

Two-dimensional fast Fourier transform 2D FFT

High-performance liquid chromatography HPLC

Self-assembled monolayer SAM

Single strand annealing proteins SSAPs

Kilo Dalton kDa

Molecular weight MW

Isoelectric point pI

Potential of hydrogen pH

Green fluorescent protein tagged Red Redβ GFP-Redβ

Immunoglobulin G protein IgG

Nanosphere lithography NSL

Scanning electron microscopy SEM

Coefficient of variance CV

Polystyrene PS

SiO_2 Silicon dioxide

1-octadecanethiol ODT

8.2 List of Publications

8.2.1 Part of this work have been / will be published in

1. **Saminathan Ramakrishnan**, Georg Krainer, Guido Grundmeier, Michael Schlierf, Adrian Keller*, Structural stability of DNA origami nanostructures in the presence of chaotropic agents, Nanoscale 8 (2016) 10398-10405.

2. **Saminathan Ramakrishnan**, Sivaraman Subramaniam, A Francis Stewart, Guido Grundmeier, Adrian Keller*, Regular Nanoscale Protein Patterns via Directed Adsorption through Self-Assembled DNA Origami Masks, ACS Appl. Mater. Interfaces, 2016, 8 (45), 31239–31247.

3. **Saminathan Ramakrishnan**, Georg Krainer, Guido Grundmeier, Michael Schlierf, Adrian Keller*, Cation-Induced Stabilization and Denaturation of DNA Origami Nanostructures in Urea and Guanidinium Chloride, Small 2017, 1702100.

4. Katharina Brassat, **Saminathan Ramakrishnan**, Julius Bürger, Marcel Hanke, Mahnaz D. Kejdehi, Jörg K. N. Lindner, Guido Grundmeier and Adrian Keller*, Directed Adsorption of DNA Origami Nanostructures in Nanohole Arrays (Submitted)

5. Book chapter: Directed Protein Adsorption through DNA Origami Masks, **Saminathan Ramakrishnan**, Guido Grundmeier, Adrian Keller*, DNA Nanotechnology Methods and Protocols (second edition), Springer (submitted).

8.2.2 Other publications

1. Sivaraman Subramaniam, Axel Erler, Jun Fu, Andrea Kranz, Jing Tang, Mohanraj Gopalswamy, **Saminathan Ramakrishnan**, Adrian Keller, Guido Grundmeier, Daniel Müller, Michael Sattler, A Francis Stewart, DNA annealing by Redβ is insufficient for homologous recombination and the additional requirements involve intra-and inter-molecular interactions, Scientific Reports. 2016, 6, 34525.

2. Fabian Kollmann, **Saminathan Ramakrishnan**, Boxuan Shen, Guido Grundmeier, Mauri A. Kostiainen, Veikko Linko* and Adrian Keller*, Superstructure-dependent loading of DNA origami nanostructures with a groove-binding drug. (submitted)

8.3 Affidavit

I hereby declare that this thesis is my original work and I have not copied or used any other information except that are mentioned through citations. All the figures, tables and scientific data used in this thesis from other sources are properly acknowledged.

Paderborn 2018

Saminathan Ramakrishnan